LES of turbulent cavitating flows using the homogeneous mixture model

A DISSERTATION
SUBMITTED TO THE FACULTY OF THE GRADUATE SCHOOL
OF THE UNIVERSITY OF MINNESOTA
BY

Mrugank Bhatt

IN PARTIAL FULFILLMENT OF THE REQUIREMENTS
FOR THE DEGREE OF
DOCTOR OF PHILOSOPHY

Krishnan Mahesh, Adviser

Sep, 2020

Acknowledgements

First and foremost, I would like to extend my deepest gratitude to my advisor Prof. Krishnan Mahesh for allowing me to work in his research group. His knowledge, experience, guidance, and motivation have been instrumental in aiding the completion of my research work. I admire his teaching and presentation skills. I have learnt a lot by rehearsing conference presentations with him and through his feedback on scientific writings.

I would like to extend my gratitude to Prof. Ellen Longmire, Prof. Filippo Coletti, and Prof. Ilja Siepmann for being in my examination committee and reviewing my thesis. I am also benefited greatly from the teachings of various faculty members including the committee members through the coursework. Special thanks to Prof. Bernardo Cockburn for giving his time outside of class for the insightful discussions on the numerical analysis. The work in this dissertation was supported by the United States Office of Naval Research under Grant ONR N00014-14-1-0290 and ONR N00014-17-1-2676 with Dr. Ki-Han Kim as the program manager. The computations were made possible through the computing resources provided by the High-Performance Computing Modernization Program (HPCMP), Texas Advanced Computing Center (TACC), and the Minnesota Supercomputing Institute (MSI). I acknowledge Dr. Harish Ganesh and Prof. Steve Ceccio at the University of Michigan, for providing the experimental data for the wedge. I acknowledge Ms. Jingyi Chen and Prof. Ilja Siepmann for insightful discussions on the molecular dynamics calculations.

Many thanks to all my colleagues at the University of Minnesota. Special thanks to Mr. Sreevatsa Anantharamu, Dr. Narendra Singh, and Dr. Durgesh Chandel. Our

many interactions helped me to cultivate the right attitude for the research. All the past and current group members of Prof. Mahesh's lab have been very approachable and helpful. Special thanks to Dr. Aswin Gnanaskandan for mentoring me during the initial stages of my Ph.D. and answering innumerable silly questions. I thank Mr. Filipe Brandao and Mr. Aditya Madabhushi for the stimulating discussions on cavitation. I thank Dr. Praveen Kumar and Mr. Thomas Kroll for discussing cutting-edge grid generation tricks and tips. I am also benefited from my interactions with Dr. Karim Alame, Dr. Wyatt Horne, Ms. Rong Ma, Mr. Ali Fakhreddine, Ms. Samantha Harel, and Mr. Nick Morse.

I would like to thank all my friends for making my stay in Minnesota exciting and memorable. I equally thank both Rahul Shah and Rahul Anand for fun excursions to Guthrie Theatre, State Fair, driving trips, and many more memorable moments. I thank Rishabh Sehgal for giving me many epic Rishabh Sehgal moments to cherish. Thanks to Anant and Shreyas for the melodious jamming sessions. Thanks to Anshul, Rachit, Deepesh, and many more for fun gatherings that brought excitement to the otherwise monotonous work routine in grad school. Thanks to Prateeth and Sandeep for enjoyable and informative discussions on Machine Learning. Thanks to my roommates Karan and Anchit for their company and for sharing great times watching the episodes of "The Office" at night.

Finally, this work would not have been possible without limitless love, support, and care of my parents Mr. Pranav Bhatt and Mrs. Sweta Bhatt. Purely observing them conduct their day to day life with utmost simplicity and selflessness has nurtured me to create well-being in the society. I would also like to thank my aunt Ms. Trupti Bhatt. Her presence and blessings always bring joy and innocence to me. Lastly, I would like to thank all who brought yoga to me. In the time of my life that involved significant use of the intellect through data analysis, critical thinking, reasoning, communications, and discussions; the practice of yoga invigorated the experiential dimension of life. Through these times the yoga has brought significant learning to see the limitations of the intellect and enhanced the experience of life.

To my family

Abstract

The objective of this dissertation is to develop LES (large-eddy simulation) capabilities to study cavitation in complex hydrodynamic geometries. The methodology is based on a fully-compressible homogeneous mixture model and finite rate mass transfer. Overall, the goals of the dissertation are to: (i) Evaluate the finite rate homogeneous mixture model. (ii) Apply the mixture model to study range of partial cavitation regimes over a sharp wedge. (iii) Perform propeller simulations. (iv) Address the acoustic stiffness of the density-based solver using preconditioning and DTS (dual-time stepping) approaches.

The ability of the homogeneous mixture approach to capture resolved small-scale vapor bubbles is evaluated by a $0.12mm$ vapor bubble collapse problem. The effect of physical length scale and surface tension is assessed by comparing the results from the homogeneous mixture model and Rayleigh-Plesset equation for a range of bubble sizes. The finite rate effects of the cavitation model are discussed using the non-dimensional parameters and compared to the flow advection time scales. Finally, the expression for the speed of sound is derived that accounts for the finite rate mass transfer and compared to the limits of the equilibrium and the frozen speed of sound assumptions.

Partial cavitation over a range of incipient, transitory and periodic regimes is investigated using LES in the (experimental) sharp wedge configuration of Ganesh et al. [1]. Physical mechanisms of cavity transition observed in the experiments; i.e. re-entrant jet and bubbly shock wave, are both captured in the LES over their respective regimes. Vapor volume fraction data obtained from the LES is quantitatively compared to X-ray densitometry. In the transitory and periodic regimes, void fractions resulting

from complex interactions of large regions of vapor in the sheet/cloud show very good comparison with the experiments. Also, very good agreement with the experiments is obtained for the shedding frequency and the bubbly shock wave propagation speed. Conditions favoring either the formation of the re-entrant jet or the bubbly shock wave are analyzed by contrasting the LES results between the regimes and discussed in detail. Bubbly shock wave propagation is observed to be initiated by the impingement of the collapse-induced pressure waves from the previously shed cloud and discussed using the Rankine-Hugoniot jump conditions.

Flow over a five-bladed marine propeller (P4381) is studied at Reynolds number of 894,000 at design conditions. Simulations are performed for the wetted conditions and the propeller loads obtained from the simulations are compared to the experiments. Evaluation of propeller shaft orientation, numerical dissipation, the pressure drop in vortex cores, freestream nuclei, and grid resolution is presented. The assessment revealed that the propeller performance is sensitive to the free-stream nuclei content, with lower values showing a better comparison to the experiments.

A numerical approach based on preconditioning and dual-time stepping is proposed to address the acoustic stiffness; thereby, enabling low free-stream nuclei calculations using the density-based solver. The key aspects of the numerical approach are: (i) preconditioning applied to the cavitating flow equations for a fully-compressible system, (ii) modifications based on the all-speed Roe-type scheme to the characteristic-based filtering, and (iii) implementation in parallel and on unstructured grids that allow the simulation of complex problems such as a propeller. The results are demonstrated for the unsteady flow over a cylinder under wetted and cavitation inception conditions, and the LES of flow over a propeller under wetted conditions.

Contents

List of Tables

List of Figures

Chapter 1

Introduction

1.1 Cavitation

Cavitation is the phase change of a liquid into vapor when the liquid pressure drops below vapor pressure. An important fluid property that governs cavitation is the vapor pressure (p_v), which is defined as the pressure exerted by the vapor in thermodynamic equilibrium with its condensed phase at a given temperature. The vapor pressure of water at 298 K is 2700 Pa, while the vapor pressure at 373 K (boiling point of water) is 1 atmosphere. The difference between the ambient pressure and the vapor pressure is an indicator of whether cavitation can occur or not and hence a non–dimensional parameter termed cavitation number $\sigma = \dfrac{p_\infty - p_v}{0.5\rho_\infty u_\infty^2}$ is used to characterize cavitating flows. Here, p_∞, ρ_∞ and u_∞ are free stream pressure, density and velocity respectively. Cavitation can be classified based on the method of vapor generation as (i) hydrodynamic cavitation, (ii) acoustic cavitation, and (iii) optic and particle cavitation. Hydrodynamic cavitation is caused by pressure variations induced due to the geometry (e.g. marine propellers, hydrofoils, rotating turbomachinery, nozzles, etc.). Nucleation, growth, and collapse of the bubble due to the passage of acoustic waves is termed as acoustic cavitation (e.g. use of ultrasound to break kidney stones, sonoluminescence, sonoporation, etc). Breakdown of the liquid medium caused due to local energy deposition using respectively, high-intensity photons and other elementary particles (e.g.

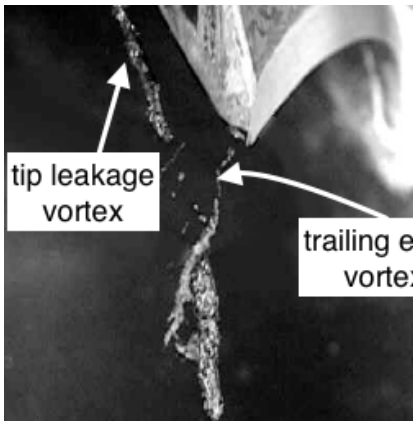

a)

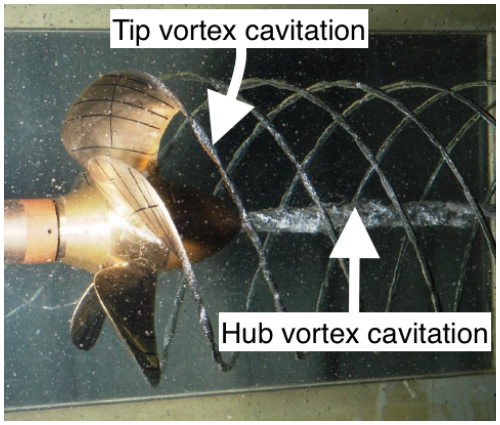

b)

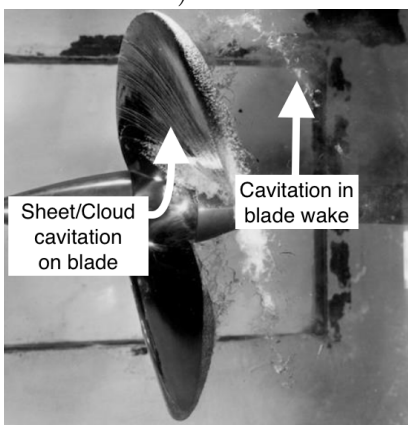

c)

Figure 1.1: Cavitation over marine propellers. a) Cavitation inception ([2]), b) vortex cavitation ([3]) and c) massive sheet/cloud type cavitation ([4]).

protons, neutrons) are termed as optic cavitation and particle cavitation. This dissertation is mainly concerned with hydrodynamic cavitation. Although, the methodology and physical insights obtained can be extended to other types of cavitation. Figure 1.1 shows hydrodynamic cavitation over marine propulsors as an example.

1.1.1 Regimes of hydrodynamic cavitation

Cavitation in marine applications (e.g. propellers, hydrofoils) exists over different regimes - ranging from inception to massive regions of vapor as shown in figure 1.1. The various regimes can be observed as the cavitation number (σ) in the free stream

is dropped, thereby generating more and more vapor. Based on this, the hydrodynamic cavitation can be classified into the following regimes: (i) cavitation inception, (ii) incipient cavitation, (iii) developed cavitation, and (iv) supercavitation.

Cavitation inception

Cavitation inception is commonly observed in the turbulent shear layers, tip vortices, and wakes of marine geometries. Cavitation inception occurs when static pressure in the flow locally drops below the vapor pressure. Cavitation inception is often captured by the acoustic signal before the nuclei sizes grow and become evident visibly. Often the bubbles do not grow to the observable size until the static pressure drops by a finite amount below vapor pressure. The difference in pressure depends on the ability of the liquid to sustain tension. The magnitude of this tension is a function of the size and properties of the microbubbles (referred to as "cavitation nuclei") that grow to produce observable bubbles (see Brennen [5]). Cavitation inception over a marine propeller is shown in figure 1.1(a). The figure is shown for σ lower than cavitation inception so that the interacting tip leakage vortex and trailing edge vortex are visible. Interestingly, in such vortex pair interactions, the vortices whose strength is much less than the neighboring vortices are often observed to incept first [6]. In turbulent shear layers, depending upon the flow conditions cavitation inception can often be observed in quasi streamwise vortices at higher ambient pressures as compared to stronger spanwise vortices [7].

Incipient cavitation

Once incepted, the microbubbles grow in size and become visible in low-pressure regions in the flow with the reduction in σ. It is often observed as a low vapor void fraction bubbly mixture (see Ganesh et al. [1]).

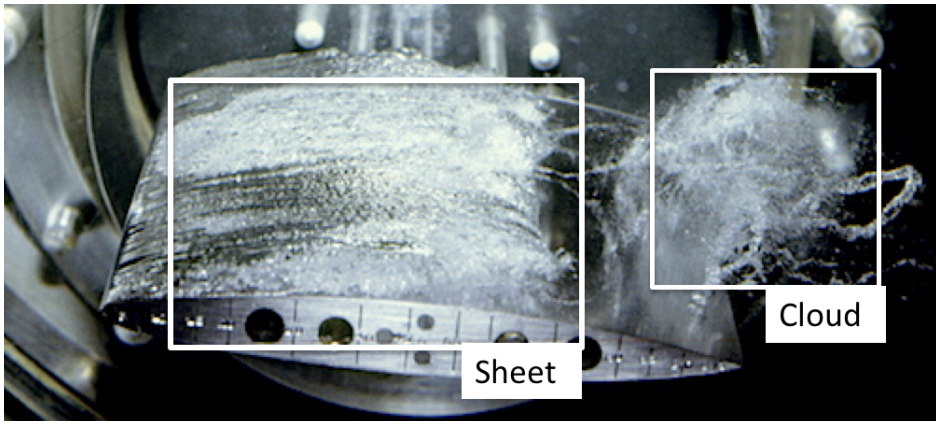

Figure 1.2: Sheet to cloud cavitation over a hydrofoil with a detached cloud cavity [9].

Developed Cavitation

With the reduction in σ, vapor regions grow in size forming sheet-like structures on the suction side of the body. The sheet cavity intermittently sheds into the cloud, referred to as "sheet to cloud transition". Figure 1.2 shows a sheet to cloud cavitation over a hydrofoil. The collapse of these large clouds in the regions of pressure recovery is a major cause of the noise, vibration, and material damage. The sheet to cloud transition is classically associated with the formation of a re-entrant jet at the cavity closure Callenaere et al. [8]. However, recently, Ganesh et al. [1] in the experimental study over a sharp wedge, observed that if the σ is sufficiently low, the sheet to cloud transition can happen due to the propagation of bubbly shock waves. The sheet to cloud transition is the most common type of cavitation observed in a variety of applications including propellers, hydrofoils, diesel injectors, pumps, etc. Figure 1.1(c) shows massive sheet/cloud type cavitation on a suction side of propeller blade.

Supercavitation

Cavitation is termed as "partial cavitation" when the cavity closes on the cavitating surface. The incipient and developed cavitation considered in the earlier sections are regimes of partial cavitation. With the reduction in σ, if the cavity becomes large enough to encompass the object traveling through the liquid, it is termed as "supercavitation".

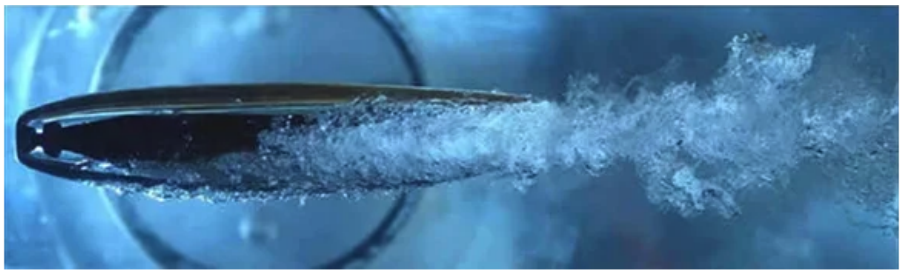

Figure 1.3: Example of supercavitation at Saint Anthony Falls Laboratory, University of Minnesota [10].

Figure 1.3 shows axisymmetric ventilated supercavitation. It has potential applications in drag and noise reduction in high-speed underwater transportation.

In this dissertation, we focus on the study of partial cavitation (i.e. both incipient and developed cavitation). Also, we discuss the extension of the methodology to potentially study cavitation inception problems.

1.2 Motivation

Cavitation is significant in several contexts. In marine applications, it is typically problematic. Examples, where cavitation can cause damage, including pumps, propellers, and hydraulic machinery, where vibration and surface erosion caused due to cavitation not only lead to adverse performance but also reduce the overall structural integrity. The vapor pockets produced by cavitation can collapse near a solid surface generating high impact loads on the surface. Erosion due to cavitation can cause undesirable noise in addition to weakening the structural integrity of the propeller. Cavitation can also be beneficial in some applications. For example, in the biomedical context, we can use ultrasound to form and direct the collapse of the cavitation bubbles to break up the kidney stones. Cavitation can be used to change the permeability of the cell plasma membrane by a process called sonoporation, which can then be used for targeted drug delivery. In industrial cleaning applications, the violent nature of cavitation is used to overcome particle-substrate adhesion forces to loosen contaminants from the substrate. The importance of studying cavitation lies in its occurrence in these wide arrays of

applications. An in-depth understanding of cavitation in such cases is necessary if we are to reduce the detrimental effects it causes while also exploiting its beneficial effects.

1.3 Challenges

In addition to the single-phase flows, cavitating flows pose various challenges for numerical modeling. As shown in the figure 1.1, depending on the geometry of the propeller and the flow conditions multiple types of cavitation can co-exist in the flow, such as vortex cavitation inside low-pressure cores of tip and hub vortices, sheet/cloud type of cavitation on the suction side of the propeller blade, etc. This results in a complex flow field of an inherently unsteady propeller wake. Being able to resolve the regions of interest and keeping the overall mesh size computationally feasible is also a challenge for generating a mesh for such complex geometries. It is known that as the flow cavitates, sound speed drops by orders of magnitude in the resulting water-vapor mixture as compared to nearly incompressible regions in water; presenting a wide range of Mach numbers in the flow. Hence, cavitating flows can have shock waves even at a reasonably low free stream velocity, if the flow becomes locally supersonic due to phase change. Besides the shock waves generated by the cavity collapse, cavitating flows can have bubbly shock waves that lead to the sheet to cloud transition [1]. Bubbly shock wave (or referred to as "condensation shock") is a void fraction discontinuity, associated with a retracting partial cavity, traveling at supersonic speed and involving phase change. To capture a variety of such phenomena, accurate modeling of mixture compressibility is necessary. Formation of vapor is often followed by the growth of vapor cavities which not only vary in size but also form and collapse at different rates, presenting a wide range of length/time scales in addition to the turbulence. This requires accurate modeling of mass transfer and its interaction with turbulence. As discussed in section 1.1.1, cavitation can exist over different regimes- ranging from inception to massive cavitation. A challenge lies in extending a computational methodology that is well suited for a particular regime, to other regimes of the flow.

1.4 Past work

To address these challenges variety of computational approaches have been used. In general, the computational approaches vary in the physical modeling of cavitation, turbulence modeling, and numerical pressure/density based formulations.

The most commonly used physical model to simulate cavitating flows is the homogeneous mixture model [11–20]. The homogeneous mixture model assumes the mixture of water and vapor as a single medium. Governing equations are solved for mixture quantities along with either equilibrium mass transfer model [14] or transport equation-based model [19]. Equilibrium models assume instantaneous phase change. Transport equation-based models employ finite rate mass transfer, although the accurate rates for evaporation and condensation are based on empirical models. Besides, the differences among these models lie in the use of the thermodynamic equation of states and calculations of the speed of sound. The challenge lies in obtaining equations of state that are physically valid over the entire range of thermodynamic states encountered in the problem, and also numerically consistent (i.e. preserve hyperbolicity of the governing equations, convex, and account for negative pressures) [21–23]. Accurate modeling of the speed of sound also is important both physically (i.e. to capture the compressibility over a range of vapor void fractions in the liquid) and numerically (i.e. to preserve proper conditioning of the eigenvalues). Experimentally, the measurement of sound speed for the highly unsteady problems in the hydrodynamic cavitation is quite involved. Besides, analytical expressions for the speed of sound provide values in the limit of no mass transfer (i.e. frozen speed of sound) and equilibrium mass transfer (i.e. equilibrium speed of sound) [24]. While it is known that homogeneous mixture models are reasonably accurate in predicting large scale vapor regions, its performance in predicting the dynamics of the small scale vapor regions is largely unknown. Also, the mixture models are typically used to simulate flow in a specific cavitation regime. Hence, the performance of a single mixture model over range regimes encountered in hydrodynamic cavitation has not been evaluated.

Many computational studies have traditionally employed RANS (Reynolds Averaged

Navier–Stokes) models for studying cavitating. [14, 16, 17, 19, 22, 25, 26]. However, standard RANS models require modifications to eddy viscosity for predicting sheet to cloud cavitation [27]. In recent years, LES (Large Eddy Simulation) has shown promising results for capturing the wide range of scales and unsteady nature of cavitating flows [28–32]. Besides, comparative studies conducted using different turbulence models have also suggested the suitability of LES over other approaches [29, 33–35]. Several studies have used pressure based approaches along with RANS or LES for turbulence closure [12, 19, 28].

One major difference between the cavitation solvers is whether they use a pressure-based (e.g. [19]) or a density-based algorithm (e.g. [17]); both of which have to address the range of Mach numbers in cavitating flows. Pressure-based algorithms proposed for single-phase flow often experience convergence problems due to the significant reduction in the speed of sound in the water-vapor mixture regions. Various modifications to the pressure-based algorithms have been proposed to obtain the correct speed of sound in cavitating flows (e.g. [19, 20]). On the other hand, density-based algorithms suffer from the accuracy and numerical stiffness due to the nearly incompressible regions in the water. To mitigate the extremely low Mach regions in the water, several studies based on the fully compressible formulation have used relatively high values of free-stream nuclei [16, 17, 29, 36, 37]. Here, 'free-stream nuclei' refer initial levels of vapor or non-condensable gases (NCG) present in the water. At sufficiently low pressures (typically the vapor pressure) these nuclei act as the starting point for the liquid breakdown to form cavitation [24]. The studies have shown that good agreement with the experiments can be obtained for capturing the large regions of vapor in the developed cavitation regimes [16, 29, 36]. Although, cavitation inception and incipient cavitation are known to be highly sensitive to the nuclei size and their distribution [36, 38]. While important for physical modeling, lower values of free stream nuclei impose a stringent requirement on the time step of the numerical method. This is due to the reduced speed of sound at low nuclei concentration in the water.

1.5 Overview

An overall objective of this dissertation is to develop LES capabilities to simulate turbulent cavitating flows in complex geometries. The principal contributions of this work are as follows:

- The ability of the homogeneous mixture model to capture the dynamics of resolved small scale vapor bubbles is demonstrated.
- Results from the homogeneous mixture model and the Rayleigh-Plesset equation are compared for a range of bubble sizes, with smaller sizes showing the importance of surface tension effects.
- The evaporation/condensation source terms are analysed in terms of non-dimensional parameters that determine the relative time-scale of flow advection with respect to the phase change.
- The effect of considering two-dimensional collapse as is commonly assumed in RANS is illustrated by comparing cylindrical and spherical bubble collapse. Cylindrical bubble collapse is shown to underpredict the collapse pressure by an order of magnitude compared to spherical bubble collapse.
- An expression for the speed of sound accounting for finite rate mass transfer is derived.
- Partial cavitation over incipient, transitory and periodic regimes is investigated using LES in the (experimental) sharp wedge configuration of Ganesh et al. [1].
- A strategy to match inflow-outflow conditions for the different regimes is developed that allows capturing of the bubbly shock wave mechanism.
- In the transitory and periodic regimes, void fractions resulting from the complex interaction of large regions of vapor in the sheet/cloud show very good comparison with X-ray densitometry. Also, very good agreement is observed for shedding

frequency and shock speed. In the incipient regime, the LES results yield a higher cavity length compared to the experiments.

- High streamline curvature, low cavity void fractions, and baroclinic vorticity production in the transitory regime are shown to promote re-entrant jet formation.
- Slow pressure recovery, high cavity void fraction, and nearly two-dimensional cavity in the periodic regime are shown to promote bubbly shock wave formation.
- The bubbly shock waves are found to originate from collapse-induced pressure waves from the previously shed cloud. This is demonstrated using $x-t$ diagrams and Rankine-Hugoniot jump conditions.
- Flow over a marine propeller (P4381) is investigated using compressible LES under wetted conditions.
- Evaluation of propeller shaft orientation, numerical dissipation, freestream nuclei, and grid resolution reveal the need to use low values of free-stream nuclei for the accurate comparison of thrust/torque.
- A numerical approach based on preconditioning and dual-time stepping is developed to handle the acoustic stiffness in cavitating flows at low Mach numbers. The novelty of the method lies in the application of preconditioning to a fully-compressible cavitation solver; where the characteristic-based filtering is modified based on the all-speed Roe-type scheme in addition to the traditional time-derivative matrix.
- The method enables low free-stream nuclei calculations in an accurate manner and in a reasonable amount of time.
- The preconditioned methodology is demonstrated for the unsteady flow over a cylinder under wetted and cavitation inception conditions, and LES of flow over a propeller under wetted conditions.

1.6 Outline

The dissertation is organized as follows. Chapter 2 explains the governing equations, physical model, and numerical method used in the simulations. Chapter 3 discusses the evaluation of the finite rate homogeneous mixture model. Chapter 4 is on the investigation of partial cavitation regimes over a sharp wedge. Chapter 5 applies the methodology to study the flow over a marine propeller. Chapter 6 discusses the preconditioning and the dual-time stepping methodology. Finally, Chapter 7 provides a summary of the dissertation.

Chapter 2

Physical model and numerical method

2.1 Introduction

The chapter is organized as follows. Section 2.2 discusses the governing equations, various components of the physical model and its assumptions. Section 2.3 discusses the predictor–corrector approach for the numerical method. The extension of the methodology to study propeller cavitation is discussed in section 2.4.

2.2 Governing equations and physical model

2.2.1 Model assumptions

We use the homogeneous mixture approach where the mixture of water and vapor is considered as a single compressible medium. We assume mechanical equilibrium (i.e. each phase has the same pressure as the cell pressure and slip velocity between the phases is not considered) and thermal equilibrium (i.e. the temperature of each phase is the same as the cell temperature). The Weber numbers of the simulations considered in this dissertation are very high. For example, the Weber number ($We = \rho u^2 l/S$) for the sharp wedge configuration presented in chapter 4 is of the $O(10^4)$ based on liquid

density ($\rho = 1000\ kg/m^3$), surface tension ($S = 0.07\ N/m^2$), length scale ($l = 0.0254\ m$) and velocity scale ($u = 8\ m/s$). Hence, surface tension effects are generally very small. Assuming a homogeneous mixture, subgrid-scale bubble dynamics and surface tension effects are thus neglected. In hydrodynamic cavitation, due to the high specific heat capacity of the water, medium causes only minor temperature fluctuations. Also, using the current mixture model, Brandao et al. [39] have shown that the temperature rise across even a bubbly shock wave can be negligible. Hence, an isothermal formulation is used to reduce simulation time.

2.2.2 Governing equations

The governing equations are the compressible Navier-Stokes equations for mixture quantities along with the transport equation for vapor mass fraction :

$$\begin{aligned} \frac{\partial \rho}{\partial t} &= -\frac{\partial}{\partial x_j}(\rho u_j), \\ \frac{\partial \rho u_i}{\partial t} &= -\frac{\partial}{\partial x_j}(\rho u_i u_j + p\delta_{ij} - \sigma_{ij}), \\ \frac{\partial \rho Y_v}{\partial t} &= -\frac{\partial}{\partial x_j}(\rho Y_v u_j) + S_e - S_c. \end{aligned} \tag{2.1}$$

Here ρ, u_i and p are density, velocity, and pressure of the mixture respectively, and Y_v is the vapor mass fraction. The mixture density is defined as

$$\rho = \rho_l(1 - \alpha_v) + \rho_v \alpha_v, \tag{2.2}$$

where ρ_l and ρ_v are densities of liquid and vapor respectively, and α_v is the volume fraction of vapor. Volume fractions of each constituent phase are related to their respective mass fractions by

$$\rho_l(1 - \alpha_v) = \rho(1 - Y_v) \quad \text{and} \quad \rho_v \alpha_v = \rho Y_v. \tag{2.3}$$

The viscous stress tensor (σ_{ij}) is given by

$$\sigma_{ij} = \mu\Big(\frac{\partial u_i}{\partial x_j} + \frac{\partial u_j}{\partial u_i} - \frac{2}{3}\frac{\partial u_k}{\partial x_k}\delta_{ij}\Big), \tag{2.4}$$

For the mixture viscosity, we follow Beattie and Whalley [40] and assume that the effective dynamic viscosity of the liquid–vapor mixture satisfies a quadratic law with a maximum in the two–phase region. The mixture viscosity is given by

$$\mu = \mu_l(1-\alpha_v)(1+2.5\alpha_v) + \mu_v\alpha_v, \quad \text{and} \tag{2.5}$$

μ_l and μ_v are the dynamic viscosity of water and vapor respectively. Note that $\mu_l >> \mu_v$. A simple volume average would give the maximum in the liquid region (i.e. for $\alpha_v = 0$), while a quadratic dependence in Beattie and Whalley [40] yields an initial increase in the mixture viscosity, moving from liquid to the mixture. The mixture viscosity is maximum in the two-phase region near liquid. Molecular dynamics simulations confirm this behavior [41].

2.2.3 Equation of state (*EOS*)

We use ideal gas *EOS* for vapor and stiffened *EOS* for water. The individual *EOS* and mixture *EOS* in terms of its constinuent phases are given as:

$$\begin{aligned} p_g &= \rho_v R_v T, \\ p_l &= -P_c + \rho_l K_l T \quad \textit{and} \\ p &= p_g\alpha_v + p_l(1-\alpha_v). \end{aligned} \tag{2.6}$$

Here, p_g and p_l respectively are gas and liquid pressures. $K_l = 2684.075\ J/(KgK)$ and $P_c = 786.333 \times 10^6\ Pa$ are the constants associated with equation of state for the liquid. In order to obtain accurate speed of sound and density variation using the stiffened *EOS*, various numerical studies have derived the EOS parameters by modifying the specific heats of the liquid phase [16, 42, 43]. The current study uses the parameters derived by Gnanaskandan and Mahesh [43] to match speed of sound in liquid at prescribed density

to NIST data. The specific heat at constant volume is thus modified to $1500 J/Kgk$, which is under predicted as compared to the NIST value of $4157.4. J/Kgk$. This however, is not a serious drawback, considering the near isothermal nature of the hydrodynamic cavitation problems considerd in the dissertation. The following inequality must hold for the given stiffened EOS to be convex as discussed by Goncalves and Patella [22]:

$$a_l^2 \geq \frac{(\gamma_l - 1)^2 C_{pl} T}{\gamma_l}. \tag{2.7}$$

Here, a_l, γ_l and C_{pl} respectively are the speed of sound, the ratio of specific heats and the specific heat at constant pressure for liquid. For the current set of parameters; $a_l = 1400\ m/s$, $\gamma_l = 2.7889$ and $C_{pl} = 4184 J/Kgk$; the inequality 2.7 holds. Hence, the stiffened EOS used here is convex. In addition to Gnanaskandan and Mahesh [43], the computational studies that followed such as Gnanaskandan and Mahesh [29] and Bhatt and Mahesh [36], have validated the thermodynamic model for a variety of cavitation regimes. $R_v = 461.6\ J/(KgK)$ is the specific gas constant for equation of state of vapor obtained from [16]. The mechanical equilibrium implies:

$$p_g = p_l = p. \tag{2.8}$$

The system 2.1 is closed using a mixture equation of state obtained obtained from equations 2.6 and 2.8 as:

$$p = Y_v \rho R_v T + (1 - Y_v) \rho K_l T \frac{p}{p + P_c}. \tag{2.9}$$

2.2.4 Mass transfer model

S_e and S_c are source terms for evaporation of water and condensation of vapor and are given by

$$\begin{aligned} S_e &= C_e \alpha_v^2 (1 - \alpha_v)^2 \frac{\rho_l}{\rho_g} \frac{\max((p_v - p), 0)}{\sqrt{2\pi R_g T}}, \\ S_c &= C_c \alpha_v^2 (1 - \alpha_v)^2 \frac{\max((p - p_v), 0)}{\sqrt{2\pi R_g T}}, \end{aligned} \tag{2.10}$$

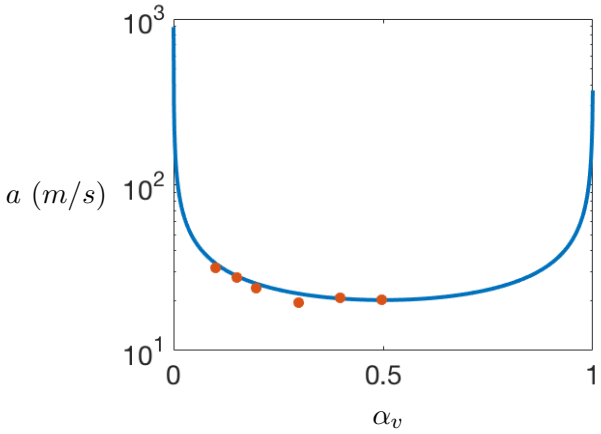

Figure 2.1: Comparison of sound speed in water-gas mixture to experiments at $0.1MPa$. Equation 2.11 ▬, Karplus [44] ●.

where $p_v = 2.3\ kPa$ is the vapor pressure. $C_e(1/m)$ and $C_c(1/m)$ are empirical constants. A value of $0.1m^{-1}$ was suggested by Saito et al. [16] in the original mass transfer model. They have shown that the solution is not sensitive to the value of $0.1m^{-1}$ using the cavitating flow over hemispherical/cylindrical bodies. In addition, Gnanaskandan and Mahesh [43] have shown validation over a variety of flow problems with the original value of $0.1m^{-1}$. While it is reassuring to note that the solution has been largely insensitive to the values of the empirical constants in these studies, the dimensional nature of the values prompts for improvement. For example, Bhatt and Mahesh [36] non-dimensionalize the empirical constants based on the characteristic length scale of the problem. For the sharp wedge configuration, they choose wedge height as the characteristic length scale to non-dimnesionalize source term as $1/h = 36.5\ 1/m$, where $h = 1\ inch$ is the wedge height. They obtained very good comparison for void fraction data to the X-ray measurements in developed cavitation regimes.

2.2.5 Speed of sound

The isothermal mixture speed of sound is obtained by taking the derivative of the mixture equation of state (2.9) to ρ at constant T. The expression of the mixture sound

speed is given as

$$a^2 = \frac{(p + P_c)Y_v RgT + p(1 - Y_v)K_l T}{2p + P_c - \rho Y_v RgT - (1 - Y_v)\rho K_l T}. \tag{2.11}$$

Note that the isothermal speed of sound is chosen to keep consistency with the isothermal assumption in the governing equations. The change in the speed of sound with gaseous phase volume fraction at a temperature of $298K$ and a pressure of $0.1MPa$ using equation 2.11 is compared to the experimental data of Karplus [44] in figure 2.1. Note the good agreement with experiments in the mixture region. The effect of gas volume fraction in changing the acoustic characteristics of water is evident by the orders of magnitude drop in the sound speed. The derivation of sound speed in the equation 2.11 does not account for the variation in Y_v, which implies no mass transfer between the phases. Hence, it is considered as the frozen speed of sound. Alternatively, the equilibrium cavitation models assume that the mass transfer between the phases is instantaneous and consider the equilibrium speed of sound [45]. Due to the finite rate of phase change, the speed of sound in a water-vapor mixture is lower than the frozen sound speed limit and higher than the equilibrium speed of sound limit [24]. Sound speed in such cases depends on the accurate rate of phase change, subgrid-scale bubble dynamics, and non-condensable gas nuclei. Hence, it often depends on the problem. The accurate measurement of the speed of sound experimentally, in highly unsteady flows such as considered in the thesis is quite involved. Besides, analytical expressions for the speed of sound provide values in the limit of no mass transfer (i.e. frozen speed of sound) and equilibrium mass transfer (i.e. equilibrium speed of sound) [24]. In the transport equation-based models the expression for the mixture speed of sound accounting for finite rate mass transfer effects can be derived using the cavitation source terms. However, the empiricism of the source terms poses a challenge in accounting for the changes in sound speed with accurate mass transfer rates.

2.2.6 Turbulence model

Governing equations (2.1) are spatially Favre filtered for LES as:

$$\begin{aligned}
\frac{\partial \overline{\rho}}{\partial t} &= -\frac{\partial}{\partial x_k}\left(\overline{\rho}\tilde{u_k}\right), \\
\frac{\partial \overline{\rho}\tilde{u_i}}{\partial t} &= -\frac{\partial}{\partial x_k}\left(\overline{\rho}\tilde{u}_i\tilde{u}_k + \overline{p}\delta_{ik} - \tilde{\sigma}_{ik} - \tau_{ik}\right) \\
\frac{\partial \overline{\rho}\tilde{Y_v}}{\partial t} &= -\frac{\partial}{\partial x_k}\left(\overline{\rho}\tilde{Y_v}\tilde{u_k} - t_k\right) + \tilde{S}_e - \tilde{S}_c,
\end{aligned} \tag{2.12}$$

Here, the tilde quantities are Favre averaged quantities and τ_{ik}, q_k and t_k are subgrid scale (SGS) terms namely: SGS stress, SGS heat flux and SGS scalar flux. These terms are modeled using the Dynamic Smagorinsky model (DSM) [46]:

$$\begin{aligned}
\tau_{ij} - \frac{\delta_{ij}}{3}\tau_{kk} &= -2C_S(\mathbf{x},t)\overline{\rho}\Delta^2\left|\tilde{S}\right|\widetilde{S^*_{ij}}, \\
\tau_{kk} &= 2C_I(\mathbf{x},t)\overline{\rho}\Delta^2\left|\tilde{S}\right|^2, \\
t_i &= -\overline{\rho}\frac{C_S(\mathbf{x},t)\Delta^2\left|\tilde{S}\right|}{Sc_T}\frac{\partial\overline{Y_v}}{\partial x_i},
\end{aligned} \tag{2.13}$$

where $|S| = \sqrt{2S_{ij}S_{ij}}$ and $S^*_{ij} = S_{ij} - 1/3S_{kk}\delta_{ij}$. The model coefficients C_s, C_I, and Sc_T are determined by the Germano identity. For example,

$$\begin{aligned}
C_S\Delta^2 &= \frac{1}{2}\frac{\left\langle L^*_{ij}M^*_{ij}\right\rangle}{\left\langle M^*_{ij}M^*_{ij}\right\rangle}, \\
L^*_{ij} &= \left(\frac{\widehat{\overline{\rho u_i}\cdot\overline{\rho u_j}}}{\overline{\rho}}\right) - \frac{\widehat{\overline{\rho u_i}}\cdot\widehat{\overline{\rho u_j}}}{\widehat{\overline{\rho}}}, \\
M^*_{ij} &= \widehat{\overline{\rho}\left|\tilde{S}\right|\widetilde{S^*_{ij}}} - \widehat{\overline{\rho}}\left(\frac{\widehat{\Delta}}{\Delta}\right)^2\widehat{\left|\tilde{S}\right|}\widehat{\widetilde{S^*_{ij}}},
\end{aligned} \tag{2.14}$$

where, $\langle\cdot\rangle$ denotes spatial average over homogeneous direction(s) and the caret denotes test filtering. Test filtering is defined by the linear interpolation from face values of a control volume, which is again the interpolation from two adjacent cell center values (see Park and Mahesh [47]):

$$\widehat{\phi} = \frac{1}{N_{\text{face}}} \sum_{\text{no of face}} \phi_f = \frac{1}{2N_{\text{face}}} \sum_{\text{no of face}} (\phi_{icv1} + \phi_{icv2}), \tag{2.15}$$

where N_{face} is the number of faces for a given control volume.

2.3 Numerical method

The numerical method is a predictor-corrector approach developed by Gnanaskandan and Mahesh [43] to simulate cavitating flows on unstructured grids.

2.3.1 Predictor step

In the predictor step, the governing equations are spatially discretized using a symmetric non-dissipative finite volume scheme, where fluxes at a cell face are given by

$$\phi_{f_c} = \frac{\phi_{icv1} + \phi_{icv2}}{2} + \frac{1}{2}(\nabla\phi|_{icv1} \cdot \Delta\mathbf{x}^{icv1} + \nabla\phi|_{icv2} \cdot \Delta\mathbf{x}^{icv2}), \tag{2.16}$$

where $\Delta\mathbf{x}^{icv1} = \mathbf{x}_{f_c} - \mathbf{x}_{icv1}$, and $\nabla\phi|_{icv1}$ denotes gradient defined at $icv1$, which is computed using a least-squares method. The viscous fluxes are split into compressible and incompressible contributions and treated separately. Once the fluxes are obtained, a predicted value $\hat{\mathbf{q}}_j^{n+1}$ is computed using an explicit Adams-Bashforth time integration as

$$\hat{\mathbf{q}}_j^{n+1} = \hat{\mathbf{q}}_j^{n} + \frac{\Delta t}{2}\Big(3RHS_j(\hat{\mathbf{q}}^n) - RHS_j(\hat{\mathbf{q}}^{n-1})\Big), \tag{2.17}$$

where RHS_j denotes the jth component of the right-hand side of the governing equations after spatial discretization, and the superscript n denotes the values taken at nth time step.

2.3.2 Corrector step

The corrector step uses characteristic based filtering to compute final solution $\mathbf{q}_j^{n+1}$ from the predicted value $\hat{\mathbf{q}}_j^{n+1}$ as

$$\mathbf{q}_{j,cv}^{n+1} = \hat{\mathbf{q}_{j,cv}^{n+1}} - \frac{\Delta t}{V_{cv}} \sum_{faces} (\mathbf{F}_f^* n_f) A_f, \tag{2.18}$$

where F_f^* is the filter numerical flux of the following form:

$$\mathbf{F}_{f_c}^* = \frac{1}{2} R_{f_c} \mathbf{\Phi}_{\mathbf{fc}}^*. \tag{2.19}$$

Here R_{f_c} is the matrix of right eigenvectors at the face computed using the Roe average of the variables from left and right cell-centered values. $\mathbf{\Phi}_{\mathbf{fc}}^*$ is a vector, lth component of which, ϕ^{*l}, is given by

$$\phi_{fc}^{*l} = k \theta_{fc}^l \phi_{fc}^l, \tag{2.20}$$

where k is an adjustable parameter and θ_{fc} is Harten's switch function, given by

$$\theta_{fc} = \sqrt{0.5(\hat{\theta_{icv1}^2} + \hat{\theta_{icv2}^2})}, \quad \hat{\theta_{icv1}} = \frac{|\beta_{fc}| - |\beta_{f1}|}{|\beta_{fc}| + |\beta_{f1}|}, \quad \hat{\theta_{icv2}} = \frac{|\beta_{f2}| - |\beta_{fc}|}{|\beta_{f2}| + |\beta_{fc}|}. \tag{2.21}$$

Here, $\beta_f = R_f^{-1}(\mathbf{q}_{icv2} - \mathbf{q}_{icv1})$ is the difference between characteristic variables across the face. For ϕ_l, Harten-Yee total variation diminishing (TVD) form is used as suggested by Yee et al. [48]:

$$\begin{aligned} \phi_{fc}^l &= \frac{1}{2}\Psi(a_{fc}^l)(g_{icv1}^l + g_{icv2}^l) - \Psi(a_{fc}^l + \gamma_{fc}^l)\beta_{fc}^l, \\ \gamma_{fc}^l &= \frac{1}{2}\frac{\Psi(a_{fc}^l)(g_{icv2}^l - g_{icv1}^l)\beta_{fc}^l}{(\beta_{fc}^l)^2 + \epsilon}, \end{aligned} \tag{2.22}$$

where $\epsilon = 10^{-7}$, $\Psi(z) = \sqrt{\delta + z^2}$ (δ being 1/16) is introduced for entropy fixing and a_{fc}^l is an eigenvalue of the jacobian matrix. The limiter function g_{icv} is computed using minmod limiter. Park and Mahesh [47] and Gnanaskandan and Mahesh [43] proposed a modification to Harten's switch to accurately represent under-resolved turbulence for

single phase and multi phase flow mixtures respectively by multiplying θ_{f_c} with $\theta^{\star}_{f_c}$ given by

$$\begin{aligned} \theta^{\star}_{f_c} &= \frac{1}{2}\left(\theta^{\star}_{icv1} + \theta^{\star}_{icv2}\right) + |(\alpha_{\text{icv2}} - \alpha_{\text{icv1}})|, \\ \theta^{\star}_{icv1} &= \frac{(\nabla \cdot \mathbf{u})^2_{icv1}}{(\nabla \cdot \mathbf{u})^2_{icv1} + \Omega^2_{icv1} + \epsilon}. \end{aligned} \tag{2.23}$$

Details of the numerical method and validation for a variety of flow problems are provided by Gnanaskandan and Mahesh [43].

2.4 Extension of the method

The road-map of the numerical advancements is shown in figure 2.2. The numerical advancements of the current thesis are indicated by the red boxes. The blue boxes indicates the original solver components. As shown in the figure 2.2, the non-dissipative predictor step fluxes and the corrector fluxes from the shock capturing are added in a single step manner and used as a total RHS for physical time integration. The physical time is integrated in an implicit manner using 2nd order backward diffferencing formula (BDF-2). Finally, the pseudo time is preconditioned and converged to zero using the dual-time stepping (DTS) framework. The non-dissipative fluxes are the same as discussed in the original solver, and the shock capturing is modified based on the All-speed scheme. Both the non-dissipative and shock-capturing fluxes are modified according to rotating reference frame approach based on absolute velocity formulation. The rotating frame of reference approach is discussed in section 2.4.1 and the preconditioning with dual-time stepping methodology is discussed in chapter 6.

2.4.1 Rotating frame of reference

Two popular approaches for rotation are : (i) relative velocity formulation and (ii) absolute velocity formulation. Relative velocity formulation involves easier implementation, but creates problems for larger domain sizes (such as used for propulsors) due to the high magnitudes of centrifugal source terms. Hence, we use absolute velocity

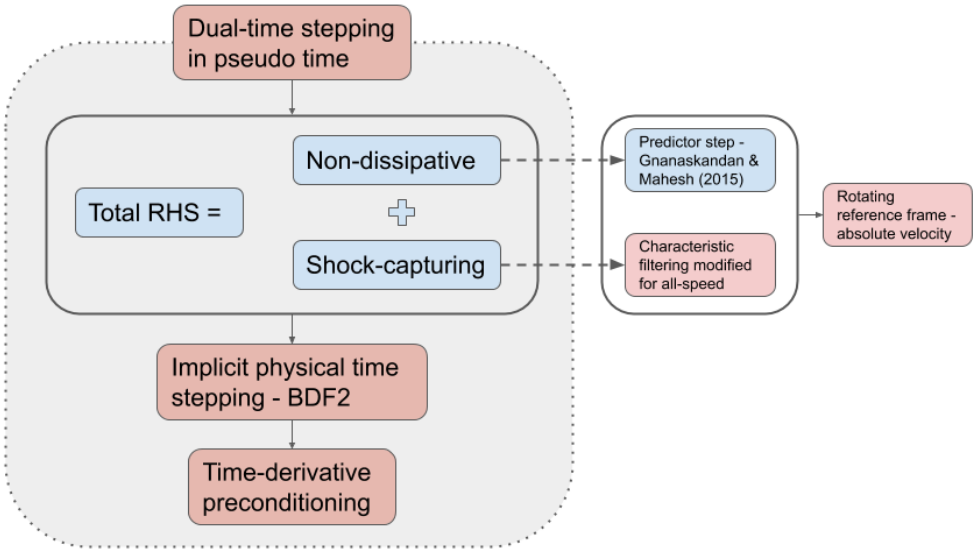

Figure 2.2: Roadmap of the numerical development. Red boxes indicate new developments and blue boxes indicate methodology of Gnanaskandan and Mahesh [43].

formulation, which modifies the force balance in equation 2.13 as

$$\begin{aligned}\frac{\partial \overline{\rho}\tilde{u}_i}{\partial t} = &-\frac{\partial}{\partial x_k}\left(\overline{\rho}\tilde{u}_i\tilde{u}_k + \overline{p}\delta_{ik} - \tilde{\sigma}_{ik} - \tau_{ik}\right) \\ &+ \frac{\partial}{\partial x_k}\left(\overline{\rho}\tilde{u}_i\epsilon_{kjl}w_j x_l\right) + \rho\epsilon_{ijk}w_j u_{r_k}.\end{aligned} \tag{2.24}$$

Here, w is angular velocity of rotating frame of reference. Absolute velocity u is related to the velocity in rotating reference frame (u_r) as $u = u_r + \epsilon_{ijk}w_j x_k$. Equation 2.24 is solved in rotating frame of reference in terms of absolute velocity, therefore it does not involve any contribution due to centrifugal force. This also simplifies the boundary condition implementation as it is now applied to absolute velocity directly. Note that this formulation adds additional contribution due to the Coriolis force and modifies the advection terms in the governing equations 2.13. Changes in the advection terms subsequently requires modification to the shock capturing of the method. Following the approach used by Economan [49] in context of ALE, this additional contribution due to

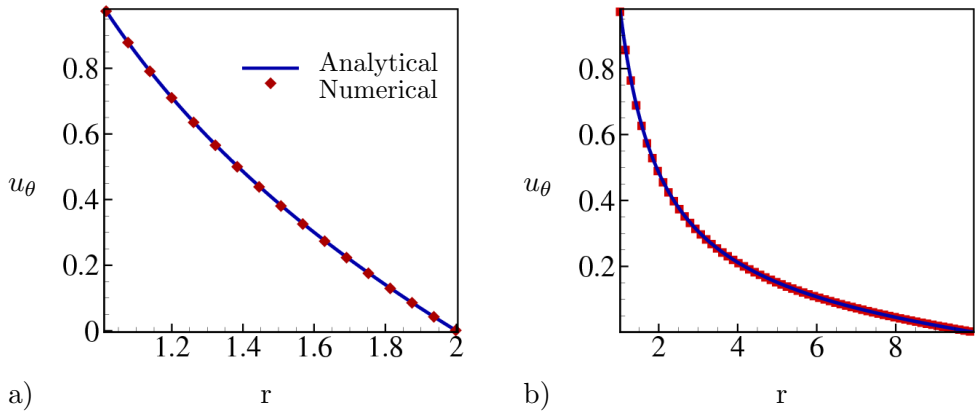

Figure 2.3: Comparison with analytical solution of Taylor-Couette flow for a) smaller and b) extended domain sizes.

rotation indeed only changes the diagonal of the jacobian matrix, which can be fit into the existing framework of the code.

The extension to the rotating frame of reference is validated using the Taylor-Couette problem for two different domain sizes based on the outer radius. $R_i = 1m$ and $R_o = 2m, 10m$ (smaller and extended domains) are radius of inner and the outer cylinder respectively. The outer cylinder is kept stationary in either cases (angular velocity $w_o = 0$) and the inner cylinder is rotated at angular velocity $w_i = 1rad/s$, mimicking the radial domain for propeller shaft rotation without axial velocities. Numerical results for radial variation of azimuthal velocity profiles are compared to analytical solution showing good agreement for both smaller and extended domain sizes in figure 2.3.

Chapter 3

Evaluation of a finite rate homogeneous mixture model

3.1 Introduction

Homogeneous mixture modeling is the most commonly used physical model to study turbulent sheet to cloud cavitation, and the model has shown promising results for capturing the large scale cavitation. However, its performance in predicting the dynamics of resolved small-scale vapor regions is largely unknown. Also, these models employ both finite rate (e.g. Singhal *et al.* [19]) and equilibrium mass transfer (e.g. Schnerr *et al.* [14]) to model phase change. The comparison of such mass transfer rates with the flow time-scale is important for the physical modeling of cavitating flows. We evaluate the performance of the finite rate mass transfer homogeneous mixture model used in the thesis. In particular, the following aspects of the physical model is evaluated: (i) the ability of the model to predict the dynamics of resolved small scale vapor regions, (ii) the effect of the physical length scale of the bubble, (iii) parameters affecting the bubble collapse such as bubble radius, driving pressure, and the dimensionality of the problem, and (iv) the effect of finite rate mass transfer (e.g. on the speed of sound).

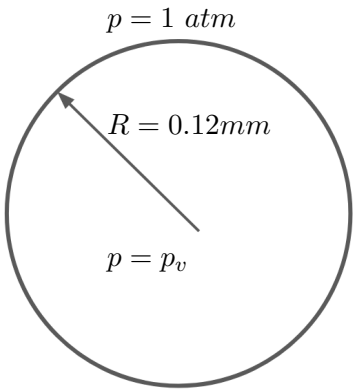

Figure 3.1: Schematic of the spherical bubble collapse validation case.

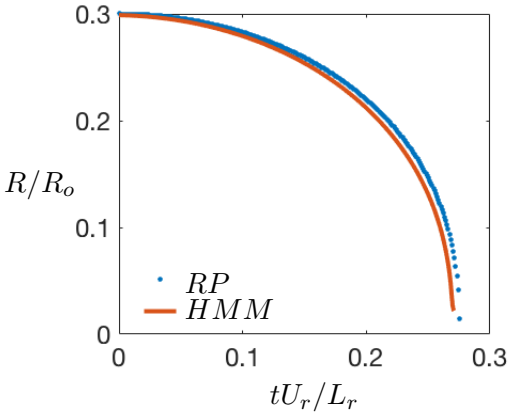

Figure 3.2: Validation of $R(t)$ obtained from the homogeneous mixture model (HMM) with Rayleigh-Plesset (RP).

3.2 Results

3.2.1 Vapor bubble collapse

While it is well known that homogeneous mixture models are reasonably accurate in predicting large scale cavitation dynamics, the final stages of a cloud collapse involve vapor regions of smaller length scales. The performance of homogeneous models in predicting the dynamics of these small-scale vapor regions is evaluated by considering a vapor bubble collapse problem. We consider the collapse of 0.12 mm spherical bubble at ambient conditions as shown in figure 4.2. Evolution of spherical cavity with time can be analytically obtained by solving the Rayleigh-Plesset (RP) equation [50],

$$R\ddot{R} + \frac{3}{2}\dot{R}^2 + \frac{p_\infty - p(R)}{\rho} + \frac{2\gamma}{\rho R} + \frac{4\nu}{R}\dot{R} = 0, \tag{3.1}$$

where ρ is the liquid density, p_∞ is the ambient pressure of liquid, $p(R)$ is the pressure in the liquid at interface. γ is the the surface tension of water. It is 0.072.8 N/m at the ambient temperature of $293K$. $\nu = 1 \times 10^{-6}\ m^2/s$ is the kinematic viscosity of water. The collapse time ($t_{rayleigh}$) can be obtained by integrating the above equation.

We consider a spherical vapor bubble of initial radius $R_0 = 0.12\ mm$ in water with the ambient pressure of $P_0 = 1\ atm$. Pressure inside the bubble is vapor pressure ($P_v = 0.02$ atm at 293 K). The bubble is initialized with the volume fraction of $\alpha_0 = 0.99$ and the free-stream nuclei content is 1×10^{-6} outside the bubble. The reference values considered are $L_r = 0.12\ mm$, $U_r = 10\ m/s$ and $\rho_r = 1000\ kg/m^3$. We consider a complete domain of $10R \times 10R \times 10R$ with a circular sponge layer from $3R$ to $4R$ from the center. The bubble is resolved using only 20 cells along the diameter. The numerical result is compared to the analytical solution of the RP equation in figure 3.2, which shows good agreement for the evolution of bubble radius with time. This suggests the suitability of the model to capture the collapse of 0.12 mm size bubbles.

3.2.2 The effect of physical length scale

The effect of physical length scale is assessed by considering bubble sizes of different orders of magnitudes as $R_o = 0.12\ mm$, $0.12\ \mu m$, $0.12\ nm$. In the homogeneous mixture model, the subgrid-scale bubble dynamics are not considered and the surface tension effects are ignored. Here, we assess the validity of such assumptions at different physical length scales. A comparison to the RP equation for the range of length scales is given in figure 3.3. Also, the RP solution with and without surface tension are considered for the assessment. At $R_o = 0.12\ mm$, a very good agreement among the homogeneous mixture model and RP solutions is obtained (figure 3.3(a)). Also, the RP solution with and without the surface tension has an identical solution. Hence, the assumption for the homogeneous mixture model is valid as long as the bubble is resolved on the grid. As the bubble size is reduced subsequently to $R_o = 0.12\ \mu m$ and $R_o = 0.12\ nm$ the surface tension effects dominate the bubble collapse, as shown in the figures 3.3(b) and 3.3(c).

3.2.3 Paramteric study

We assess various parameters that influence the bubble collapse such as its initial radius, driving pressure, and the dimensionality of the problem.

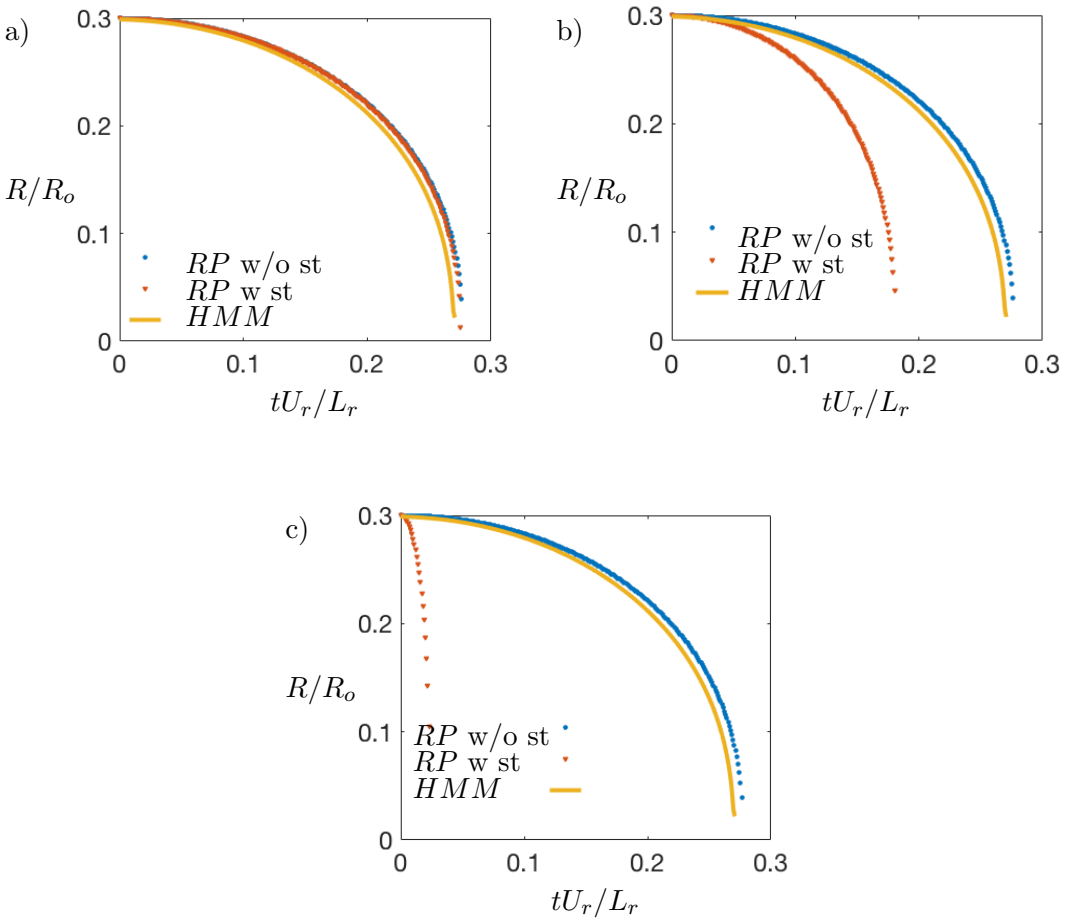

Figure 3.3: Comparison of $R(t)$ with the analytical solution. a) $R = 0.12\ mm$, b) $R = 0.12\ \mu m$, and c) $R = 0.12\ nm$.

Effect of initial radius R_0 and liquid pressure P_0

Parametric studies are conducted for $R_0 = 0.4, 0.2$ and 0.1mm, and $P_0 = 0.5, 1$ and 2 atm. figure 3.4 shows the pressure evolution at the center of the bubble for $R_0 = 0.4, 0.2$ and 0.1 mm. Note that the simulations in this section are conducted using the grid and the domain considered by Bhatt et al. [51], which is different from the validation case. It is observed that both the collapse pressure magnitude and the time taken for collapse (τ_c) reduce as the initial radius is reduced. The larger bubble has more mass to be compressed and hence leads to larger collapse pressure. figure 3.5 shows pressure evolution at the center for $P_0 = 0.5, 1$ and 2 atm. The main consequence of changing P_0 is in changing the initial velocity with which the material front moves (U_0). For the highest P_0, the difference in speed between the material front and the compression wave is negligible and hence the initial pressure peak due to compression is not visible. Further maximum collapse pressure and minimum collapse time are obtained for $P_0 = 2$ atm. It is evident that the higher the pressure gradient ($P_0 - P_v$), the faster the collapse will be, and the higher the collapse pressure.

Comparison of cylindrical and spherical bubble collapse

Here, we consider a case of collapsing cavitation bubble in 2D (i.e. a cylindrical shape bubble with infinite length in spanwise direction) and compare it with a spherical bubble collapse. Interestingly, a spherical bubble of the same size under the same flow parameters generates an order of magnitude higher collapse pressure compared to a cylindrical bubble as shown in figure 3.7. Further, from figure 3.8, we can see that the volume fraction of vapor remaining at the center is much lower for spherical bubble collapse compared to the cylindrical bubble collapse, which shows that condensation strength is higher in the case of spherical bubble collapse. The practical significance of this result is that, 2D RANS simulations will under-predict the condensation strength and collapse pressure.

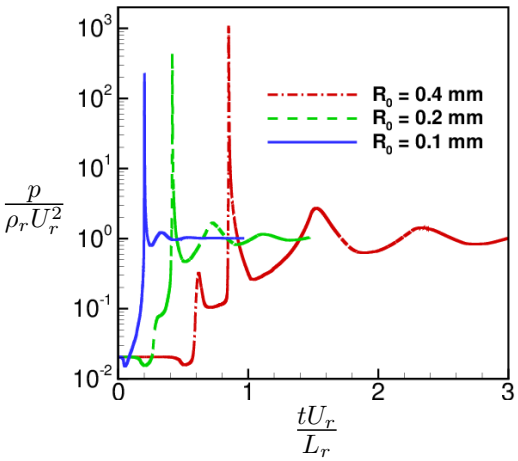

Figure 3.4: Temporal evolution of pressure at center for different initial bubble radius.

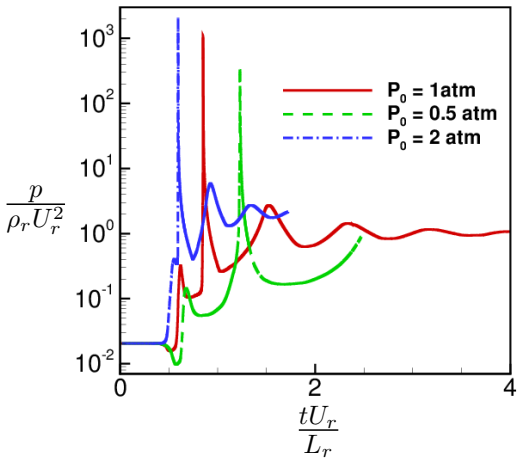

Figure 3.5: Temporal evolution of pressure at center for different ambient pressures.

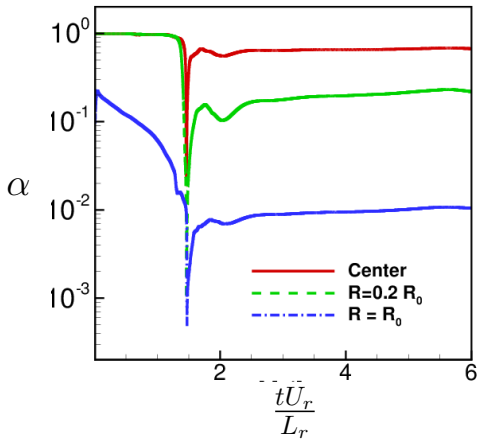

Figure 3.6: Volume fraction evolution at several locations showing residual vapor.

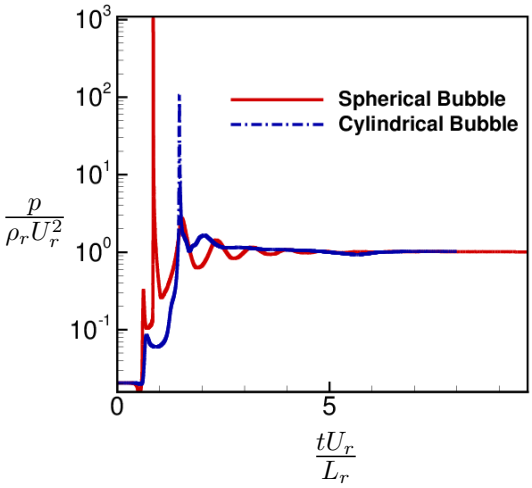

Figure 3.7: Comparison of temporal evolution of pressure at center for spherical and cylindrical bubbles.

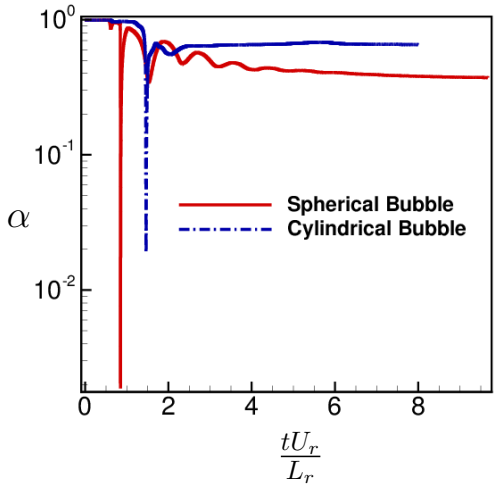

Figure 3.8: Comparison of temporal evolution of volume fraction at center for spherical and cylindrical bubbles.

3.2.4 Effect of finite rate cavitation source terms

Equilibrium models assume mass transfer between phases to occur at rates much faster than that of convection. While this assumption is only valid as long as the mass transfer rates are significantly higher than any other significant flow time-scale. Here, we make a comparison of the mass transfer rate with the advection time-scale for the vapor bubble collapse.

Non-dimensional analysis

The collapse process generates very high pressure and the magnitude of this collapse pressure depends on the relative rate of condensation and convection. In a cavity collapse problem, evaporation term is zero. The non-dimensional mass fraction transport equation is thus given by,

$$\frac{\partial \tilde{\rho} Y}{\partial \tilde{t}} = -\frac{\partial \tilde{\rho} Y \tilde{u_j}}{\partial \tilde{x_j}} - \tilde{S_c}, \tag{3.2}$$

where $\tilde{S_c}$ is the non-dimensional condensation source term. It is given by,

$$\tilde{S_c} = \frac{C_c \alpha^2 (1-\alpha)^2 \max(P - P_v, 0)}{\sqrt{2\Pi R_g T_s}} * (\frac{L_r}{\rho_r * U_r}), \tag{3.3}$$

where α is the void fraction, C_c is an empirical constant, P is the pressure, P_v is the vapor pressure, R_g is the characteristic gas constant of vapor and T_s is the saturation temperature. where L_r, ρ_r and U_r are the reference quantities. Defining a_s as speed of sound in vapor at saturation temperature ($\sqrt{\gamma R_g T_s}$), $\tilde{S_c}$ can be rearranged as a product of three non–dimensional parameters,

$$\tilde{S_c} = (C_c L_r) * (\frac{P - P_v}{\rho_r U_r^2}) * (\frac{U_r}{a_s}) * [\alpha^2 (1 - \alpha^2)]. \tag{3.4}$$

For the bubble collapse problem, the reference length is taken as the initial radius (R_0), and the reference velocity is the initial material front speed $\sqrt{(P_0 - P_v)/\rho_r}$. The non-dimensional source term can be considered as the relative strength of condensation with respect to convection. It can also be construed as the ratio of the convection and condensation time scales. Consequently, these non-dimensional parameters allow us to comment on the rate and strength of collapse. The larger the length scale of the bubble, the higher the driving pressure, and the higher the Mach number; the condensation is stronger. Further, if we interpret in terms of time scales, increasing these non-dimensional parameters decreases the condensation time scale.

3.2.5 Speed of sound with the finite rate mass transfer

One of the most significant influences of finite rate mass transfer is on the mixture speed of sound. As discussed in chapter 2, the speed of sound in the water-vapor mixture lie between the limits of frozen speed of sound (i.e. assuming no mass transfer) and the equilibrium speed of sound (i.e. assuming instantaneous mass transfer). These two limits can have almost two orders of magnitude difference in the speed of sound vale. The derivation of the sound speed in these two limits is given by Franc and Michel [24]. However, the speed of sound including the finite rate mass transfer has not been

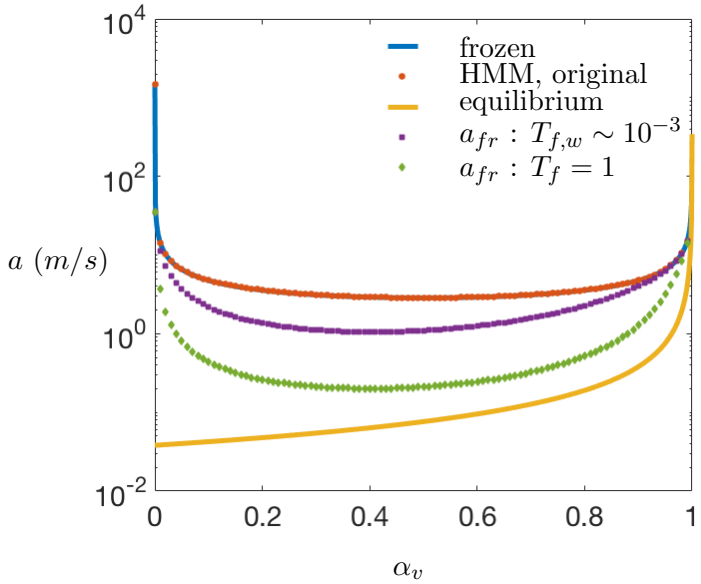

Figure 3.9: Speed of sound with finite rate mass transfer. The equilibrium and the frozen speed of sound is plotted using the analytical expressions in Franc and Michel [24]. HMM, original is the speed of sound obtained from equation 3.5. a_{fr} is the speed of sound with finite rate mass transfer. $T_{f,w}$ is the time-scale for partial cavitation over wedge studied in [36], chosen as an example.

considered previously. In this section, we derive the experssion for speed of sound accounting the finite rate mass transfer using the cavitation source terms. We begin with the isentropic mixture speed of sound derived by Gnanaskandan and Mahesh [43] for the current mixture model as:

$$\begin{aligned} a^2 &= \frac{C_1 T}{C_0 - \frac{C_1}{C_{pm}}}, \text{where} \\ C_0 &= 1 - (1 - Y_v)\rho K_l T \frac{P_c}{(p + P_c)^2}, \\ C_1 &= R_g Y_v + K_l (1 - Y_v) \frac{p}{p + P_c} \text{ and} \\ C_{pm} &= Y_v C_{pg} + (1 - Y_v) C_{pl}. \end{aligned} \tag{3.5}$$

Here, $C_{pl} = 4184.4 J/Kg \cdot K$ and $C_{pg} = 1882 J/Kg \cdot K$ are respectively the specific heats at constant pressure for water and vapor. The derivation of sound speed in the equation 3.5 does not account for the variation in Y_v, which implies no mass transfer between the phases. Hence, it is considered as the frozen speed of sound.

We make use of the finite rate source terms (Saito et al. [16]) to account for the mass transfer effects. C_0 in the equation 3.5 can be modified as $C_0^{'}$, which is given by

$$\begin{aligned} C_0^{'} &= C_0 - p\rho \frac{\partial Y_v}{\partial p} (\frac{1}{\rho_g} - \frac{1}{\rho_l}) \\ &= C_0 + \frac{C_e p \alpha^2 (1 - \alpha)^2 T_f \rho_l}{\sqrt{2\pi R_g T_r} \rho_g}. \end{aligned} \tag{3.6}$$

Here, $C_e = 0.1\ 1/m$ is the empirical constant as in the original source term [16] and $T_f = L_r/U_r$ is the flow time scale. Note that if the $\frac{\partial Y_v}{\partial p}$ is ignored, the expression reduces to equation 3.5. The speed of sound obtained using equation 3.5 with the modifications proposed in equation 3.6 accounts for mass transfer, and it is plotted in figure 3.9. Note that the speed of sound from equation 3.5 matches the frozen speed of sound. Also, with the modification proposed in equation 3.6 the speed of sound can be obtained between the two limits of the frozen and the equilibrium speed of sound as shown in figure 3.9. For $T_f = T_{f,w} \sim 10^{-3}$ (i.e. the flow time-scale for the study of

range of partial cavitation regimes in [36]), the finite rate sound speed (a_{fr}) is closer to the frozen speed of sound value. As the T_f is increased to $T_f = 1$, the sound speed approaches towards equilibrium. This is expected, as the flow now has higher chances to equilibriate within the larger flow time scale. The finite rate sound speed rely on the accuracy of the source terms in the transport equation. The procedure can also be applied to any other cavitation source terms (e.g. Kunz et al. [12], Singhal et al. [19] etc.)

Chapter 4

Partial cavitation regimes over a sharp wedge

4.1 Introduction

Cavitation is termed as 'partial cavitation' when the cavity closes on the cavitating surface. Ganesh et al. [1] characterized partial cavitation over a wedge into incipient, transitory and periodic regimes. A schematic summarizing the characteristics of the regimes is shown in figure 4.1. Incipient cavitation is observed in the separated shear layers and often inside the low-pressure cores of coherent vortices. With further reduction in σ, a sheet cavity forms over the wedge and intermittently sheds as a cloud (referred to as "sheet to cloud" transition) due to formation of a re-entrant jet at the cavity closure. This regime is referred to as the transitory regime. As σ is reduced further, the cavity periodically transitions from sheet to cloud due to the propagation of bubbly shock waves. This regime is termed as the periodic regime. In the present work, we analyze the performance of LES in capturing the physical characteristics of the regimes discussed by Ganesh et al. [1]. The numerical results are used to comment on the differences in the flow field that lead to the formation of either the re-entrant jet or bubbly shock waves. Some of these differences are highlighted in figure 4.1; e.g.

streamline curvature, vapor production, vorticity transport, and collapse-induced pressure waves.

The role of liquid re-entrant jets in sheet to cloud transition has been investigated by various experimental and computational studies [8, 29, 52–59]. Callenaere et al. [8] showed that if the adverse pressure gradient at cavity closure is high enough, a re-entrant jet will develop. They observed two different cavity patterns based on the thickness of the cavity. For thick cavities, the interaction of the re-entrant jet with the cavity is minimal leading to the classical sheet to cloud transition. For thin cavities, re-entrant jet propagation splits the cavity into many small structures. The thin cavity appears rather like a two-phase mixture of approximately constant length. Laberteaux and Ceccio [56] further classified cavities as 'open' or 'closed' based on the absence or presence of re-entrant jet, in their experimental study over a wedge. They described an open cavity as typically frothy without a clear re-entrant jet, while a closed cavity had a sharp interface and exhibited cloud shedding due to re-entrant jet formation. They observed that the flow around the closed cavity was largely irrotational. Gopalan and Katz [55] using particle image velocimetry (PIV) and high-speed videography studied the flow structures in the cavity closure region. They observed that the process of cavity collapse involves roll-up of large hairpin-like vortices and substantial vorticity production. In addition, both Laberteaux and Ceccio [56] and Gopalan and Katz [55] concluded that the adverse pressure gradient is necessary for the formation of re-entrant jet, in line with Callenaere et al. [8].

It is known that the sound speed of the two-phase mixture is orders of magnitude smaller than its constituent phases [24]. Hence, regions in the bubbly mixture are susceptible to the formation of shock waves if the sound speed becomes comparable to the flow velocities. The appearance of shock waves in cavitating flows has been noted by various computational and experimental studies [53, 54, 60, 61]. Recently, the experiments of Ganesh et al. [1] showed bubbly shock propagation as a mechanism for the sheet to cloud transition, in addition to the classically observed re-entrant jet. This motivated various computational studies on the same configuration [29, 45, 62]. Gnanaskandan and Mahesh [29] simulated the experimental configuration of Ganesh et al. [1] in the

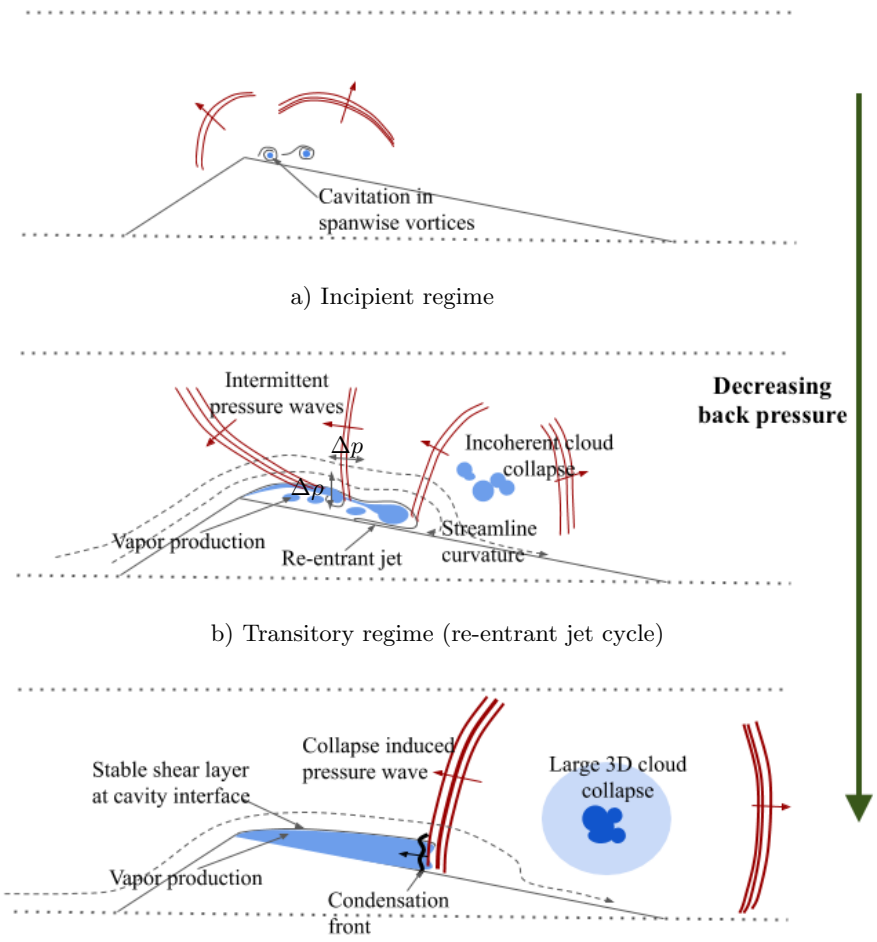

Figure 4.1: Schematic summarizing the continuum over the partial cavitation regimes: a) incipient, b) transitory and c) periodic. Cavity interface is indicated by the solid black line, vapor regions are shown by blue, pressure waves are shown using red lines and streamlines are shown using dashed line followed by an arrow. Note that this is an overall depiction of the regimes and does not necessarily indicate the same instance of time.

transitory regime, using the compressible LES approach. They provided a detailed description of the re-entrant jet induced transition including flow reversal due to adverse pressure gradient, intermittent nature of the pressure waves, and baroclinic vorticity production. However, they do not discuss the bubbly shock wave phenomenon. Budich et al. [45] studied the experimental configuration in the periodic regime using the compressible Euler equation with a barotropic equation of state, capturing the bubbly shock waves in their simulations. In accordance with the experiments, they showed that bubbly shocks are locally supersonic and satisfy the Rankine-Hugoniot jump conditions. However, they do not use a subgrid-scale model and do not discuss the re-entrant jet phenomenon. Schenke and van Terwisga [62] presented a model to capture compressible effects using an incompressible solver with finite rate mass transfer. They also performed simulations in the periodic regime and provided a useful discussion of finite rate mass transfer effects on shedding frequency and vapor content. Experimentally, bubbly shock wave propagation was also observed by Jahangir et al. [63] in partial cavitation inside a nozzle and Wu et al. [64] in a 2D converging-diverging section. Interestingly, Jahangir et al. [63] and Wu et al. [64] observe initiation of the bubbly shock wave by the impingement of collapse-induced pressure waves from previously shed clouds.

Many computational studies have used RANS (Reynolds Averaged Navier–Stokes) models along with the homogeneous mixture assumption for the study of the sheet to cloud cavitation [14, 16, 17, 19, 22, 25]. However, standard RANS models require modifications to eddy viscosity for predicting cloud cavitation [27]. Gnanaskandan and Mahesh [29] compare RANS and LES in the Ganesh et al. [1] configuration and demonstrate that LES shows better results for volume fraction compared to RANS. In recent years, LES has shown promising results for capturing the wide range of scales and unsteady nature of cavitating flows [28–32]. Besides, comparative studies conducted using different turbulence models have also suggested the suitability of LES over other approaches [33–35].

The goals of the present study are to (i) Evaluate the finite rate homogeneous mixture model using compressible LES (Gnanaskandan and Mahesh [43]) over the diverse

range of incipient, transitory and periodic cavitation regimes observed in the experimental configuration of Ganesh et al. [1]. This includes capturing both the re-entrant jet and the bubbly shock waves as instability mechanisms of cloud cavitation. Also, perform a quantitative comparison to the experimental data for the vapor volume fraction, shedding characteristics, and bubbly shock propagation speeds. (ii) Use the LES flow field to investigate the conditions that lead to either the formation of a re-entrant jet or bubbly shock wave. (iii) Study the initiation of the bubbly shock wave by the collapse-induced pressure wave from previously shed clouds.

The chapter is organized as follows. Section 4.2 describes the computational domain, grid, and inflow/outflow comparisons. Section 4.3 discusses the instantaneous solution obtained from LES, comparison to experiments, results comparing different flow regimes and mechanisms governing sheet to cloud transition.

4.2 Problem setup

4.2.1 Computational setup and simulation details

Figure 4.2 shows a schematic of the computational setup. The apex of the wedge is located at $(0, h, 0)$, where h $(1\ inch)$ is the wedge height. The mean flow direction is along the positive x-axis. Flow enters the domain through a $3h \times 3h$ cross-section ($y-z$ plane) which corresponds to the reduced test section in the experiments of Ganesh et al. [1]. The experimental test section is highlighted by $y-z$ planes (in red) towards the inflow and outflow in figure 4.2(a), a magnified view of which is shown in figure 4.2(b). The computational domain is extended upstream for $52.5h$ and downstream for $57h$ from the wedge apex to minimize the reflection of acoustic waves from the boundaries. Besides, acoustically absorbing sponge layers of length $20h$ are applied at both inlet and outlet boundaries as indicated by $y-z$ planes (in green) in figure 4.2(a). This adds an additional term $\Gamma(q - q_{ref})$ in the governing equations (eq.2.1). Here 'q' denotes the vector of conservative variables and the subscript 'ref' denotes the reference solution. In current simulations, the reference solution corresponds to the inlet and the outlet boundary conditions. 'Γ' denotes the amplitude of the forcing. The inflow plane in

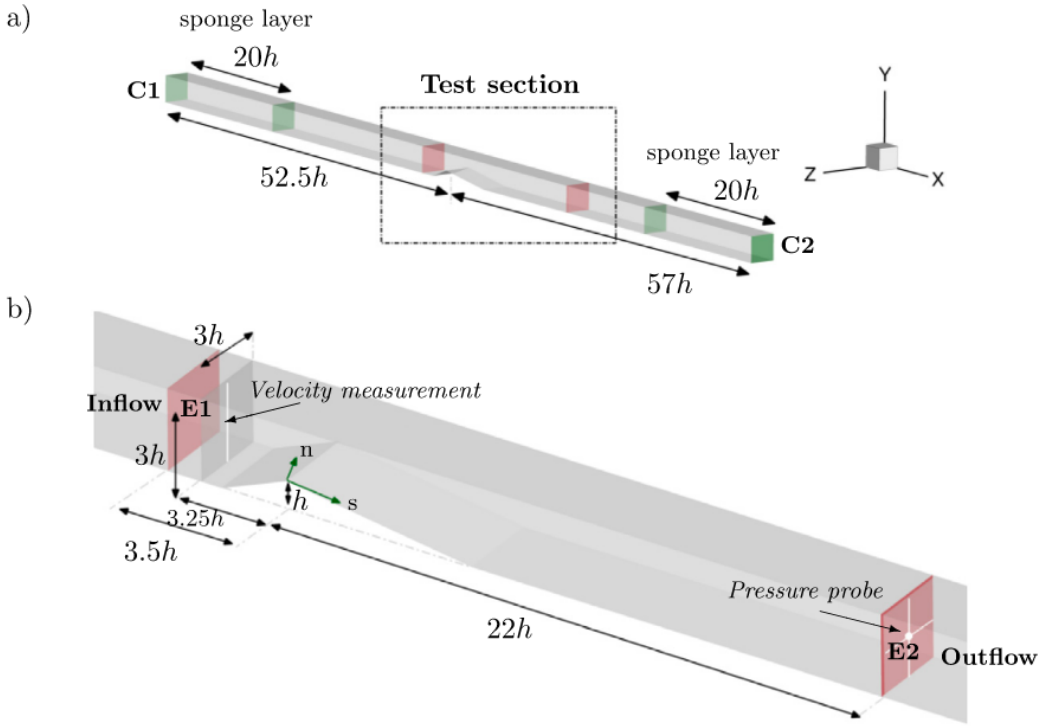

Figure 4.2: Schematic of the computational domain to scale. a) Complete domain and b) magnified view of the test section.

the experiments is located $3.5h$ upstream of the wedge apex and the outflow plane is located $22h$ downstream of the wedge apex as shown in figure 4.2(b). Velocity profile measurements are performed $3.25h$ upstream of the wedge apex. 's' and 'n' denote directions parallel and perpendicular to the wedge surface respectively. The wedge has a contraction angle of 22.1 and a diffuser angle of 8.1. Computational planes at inlet and outlet are indicated by C1 and C2 respectively, and experimental planes for inflow and outflow comparison are indicated by E1 and E2 respectively.

The computational mesh consists of approximately 3 million hexahedral cells. The mesh is refined in the convergent-divergent section of the wedge with a minimum spacing of $0.005h$ ($\sim 0.125\ mm$) in both streamwise and wall-normal directions, near the wedge apex. A wall-normal spacing of $0.005h$ is chosen to sufficiently capture the re-entrant jet. The wall-normal spacing stretches to $0.03h$ ($\sim 0.75\ mm$) at a distance of $0.5h$ (~ 13 mm) normal to the wedge surface to maintain finer resolution within the vapor sheet cavity. Beyond $0.5h$, nearly uniform spacing of $0.05h$ ($\sim 1.3\ mm$) is maintained in all the directions within the divergent section of the wedge. The grid is coarsened beyond the experimental inflow/outflow planes to assist in the dampening of acoustic reflections from computational boundaries.

The flow is simulated at Reynolds number $Re = \frac{\rho_\infty u_\infty h}{\mu_\infty} = 203000$, where the subscript '$\infty$' represents free stream values. Incipient, transitory, and periodic cloud shedding is considered with changes in σ_b. Details of the time step, total run time, number of shedding cycles for each regime are presented in table 4.1. Note that this only includes the simulation time after initial transients have subsided and cloud shedding is established.

4.2.2 Inflow/outflow comparison

Computational inlet C1 is located upstream of the experimental inflow E1 and similarly, computational outlet C2 is located downstream of the experimental outflow E2. Hence, boundary conditions cannot be directly prescribed based on experimental values at E1 and E2, instead, computational inlet/outlet (C1 and C2) conditions are iteratively changed to match the inflow/outflow conditions at planes E1 and E2 with the

Regime	σ_b	Time step (tu_∞/h)	Time units	Shedding cycles (approximate)	Total run-time CPU hours (10^5)
Incipient	2.47	1.0×10^{-5}	40 (0.125s)	-	0.82
Transitory	1.89	2.5×10^{-5}	100 (0.3s)	9-10	1.32
Periodic I	1.78	2.5×10^{-5}	160 (0.5s)	10	2.2
Periodic II	1.59	2.5×10^{-5}	160 (0.5s)	8-9	2.2

Table 4.1: Details of simulations conducted.

experiments. To accelerate the process of iteratively prescribing inflow-outflow, the solution is first obtained in a two-dimensional configuration and interpolated along the span to provide initial conditions to the LES. Details of the results obtained in 2D and comparison to the experimental data are given in Bhatt and Mahesh [65]. One could also consider two-dimensional RANS results for initializing LES [29]. The pressure drop across the wedge is different in 2D as compared to the 3D; it has different blockage effects from the sheet/cloud transition and order of magnitude differences in the collapse pressures [51]. Hence, the interpolated solution needs to adjust further to the computational inlet/outlet boundary conditions. This process, however, is quicker than iterating the inlet/outlet directly in the 3D simulations. Results are analyzed after the periodic cloud shedding is established at given inflow/outflow conditions.

Spatially uniform inflow velocity is prescribed at computational inlet C1 and changed iteratively to match the mean inflow velocity at the geometric center of the inflow plane E1 as provided in the experiments. The velocity is averaged for approximately 10 cavity shedding cycles for each regime and compared to experiments in table 4.2. Besides, we compare the velocity profile along the wall-normal direction with Laser Doppler Velocimetry (LDV) data from Ganesh et al. [1] at the mid-line of the $x = -3.25h$ plane indicated in figure 4.2(b). The comparison is shown in figure 4.3. Note that the deceleration of the flow near the bottom wall of the wedge is captured in the numerical results. Also, the profiles are not affected by the cloud shedding regimes and compare well within the experimental uncertainties. Due to the subsonic nature of the inflow, one of the characteristics is directed towards the inlet from within the

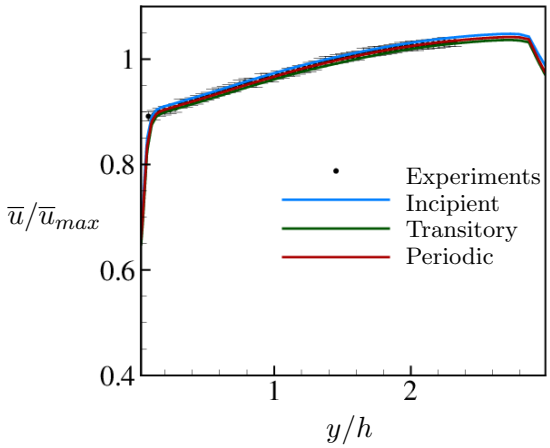

Figure 4.3: Comparison of the inflow velocity profile at velocity measurement plane ($x = -3.25h$ as indicated in figure 4.2(b)) with the LDV measurements of experiments [1].

domain. Hence, pressure cannot be directly prescribed at the inlet boundary. In the simulations, we adjust the back-pressure at computational outlet plane E2 to match the back cavitation number at outflow plane E1. Back cavitation number σ_b is defined as $\sigma_b = \frac{p - p_v(T)}{1/2 \rho_\infty u_I^2}$. Here, u_I is the inflow velocity. σ_b is reduced to progress from incipient cavitation towards periodic cloud shedding as shown in table 4.2. With reduction in σ_b, the experimental uncertainty in u_I and σ_b increases. Numerical values show a good comparison to the inflow/outflow conditions in the experiments. The remaining domain boundaries (top/bottom and span) are treated as walls with no-slip velocity boundary conditions.

4.3 Results

4.3.1 Partial cavitation regimes

We present LES results for incipient, transitory and periodic regimes. The section illustrates how LES captures the physical characteristics of each regime observed in the

	Inflow (E1): u_I (m/s)		Outflow (E2): σ_b	
	Exp.	LES	Exp.	LES
Incipient regime	8.0 ± 0.06	8.1	2.38 ± 0.06	2.47
Transitory regime	7.9 ± 0.09	8.05	1.82 ± 0.06	1.89
Periodic regime I	7.9 ± 0.18	8.01	1.73 ± 0.11	1.78
Periodic regime II	7.9 ± 0.16	8.06	1.60 ± 0.10	1.59

Table 4.2: Inflow/outflow comparison with the experiments. σ_b is obtained from the back pressure values (from direct communication with H. Ganesh).

experiments [1]. We show that in the incipient regime, LES captures the cavitation inside the spanwise vortices. In the developed cavitation regimes, LES captures both the instability mechanisms (re-entrant jet and bubbly shock wave) of the sheet to cloud transition as observed in the experiments.

Incipient cavitation

First, we consider $\sigma_b = 2.47$. An instantaneous solution of the incipient cavitation is shown in figure 4.4. The cavity is indicated by iso-contours of α_v and pressure is plotted on the side plane. Note that no attached sheet cavity is observed at this σ_b, instead, cavitation is observed intermittently downstream of the wedge apex particularly within the shear layer, as the local pressure drops below vapor pressure . Spanwise cavitating structures are observed within the low-pressure cores of rolled-up vortices inside the shear layer (as observed in Ganesh et al. [1]). It is important to distinguish this regime from cavitation inception in that it is a low volume fraction bubbly mixture.

Transitory regime

As σ_b is dropped to 1.89, a vapor sheet cavity forms that is attached to the wedge apex (figure 4.4(a)). There is noticeable variation along the span as evident from the iso-contours of α_v. Vapor volume fraction data is spanwise averaged ($\langle\alpha_v\rangle$) to provide similar visualization as the X-ray measurements. Here, '$\langle\rangle$' denotes spanwise averaged quantities. High levels of vapor production are observed in the shear layer, while the

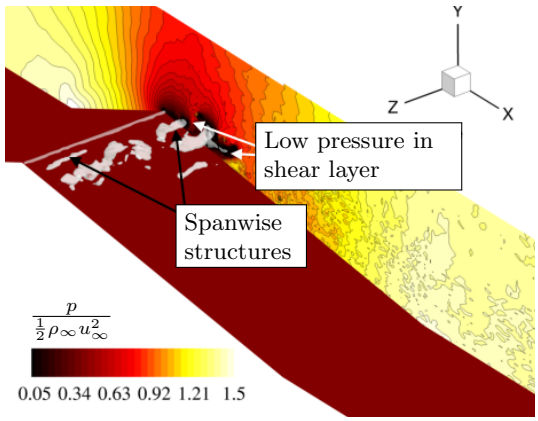

Figure 4.4: Incipient cavitation. Iso-contour level $\alpha_v = 0.1$ with pressure plotted on side plane ($x - y$ plane at $z = 2.9h$).

rest of the cavity displays smaller vapor production and relatively smaller values of $\langle \alpha_v \rangle$ (~ 0.45). A re-entrant jet forms aft of the cavity as the liquid flow re-attaches as indicated in figure 4.4(b). Also, note the cavity perturbation due to the interaction with intermittent pressure waves. Gnanaskandan and Mahesh [29] discuss the intermittent nature of the pressure waves in detail, for the transitory shedding. The re-entrant jet moves upstream towards the mid-cavity leading to the transition of the aft portion of the sheet cavity into the cloud (figure 4.4(c)). $\langle \alpha_v \rangle$ within the cavity remains in the range $\sim$ 0.4-0.6 and vapor production is observed intermittently inside the cavity and shear layer. Spanwise roll-up of the detached cloud and, the subsequent formation of a new vapor sheet cavity are visualized in figures 4.4(d,e). The overall shedding cycle is approximately 20 ms in duration.

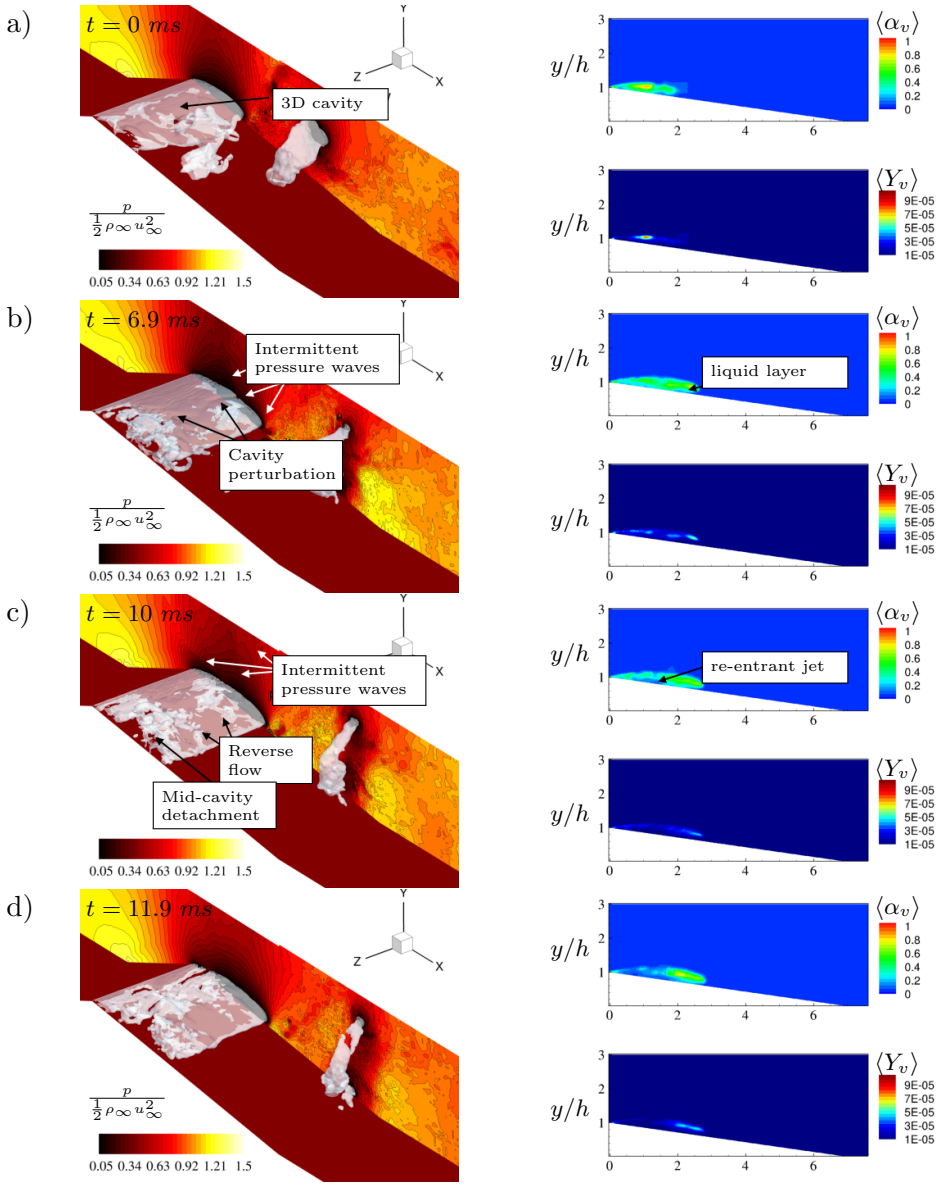
a)
$t = 0\ ms$
3D cavity
b)
$t = 6.9\ ms$
Intermittent pressure waves
Cavity perturbation
c)
$t = 10\ ms$
Intermittent pressure waves
Reverse flow
Mid-cavity detachment
d)
$t = 11.9\ ms$
$\frac{p}{\frac{1}{2}\rho_\infty u_\infty^2}$
0.05 0.34 0.63 0.92 1.21 1.5
Y
Z
X
y/h
$\langle \alpha_v \rangle$
$\langle Y_v \rangle$
liquid layer
re-entrant jet
1
0.8
0.6
0.4
0.2
0
9E-05
7E-05
5E-05
3E-05
1E-05

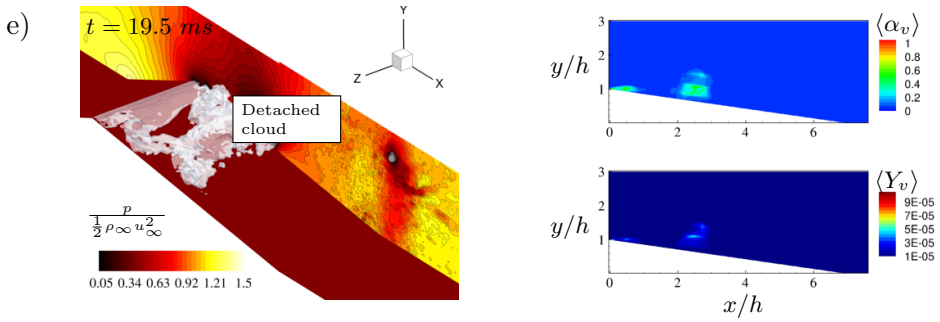

Figure 4.4: Transitory shedding cycle: (On left) Iso-contour level $\alpha_v = 0.1$ with pressure plotted on side plane ($x - y$ plane at $z = 2.9h$) and (on right) spanwise averaged vapor volume fraction ($\langle\alpha_v\rangle$) and vapor mass fraction ($\langle Y_v\rangle$). a) Sheet cavity growth ($t = 0$ ms), b) maximum cavity length ($t = 8$ ms), c) re-entrant jet induced sheet to cloud transition ($t = 10$ ms), d) detached cloud ($t = 11.9$ ms) and e) new cycle of sheet growth ($t = 19.5$ ms).

Periodic shedding

With further reduction in σ_b, the sheet to cloud transition exhibits periodic behavior. We consider periodic shedding at $\sigma_b = 1.78$. Figure 4.4(a) shows the beginning of cavity growth from the wedge apex. The detached cloud from the previous cavity rolls up and advects downstream accompanied by the growth of the vapor cavity (figure 4.4(b)). Figure 4.4(c) shows an instant when the cavity reaches its maximum length. It is interesting to note that the grown cavity is nearly two-dimensional with a stable cavity interface, while three-dimensionality is observed in the cavity closure region and the detached cloud. In addition, high values of $\langle\alpha_v\rangle$ (∼0.8-0.9) are observed inside the entire cavity (also observed in the experiments of Ganesh et al. [1]) along with significant vapor production indicated by $\langle Y_v\rangle$. Complete collapse of the vapor cloud (visible in figure 4.4(c)) is shown in 4.4(d). High-pressure regions due to the cloud collapse are noticeable on the side plane. Collapse-induced pressure waves impinge on the trailing edge of the cavity, initiating the cavity retraction by a condensation front. Spanwise variation in the condensation front as it propagates towards the wedge-apex can be observed in figure 4.4(e). Note that transitory shedding also exhibits condensation

front induced sheet to cloud transition along with the re-entrant jet induced shedding. However, periodic shedding is observed predominantly due to the condensation front propagation. The behavior is apparent at lower σ_b (e.g. $\sigma_b = 1.59$). In the current section, only representative shedding cycles are considered.

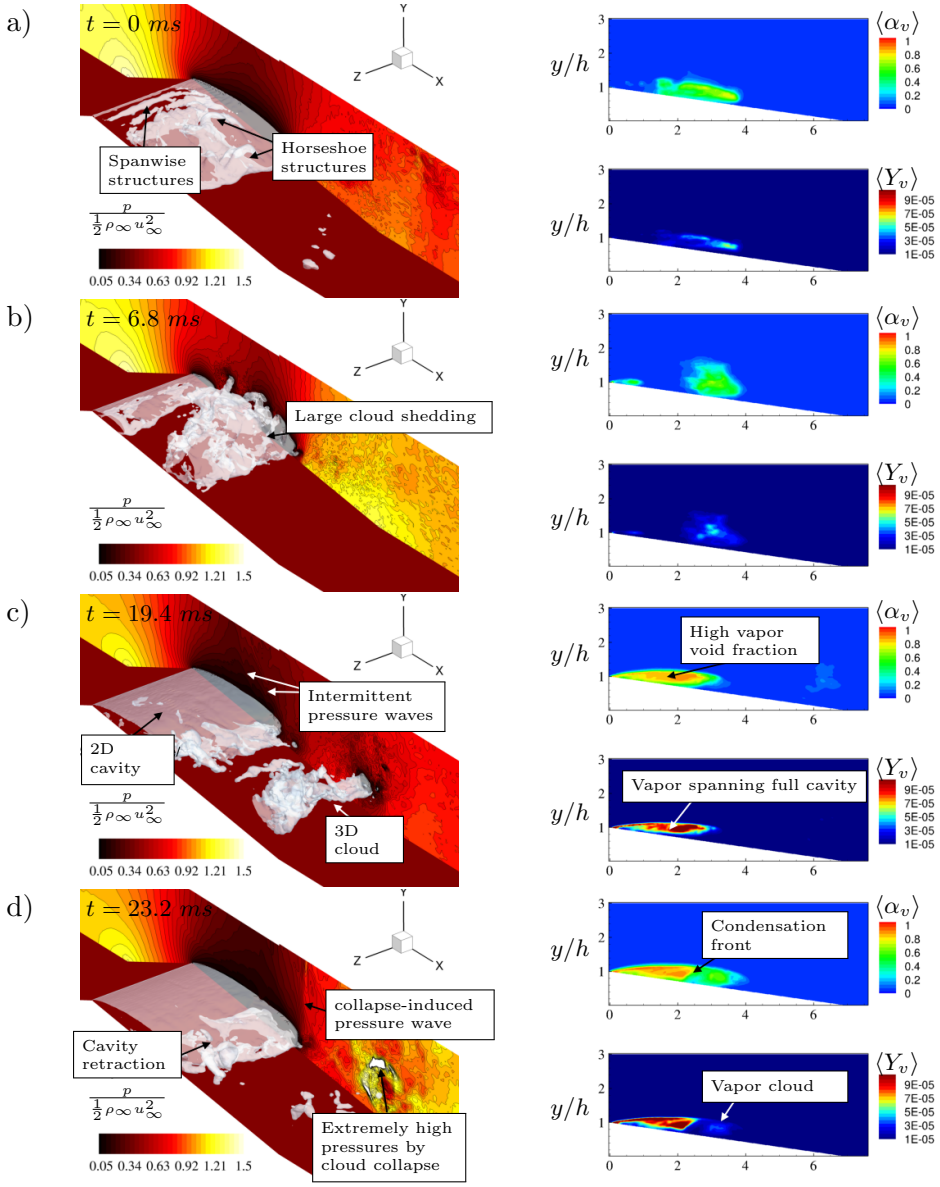
a)
$t = 0\ ms$
Spanwise structures
Horseshoe structures
b)
$t = 6.8\ ms$
Large cloud shedding
c)
$t = 19.4\ ms$
Intermittent pressure waves
2D cavity
3D cloud
d)
$t = 23.2\ ms$
collapse-induced pressure wave
Cavity retraction
Extremely high pressures by cloud collapse
$\frac{p}{\frac{1}{2}\rho_\infty u_\infty^2}$
0.05 0.34 0.63 0.92 1.21 1.5
Y
Z
X
y/h
$\langle\alpha_v\rangle$
$\langle Y_v\rangle$
1 0.8 0.6 0.4 0.2 0
9E-05 7E-05 5E-05 3E-05 1E-05
High vapor void fraction
Vapor spanning full cavity
Condensation front
Vapor cloud

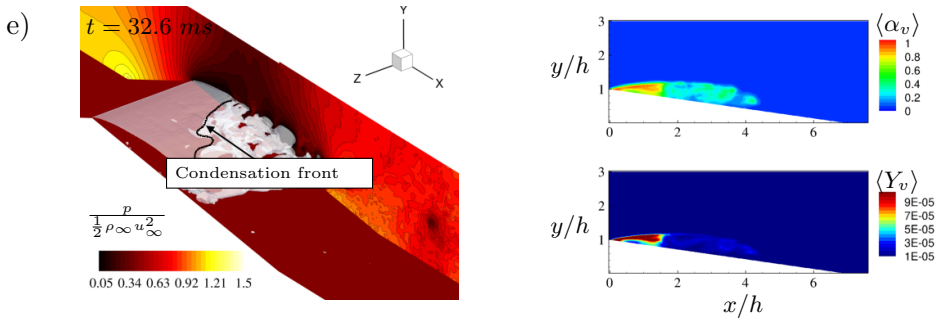

Figure 4.4: Periodic shedding cycle: (On left) Iso-contours level $\alpha_v = 0.1$ with pressure plotted on side plane ($x - y$ plane at $z = 2.9h$) and (on right) spanwise averaged vapor volume fraction ($\langle\alpha_v\rangle$) and vapor mass fraction ($\langle Y_v\rangle$). a) Detached cloud (previous cycle) ($t = 0\ ms$), b) cavity growth ($t = 6.8\ ms$), c) Complete cavity growth ($t = 19.4\ ms$), d) Initiation of cavity retraction ($t = 23.2\ ms$) and e) sheet to cloud transition due to the propagation of condensation front ($t = 32.6\ ms$).

4.3.2 Comparison to the experiments

We compare the mean volume fraction data to the X-ray measurements of Ganesh et al. [1]. Also, we consider the time evolution of instantaneous vapor volume fraction, condensation front speed, and the frequency of periodic shedding for comparison to the experimental data.

Comparison to X-ray densitometry

The mean vapor volume fraction is compared to experiments in figures 4.5, 4.6 and 4.7 for incipient, transitory and periodic regimes respectively. For each case, contours of time average of spanwise averaged vapor volume fractions ($\overline{\langle\alpha_v\rangle}$) obtained from LES are plotted alongside the time averaged X-ray measurement data. Here '$\bar{}$' denotes time average. The field of view of the X-ray measurement is matched to LES and contour levels are identical. In addition, profiles of $\overline{\langle\alpha_v\rangle}$ extracted along the y axis from the wedge surface at various axial locations are plotted in figure 4.5(c), 4.6(c) and 4.7(c). For each case, LES statistics are sampled at $0.005tu_\infty/h$ ($\sim 0.015\ ms$), which provides sufficient temporal resolution to capture variations in cavity size over a given cycle for

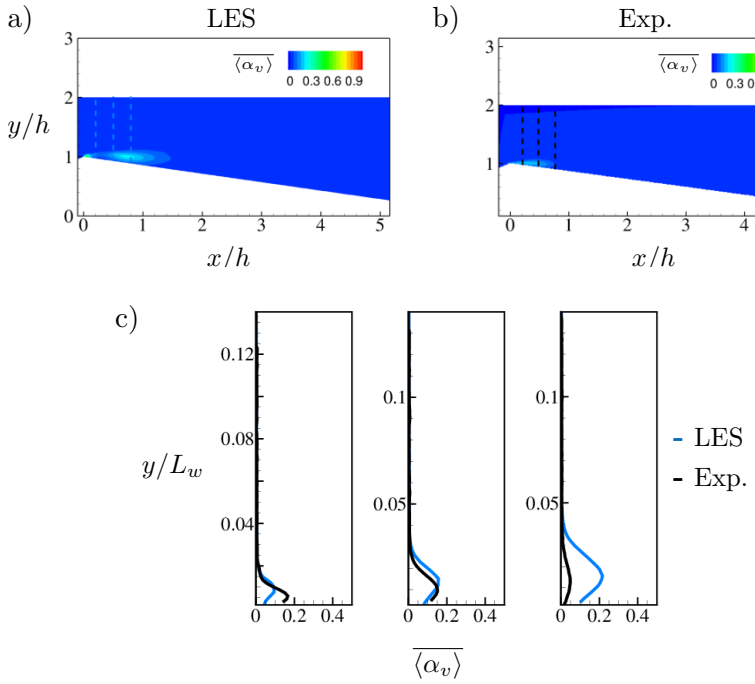

Figure 4.5: Incipient regime : comparison of time average of spanwise averaged vapor volume fraction $\overline{\langle\alpha_v\rangle}$. a) Contours of $\overline{\langle\alpha_v\rangle}$ from LES at $\sigma_b = 2.47$, b) time average of X-ray measurements at $\sigma_b = 2.38 \pm 0.06$ as indicated in table 4.2 (data obtained from direct communication with H.Ganesh) and c) comparison of profiles extracted at $s/L_w = 0.03, 0.06$ and 0.09, indicated by the dashed lines in the contour plots.

Regime	Cavity length (mm)		Cavity thickness (mm)	
	LES	Exp	LES	Exp
Transitory	76.86	75.96	10.18	10.05
Periodic I	102.35	93.38	12.30	11.76

Table 4.3: Comparison of cavity length and thickness based on iso-contour level of $\overline{\langle \alpha_v \rangle} = 0.25$ for transitory and periodic regime.

comparison to the X-ray measurements sampled at 1 ms. Statistics are averaged over approximately 10 shedding cycles (which corresponds to the physical time of $0.5s$ for the periodic shedding case) to capture the low frequency of cloud shedding. Table 4.1 shows details of the total run for each regime. Experimental results are taken for total time of $0.79s$, which corresponds to approximately 16 shedding cycle for periodic shedding.

Figure 4.5 shows the comparison for the incipient regime. Volume fraction levels within the cavity are very small (less than ~ 0.2) both in the simulations and the experiments. The larger cavity in the simulation compared to the experiments can be due to increased sensitivity of the incipient regime to inflow/outflow conditions and free stream nuclei content. Figures 4.6 and 4.7 respectively, show comparison for the transitory and the periodic regimes. In both regimes, as discussed in section 4.3.1, overall larger regions of vapor are formed (e.g. a sheet cavity of vapor over a wedge surface and cloud shedding downstream). Mean volume fractions within the cavity range from ~ 0.3 to ~ 0.6, with higher values particularly within the sheet region. Cavity length/thickness is obtained by considering an iso-contour level of $\overline{\langle \alpha_v \rangle} = 0.25$ both in the experiments and in the simulations and is shown in 4.3. Considering cycle to cycle variation in sheet/cloud cavitation in each regime (also observed in Ganesh et al. [1]) and the unsteady nature of the flow, the comparison in the cavity length and thickness is encouraging. Besides, the distribution of vapor volume fraction in the divergent section of the wedge shows a very good comparison in the free stream, within the cavity and also near the surface of the wedge. This is indicated by $\overline{\langle \alpha_v \rangle}$ profiles in figures 4.6(c) and 4.7(c).

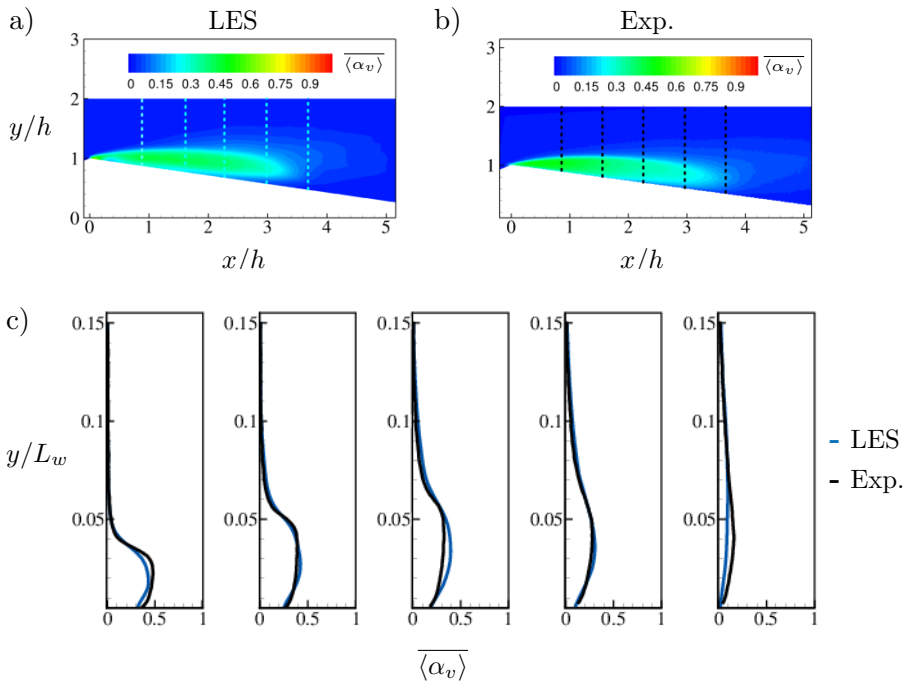

Figure 4.6: Transitory shedding : comparison of time average of spanwise averaged vapor volume fraction $\overline{\langle\alpha_v\rangle}$. a) Contours of $\overline{\langle\alpha_v\rangle}$ from LES at $\sigma_b = 1.89$, b) time average of X-ray measurements at $\sigma_b = 1.82 \pm 0.06$ as indicated in table 4.2 (data obtained from direct communication with H.Ganesh) and c) comparison of the profiles extracted at $s/L_w = 0.1, 0.2, 0.3, 0.4$ and 0.5, indicated by the dashed lines in the contour plots.

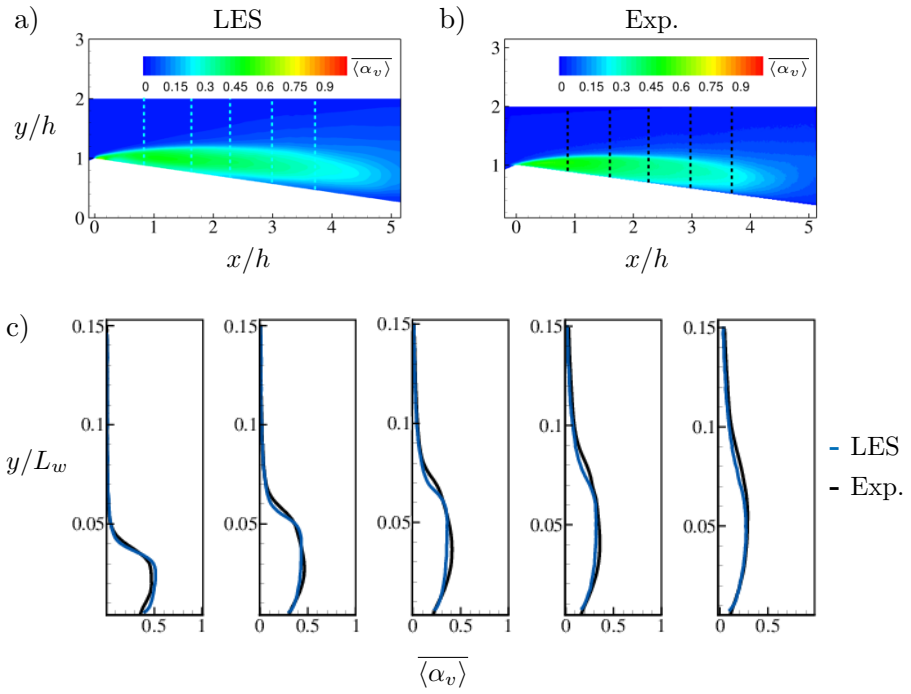

Figure 4.7: Periodic shedding : comparison of time average of spanwise averaged vapor volume fraction $\overline{\langle\alpha_v\rangle}$. a) Contours of $\overline{\langle\alpha_v\rangle}$ from LES at $\sigma_b = 1.78$, b) time average of X-ray measurements at $\sigma_b = 1.73 \pm 0.11$ as indicated in table 4.2 (data obtained from direct communication with H.Ganesh) and c) comparison of the profiles extracted at $s/L_w = 0.1, 0.2, 0.3, 0.4$ and 0.5, indicated by the dashed lines in the contour plots.

Characteristics of shedding and condensation front

The frequency of periodic shedding of the cloud at $\sigma_b = 1.784$ is computed from Fast Fourier Transform (FFT) of the time-varying void fraction and pressure signal at $(3h, 1.5h, 1.5h)$ inside the cavity. The signals for the pressure and the void fraction are shown in figures 4.8(a) and 4.8(b) respectively. The corresponding FFT is shown in figure 4.8(c). The signal shows periodic pressure pulses followed by low pressure (vapor pressure $\sim 2\ kPa$) regions spanning approximately 10 cycles taken over 0.5s. FFT of both the signals (α and p) show peaks at identical values of $f = 20.13Hz$, indicating that the cavity shedding mechanism is associated with the propagation of pressure pulses. The Strouhal number for the cavity shedding is obtained as $St = fL_{cav}/u_I$. Here, L_{cav} is obtained based on iso-contour level $\overline{\langle\alpha_v\rangle} = 0.25$ as defined in section 4.3.2. u_I is shown in table 4.2. We compute St for the experiment in an identical manner to maintain the same definition of L_{cav} and u_I. Table 4.4 shows that shedding characteristics obtained from the LES compare well with the experiments.

The time evolution of cavity shedding over multiple cycles can be analyzed by considering the temporal evolution of the spanwise-averaged flow field. We consider a line parallel to the wedge surface at a normal distance $n = 4\ mm$ and stack the solution for multiple time instances, constructing an $s-t$ diagram. Figure 4.9 shows time evolution of $\langle\alpha_v\rangle$ for LES and X-ray measurement plotted side by side. The triangular region of $\langle\alpha_v\rangle$ indicates 1 cycle of cavity shedding. The cavity growth and collapse within the cycle are indicated by white arrows. Variations in cavity length and vapor volume fraction distribution are observed from cycle to cycle in both the simulation and in the experiment. It is observed that $\langle\alpha_v\rangle$ inside the cavity reaches values greater than 0.75, while regions within the cloud have $\langle\alpha_v\rangle$ in the range $0.25 - 0.5$. Besides, the slopes of iso-contour lines during cavity growth and retraction can be used to compute the respective speeds. The inverse of the slope in the $s-t$ diagram (figure 4.9) for cavity retraction indicates condensation front speed in the laboratory frame of reference. This is, assuming that the flow speed inside the cavity is negligible. Condensation front speed

Shedding characteristics			
Frequency		Strouhal number ($St_{L_{cav}}$)	
Exp.	LES	Exp.	LES
20.00 Hz	20.13 Hz	0.240	0.256

Condensation front			
Shock speed		Sound speed	Mach
Exp.	LES		
4.5 m/s	5.0 m/s	3.34 m/s	1.49

Table 4.4: Comparison of characteristics of shedding and condensation front with experiments.

thus obtained is averaged over 10 shedding cycles for both the experiment and the simulation and good comparison is obtained as shown in table 4.4. The sound speed of high volume fraction liquid-gas mixture is orders of magnitude smaller than its constituent phases. Mach number computed based on the frozen speed of sound is greater than 1. This indicates that the condensation front is supersonic and hence a shock wave. This volume fraction discontinuity traveling at supersonic speed is referred to as a "bubbly shock wave".

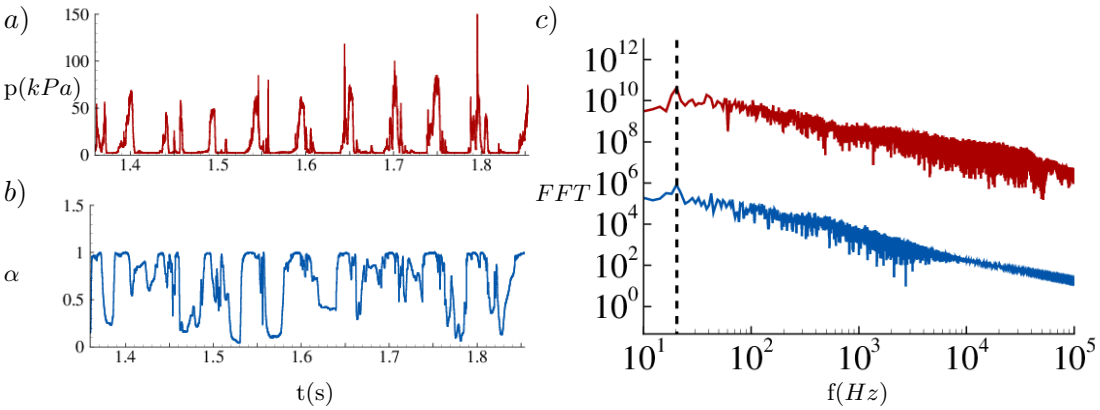

Figure 4.8: Frequency of shedding: a) p(t), b) $\alpha(t)$ taken at $(3h, 1.5h, 1.5h)$ and c) corresponding FFT (p -, α -).

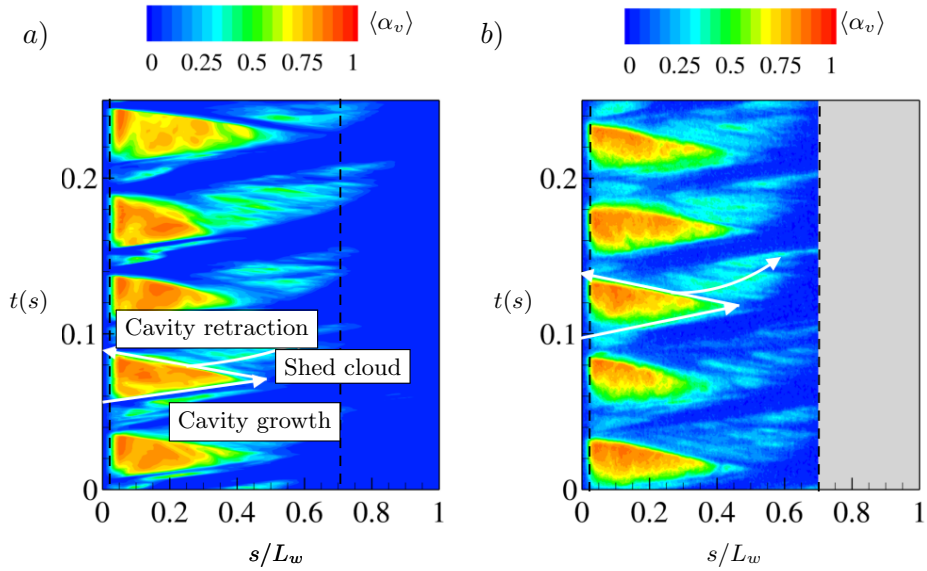

Figure 4.9: Temporal evolution of $\langle\alpha_v\rangle$ taken on a line parallel to the wedge surface at a normal distance $n = 4\ mm$ for $0.25s$ showing approximately 5 cavity shedding cycles. a) LES, b) X-ray measurements (from direction communication from H.Ganesh). Black dashed line is used to indicate the wedge apex and edge of X-ray measurement frame.

	Regime	Transitory	Periodic I	Periodic II
	Streamline curvature	17.19	10.56	4.2
$\overline{p}_{s_2} - \overline{p}_{s_1}$ (kPa)	LES	18.37	11.15	5.9

Table 4.5: Pressure estimation from streamline curvature.

4.3.3 Conditions favoring the formation of re-entrant jet or bubbly shock waves

We consider the effect of reducing σ_b on the mean flow-field in the developed cavitation regimes (transitory, periodic I, and periodic II). We discuss conditions favoring the formation of either the re-entrant jet or bubbly shock waves through streamline curvature effects, adverse pressure gradient, medium compressibility, and vapor production.

Streamline curvature

Mean pressure contours inside the convergent-divergent section of the wedge are plotted in figure 4.10. Streamlines in the figure are based on the mean flow velocities for each regime. Visibly, with the reduction in σ_b, the mean cavity length increases, and the mean pressure in the divergent section of the wedge decreases. Note that the lowest pressures in the divergent section are observed in the vicinity of the midpoint of the cavity where flow confinement is maximum. Also, note that the streamline curvature reduces with the reduction in σ_b. For periodic regime II (at $\sigma_b = 1.59$), streamlines closer to the cavity are nearly flat. We assess the effect of streamline curvature on the pressure recovery by computing pressure rise normal to the streamlines using the momentum equation in the streamline coordinate system. We simplify the analysis by considering the inviscid momentum equation for the mean flow as

$$\frac{\partial \overline{p}}{\partial n} = \frac{\overline{\rho}\overline{U}^2}{R}. \tag{4.1}$$

Here, R is the radius of curvature, which is approximated as $R(n) = R_{cav} exp^{-(n-n_0)}$. R_{cav} is the radius of curvature at the cavity interface and n_0 indicates co-ordinate at

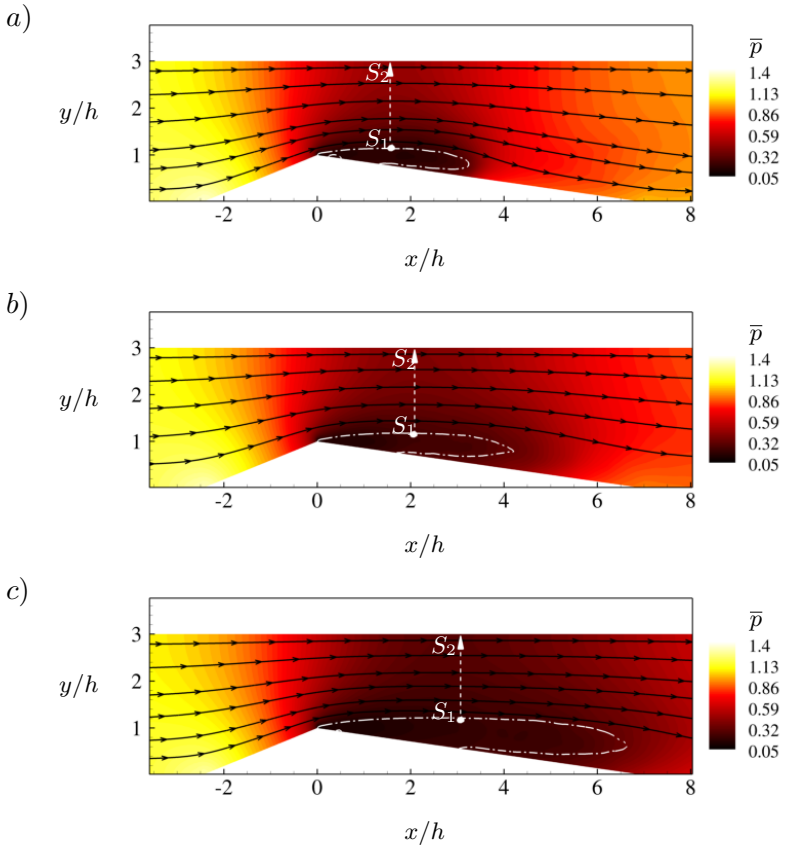

Figure 4.10: Streamline curvature: contours of $\overline{p}$ for a) transitory regime, b) periodic I and c) periodic II. The dotted dashed line indicates the cavity interface and the dashed line indicates the direction along the measurement of pressure rise.

the edge of the cavity. The exponential profile tends to R_{cav} at the cavity interface and to nearly flat streamlines at the top wall. $\overline{U}$ is the mean velocity along the streamlines. Integrating equation 4.1 from the mid cavity to the top wall as shown in figure 4.10, yields corresponding pressure rise normal to the streamlines. Note that higher curvature (lower radius of curvature) and higher mean density results in larger pressure rise (eq. 4.1). Table 4.5 compares the pressure rise obtained from the streamline curvature estimation to the LES results. The simplified streamline curvature estimation compares reasonably to the LES results. Also, the pressure rise in the divergent section reduces significantly as one advances from the transitory to the periodic regime (table 4.5). To summarize, moving from the transitory to the periodic regime, cavity growth leads to reduction in streamline curvature and consequently the reduction in pressure rise. The analysis presented here is for the mean flow. Instantaneously also, one can conceive that the pressure inside the cavity is determined by vapor pressure, and resulting curvature of the cavity influences the pressure rise beyond the cavity into the divergent section of the wedge. Profiles of pressure recovery (for the analysis presented in 4.3.3) from 'S1' to 'S2' are plotted in figure 4.11. The pressure within the cavity is order of few kPa (close to vapor pressure). Periodic shedding II shows that the pressure only recovers as much as $\sim 5kPa$ normal to the cavity (also shown in table 4.5).

Pressure recovery

Here, we compare mean adverse pressure gradient (or pressure recovery) in the cavity closure region for the transitory and the periodic shedding. The analysis to obtain pressure rise based on the streamline curvature as discussed in section 4.3.3 is non-trivial along the axial direction due to the difficulty in accurately estimating curvature and high turbulent intensities. Results obtained directly from the LES are plotted along a line parallel to the wedge surface at a normal distance $n = 4\ mm$ in figure 4.11. Sharp pressure recovery in the transitory regime, compared to the slower pressure rise in the periodic regimes is evident. Hence, a high adverse pressure gradient in the transitory regime favors the formation of the re-entrant jet.

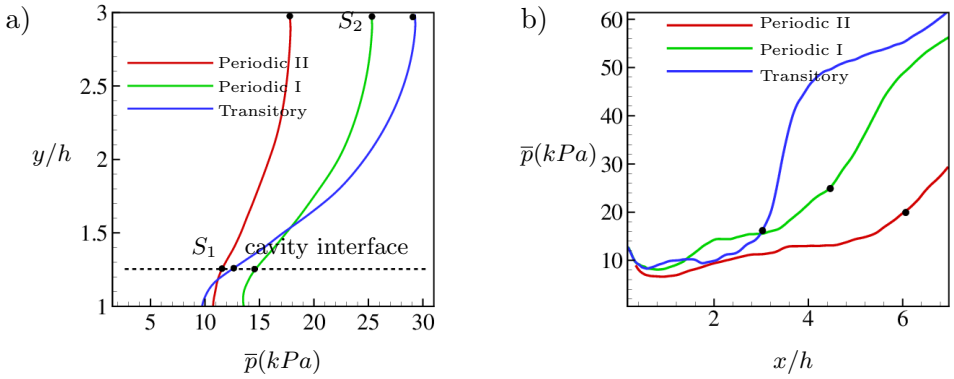

Figure 4.11: Pressure rise a) normal to the cavity at mid-cavity and b) parallel to the wedge surface at a normal distance $n = 4\ mm$ (• indicates cavity closure). Note that cavity interface is indicated by single dotted line only for clarity, minor variations in the interface position exist for different regimes.

Medium compressibility

Next, we consider the effect of pressure recovery on medium compressibility. As discussed earlier, in the periodic regime, pressure recovery is weaker from within the cavity to outside. As a result, relatively low pressure is maintained in the divergent section of the wedge following the cavity. This is shown in figure 4.12(a) by profiles of mean pressure at $y/h = 1.5$ along the convergent-divergent section of the wedge. Significantly lower pressures are observed in the region following cavity closure. Low pressure following the cavity also leads to an increased vapor volume fraction. This forms a bubbly mixture with $\overline{\alpha_v} \sim 0.01 - 0.1$, higher values in the periodic shedding cases (figure 4.12(b)). The vapor volume fraction observed beyond cavity closure can be due to the cloud shedding and the expansion of the free stream nuclei. This low-pressure bubbly mixture results in increased medium compressibility. Consider the variation in the sound speed with vapor volume fraction and pressure (plotted in figure 4.13). Sound speed drops by an order of magnitude in the bubbly mixture with the drop in pressure from 100 kPa to 2 kPa. Besides, higher vapor volume fraction further reduces the speed of sound. As shown in table 4.6, speed of sound at $p = 100\ kPa$ and $\alpha_v = 0.01$ is 106.88 m/s and it drops to as low as 4.7 m/s at $p = 2\ kPa$ and $\alpha_v = 0.1$. Consequently,

P	100 (kPa)			20 (kPa)			2 (kPa)		
α	0.01	0.05	0.1	0.01	0.05	0.1	0.01	0.05	0.1
a	106.88	45.52	33.56	47.89	20.37	15.00	15.15	6.40	4.70

Table 4.6: Sound speed (a in m/s) variation with vapor volume fraction and pressure.

as one moves from the transitory to the periodic regime, the medium becomes more compressible and susceptible to the formation of shock waves.

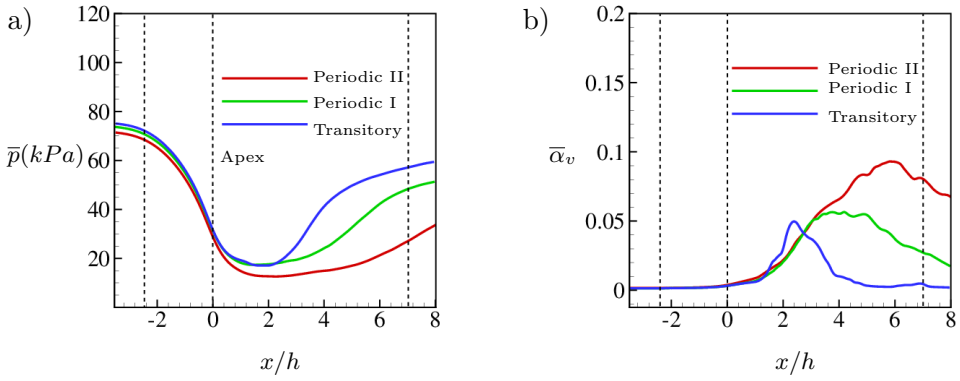

Figure 4.12: Variation in a) mean pressure and b) $\overline{\alpha_v}$ at $y/h = 1.5$ along the convergent-divergent section of the wedge.

Vapor production

We consider the differences in vapor production between the transitory and the periodic regimes. In the transitory regime, vapor begins to form inside the shear layer attached to the wedge apex and also intermittently within the cavity, as instantaneous pressure drops below vapor pressure (figure 4.14(a)). Vapor production averaged over an entire cycle of re-entrant jet-driven sheet to cloud shedding show high values along with the shear layer and at the cavity closure inside the spanwise rolled up cloud (figure 4.14(a)). With a further drop in cavitation number to $\sigma = 1.78$ in the periodic regime, vapor forms over the entire thickness of the cavity as indicated in figure 4.14(b). Vapor production averaged over an entire cycle of the bubbly shock wave is different from the re-entrant

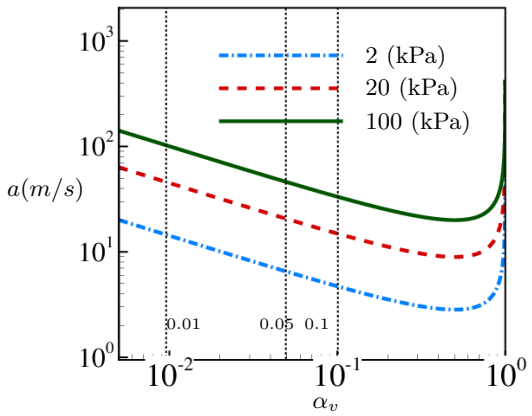

Figure 4.13: Sound speed variation with vapor volume fraction and pressure.

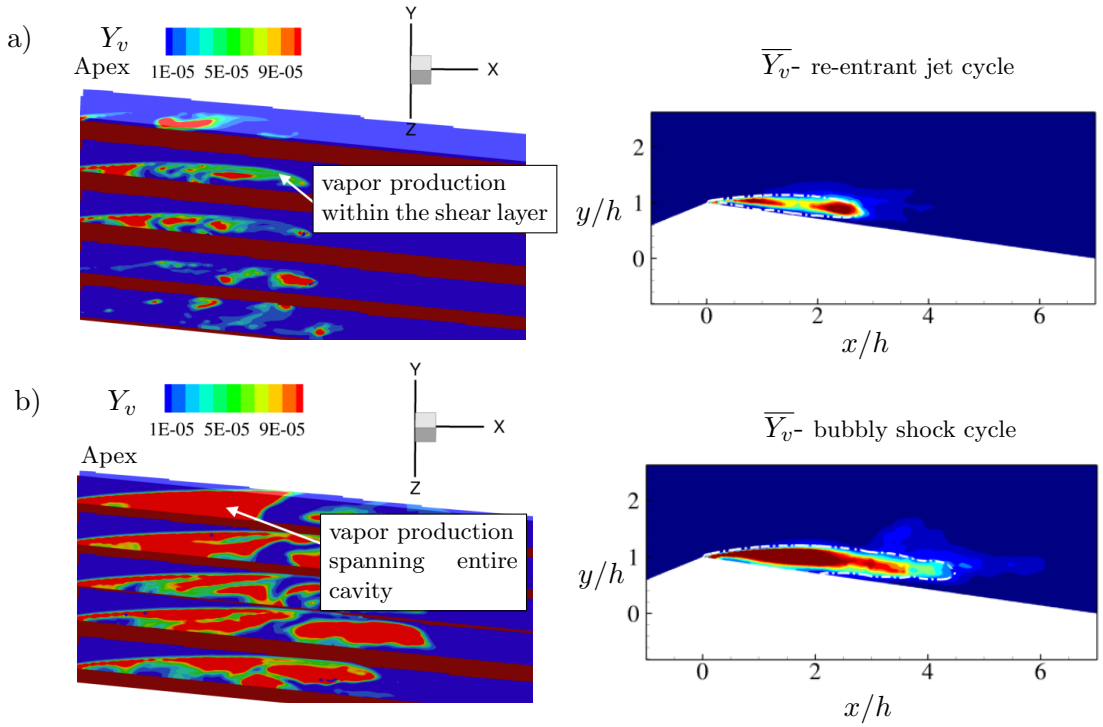

Figure 4.14: Vapor production: On left are the slices along the z-axis showing instantaneous Y_v and on right are the spanwise averaged mass fraction taken over a corresponding shedding cycle in the regime. a) Transitory (re-entrant jet cycle) and b) periodic I (bubbly shock wave cycle).

jet-driven shedding cycle, particularly concerning the overall mass fraction within the cavity. Significant vapor production in the periodic regime leads to a reduction in the speed of sound favoring the formation of shocks. This is also in-line with the observation of high vapor volume fractions (~ 0.9) within the cavity both in the experiments [1] and in the LES.

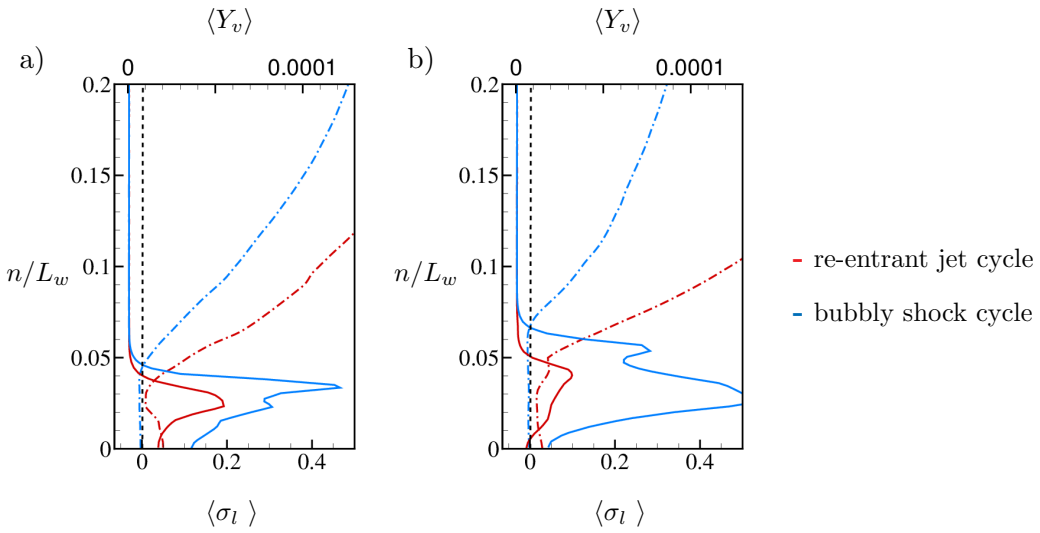

Figure 4.15: Local cavitation number: a) profiles of $\langle \sigma_l \rangle$ and $\langle Y_v \rangle$ taken at $s = 0.1L_w$ normal to the wedge and b) profiles of $\langle \sigma_l \rangle$ and $\langle Y_v \rangle$ taken at $s = 0.2L_w$ normal to the wedge surface. Dotted dashed lines indicate $\langle \sigma_l \rangle$ and solid lines indicate $\langle Y_v \rangle$.

We define local cavitation number as $\sigma_l = \frac{p_{loc} - p_v}{0.5\rho_\infty u_\infty^2}$, where p_{loc} is the local pressure inside a cell. At a given instant if σ_l is below 0, the vapor is produced by the phase change. This also distinguishes the phase change process as compared to only expansion. We compare $\langle \sigma_l \rangle$ and $\langle Y_v \rangle$ within the cavity to identify the distinction between re-entrant jet and bubbly shock cycles. Figure 4.15(a) and 4.15(b) show profiles of $\langle \sigma_l \rangle$ and $\langle Y_v \rangle$ taken respectively at $s = 0.1L_w$ and $s = 0.2L_w$ normal to the wedge for both cycles. For the bubbly shock cycle, $\langle \sigma_l \rangle$ remains less than 0 (nearly constant) spanning the entire cavity, unlike the re-entrant jet cycle where σ_l tends to 0 in the shear layer at the cavity interface and recovers to positive values within the rest of the cavity. Besides, vapor mass production inside the cavity is noticeably higher for the bubbly shock cycle. A nearly constant value of $\sigma_l < 0$ inside the cavity for the bubbly shock cycle can be

explained by considering equation 4.1. With significant vapor inside the cavity, the overall mixture density is an order of magnitude small, and consequently, the resulting pressure difference from equation 4.1 is small. This is unlike the case of the re-entrant jet, where in addition to the low vapor production within the cavity, density recovers by the liquid layer. In either case, regions of the shear layer (at cavity interface) show maximum vapor production. Makiharju et al. [66] indeed observed that injection of non-condensable gas at the apex into the shear layer as compared to the injection at mid-cavity led to a significant reduction in vapor production within the cavity, and consequently influencing bubbly shock propagation.

4.3.4 Origin of the bubbly shock waves

In the periodic regime, we observed that cavity retraction is initiated by the collapse-induced pressure wave. The occurrence of this is evident at lower σ_b. We consider $\sigma_b = 1.59$ (periodic shedding II in table 4.1) to explain this phenomenon. We concentrate only on the part of the cycle visualizing collapse-induced pressure waves and subsequent cavity retraction. The shedding cycle is visualized using instantaneous iso-contours of vapor volume fraction along with pressure on the side plane as shown in figure 4.16. High pressure generated due to the collapse of large vapor clouds (visible in the figure 4.16(a)) is indicated in figure 4.16(b). Collapse-induced pressure waves impinging on the trailing edge of the cavity are visualized in figure 4.16(c). Note that figures 4.16(b) and (c) are only 0.6 ms apart. Subsequently, the retraction of the cavity by a condensation front is visualized in figure 4.16(d). The shedding cycle illustrates the cavity retraction due to the condensation front, initiated by the collapse-induced pressure wave from the previously shed cloud.

Time evolution over multiple cavity shedding cycles can be analyzed by constructing an $s - t$ diagram. We consider spanwise averaged quantities ($\langle \alpha_v \rangle$ and $\langle p \rangle$) along a line parallel to the wedge surface at a normal distance $n = 4$ mm, and stack them for multiple time instants as indicated in figure 4.17. The cavity is indicated by the triangular region. Cavity growth ($\sim t = 0.01s$), cavity retraction ($\sim t = 0.03s$) and shedding of the cloud is indicated by the arrow in figure 4.17(a) (cycles presented in

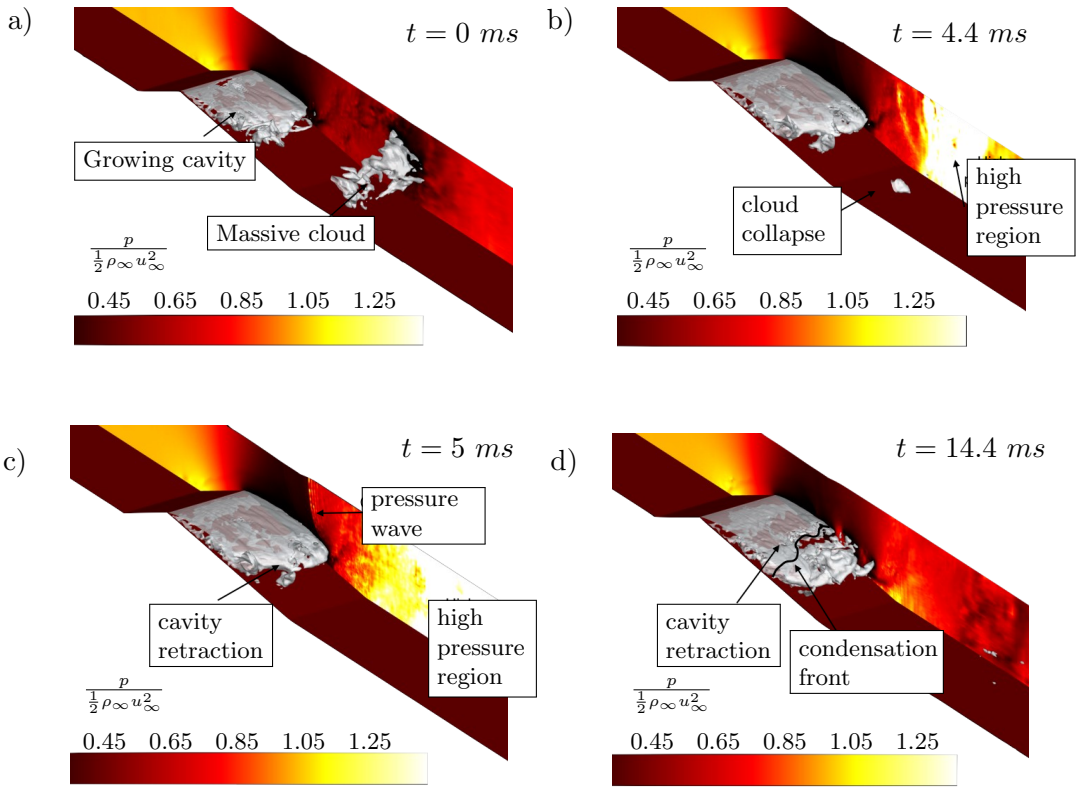

Figure 4.16: Periodic shedding II (shedding cycle): Iso-contours level of $\alpha_v = 0.5$ with pressure plotted on side plane ($x-y$ plane at $z = 2.9h$). a) Growing cavity and previously shedded cloud ($t = 0\ ms$), b) cloud collapse ($t = 4.4\ ms$), c) collapse-induced pressure wave ($t = 5.0\ ms$) and d) retracting cavity ($t = 14.4\ ms$).

the $s-t$ diagram are different from the instantaneous shedding cycle in figure 4.16). The cloud advects downstream as we march in time ($\sim t = 0.05s$). Note that the collapse of the cloud is not visible in the frame considered at $n = 4\ mm$, rather it occurs at a higher normal distance and downstream of the wedge trailing edge. Figure 4.17(b) visualizes the collapse-induced pressure wave impinging on the trailing edge of the cavity (indicated by black arrow $\sim \ t = 0.06s$), and subsequent retraction of the cavity due to the propagation of condensation front (indicated by white arrow $\sim t = 0.06s - 0.08s$). Note the difference in the slopes of the collapse-induced pressure wave and the condensation front. The inverse of the slopes of the line indicates the speeds. As one would expect, the collapse-induced pressure wave travels much faster than the condensation front.

Rankine-Hugoniot jump conditions

Properties across the collapse-induced pressure wave and the condensation front are extracted at the points indicated in figure 4.17(b), and shown in tables 4.7 and 4.8 respectively. Only a representative case is considered. Detailed derivation of Rankine-Hugoniot jump conditions for the current homogeneous mixture system is provided in Brandao et al. [39]. Expression for the shock speed as derived in Brandao et al. [39] is given as:

$$\begin{aligned} S &= u_L - \sqrt{\frac{(p_R - p_L)[\frac{p_R}{p_L}\frac{\overline{\gamma}_R+1}{\overline{\gamma}_R-1}+1]}{(\rho_R-\rho_L)[\frac{p_R}{p_L}+\frac{\overline{\gamma}_L+1}{\overline{\gamma}_L-1}]}}, \\ \frac{1}{\overline{\gamma}-1} &= \frac{C_{vm}p + [C_{vm}+(1-Y_v)K_l]P_c}{[(Y_vR_v)(p+P_c)+(1-Y_v)K_lp]}. \end{aligned} \tag{4.2}$$

Here, 'L' and 'R' respectively refer to the pre-shock and the post-shock states as shown in tables 4.7 and 4.8. It is important to note that essentially both the collapse-induced pressure wave and the condensation front move through a bubbly mixture (not through a completely liquid phase of water). Collapse-induced pressure waves travel through a low void fraction bubbly mixture (~ 0.05) in the shed cloud, while the condensation front moves through extremely high volume fraction regions (~ 0.9) within the cavity. Shock speed obtained for the condensation front using equation 4.2, for the representative case

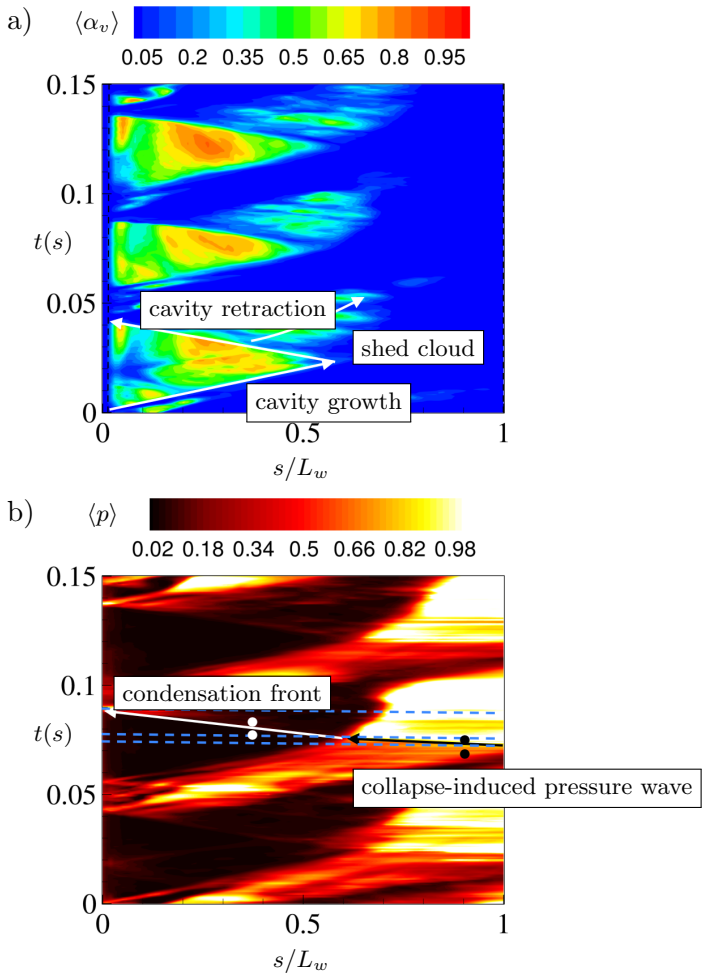

Figure 4.17: Temporal evolution of spanwise averaged quantities taken on a line parallel to the wedge surface at a normal distance $n = 4\ mm$ for $0.15s$ showing approximately 3 cavity shedding cycles. a) $\langle\alpha\ \rangle$ and b) $\langle p\rangle$.

	p (kPa)	ρ (kg/m^3)	u_s (m/s)	
pre-shock (L)	30.83	993.0	4.86	
post-shock (R)	66.92	997.0	4.29	

	Y	a (m/s)	S (m/s)	M_s
pre-shock (L)	1.403×10^{-6}	74.54	-90.9	1.22
post-shock (R)	9.215×10^{-7}	187.2		

Table 4.7: Properties ahead and behind of the collapse-induced pressure wave.

chosen in table 4.8, is -5.438 m/s. It is in close agreement with the mean value of the shock speed obtained from the slope of the $s-t$ diagram and experiments (see table 4.4). Mach number based on the sound speed of $3.88m/s$ ahead of the shock is 1.4, indicating the supersonic nature of the front. In addition, approximately two orders of magnitude jump in vapor mass fraction and an order of magnitude jump in density (see table 4.8) indicate significant condensation of vapor as the front propagates. Accordingly, the front is referred as "condensation shock". A pressure ratio of 2.35 suggests that the condensation shock is a weak discontinuity in pressure (also observed by Ganesh et al. [1] and Budich et al. [45]). Interestingly, the velocity ahead of the shock (u_L) is only -0.29 m/s, which is less than an order of magnitude of the free stream velocity. As equation 4.2 suggests, u_L plays a critical role in determining the shock speed and consequently the nature of the condensation front.

For collapse-induced pressure waves, jumps in the vapor mass fraction and the density are very small. Speed of the pressure wave obtained from equation 4.2 is -90.9 m/s. Mach number based on the sound speed of 74.54 m/s ahead of the shock is 1.22; suggesting the supersonic nature of the pressure wave. This conclusion, however, is subject to some uncertainty due to cycle to cycle variations, probed location, and accurate sound speed value in the low volume fraction bubbly mixture.

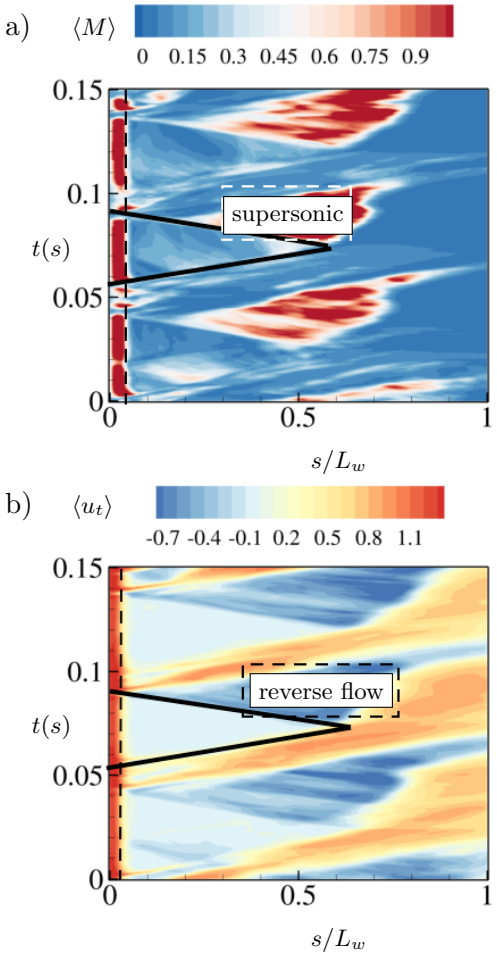

Figure 4.18: Temporal evolution of spanwise averaged quantities taken on a line parallel to the wedge surface at a normal distance $n = 4\ mm$ for $0.15s$ showing approximately 3 cavity shedding cycles. a) $\langle M \rangle$ and b) $\langle u_t \rangle$. Cavity is indicated by triangle shape formed by solid black line.

	p (kPa)	ρ (kg/m^3)	u_s (m/s)
pre-shock (L)	2.23	172.9	-0.27
post-shock (R)	5.248	973.7	-3.32

	Y	a (m/s)	S (m/s)	M_s
pre-shock (L)	1.069×10^{-4}	3.88	-5.438	1.40
post-shock (R)	2.168×10^{-6}	15.74		

Table 4.8: Properties ahead and behind of the condensation front.

Cavity Mach numbers

We consider the time evolution of spanwise averaged Mach number ($\langle M \rangle$) and tangential velocity ($\langle u_t \rangle$) on a line parallel to the wedge at a normal distance $n = 4\ mm$ as indicated in figure 4.18. The cavity is illustrated by the black line. The region immediately following the cavity closure is indicated by a box; note that it is supersonic (figure 4.18(a)), and flow is reversed with a speed comparable to the free stream values (figure 4.18(b)). Interestingly, the cavity itself is subsonic despite the low speed of sound in the high volume fraction mixture (figure 4.18(a)). This is due to the negligible flow velocities within the cavity as shown in figure 4.18(b). This behavior is related to the vapor formation within the cavity in the periodic shedding case. In the periodic regime, it is observed that vapor is formed within the cavity during the cavity growth phase and upon formation, it remains stationary.

4.3.5 Vorticity transport

A comparative study of vorticity transport for the bubbly shock cycle and the re-entrant jet cycle is presented. An instance of maximum cavity growth is considered and contributions of individual terms in the vorticity transport equation are analyzed. The vorticity transport equation is given as

$$\frac{D\omega}{Dt} = \frac{1}{\rho^2}(\nabla\rho \times \nabla p) - \omega(\nabla \cdot u) + (\omega \cdot \nabla)u + \nabla \times \frac{\nabla \cdot \tau}{\rho}. \tag{4.3}$$

The lagrangian time rate of change of vorticity in a given material volume is due to the production of vorticity due to the misaligned pressure and density gradients (baroclinic torque), modulation of vorticity because of the compressibility of the medium, stretching/tilting of the vortex filament in the presence of velocity gradients and viscous stress. Individual contributions are given by the terms on the RHS of the equation 4.3 and plotted in the figure 4.19.

We note two important distinctions between the cycles. First, in the re-entrant jet cycle, vorticity is evenly distributed among the sheet cavity, the closure region, and the cloud downstream; while in the bubbly shock cycle, the region within the fully-grown cavity show low vorticity followed by highly vortical regions in the cloud (figure 4.19(a)). In the bubbly shock cycle, no vortex stretching/tilting is observed within the cavity unlike in the re-entrant jet cycle (figure 4.19(b)). This also confirms the 2D nature of the grown cavity observed in the bubbly shock cycle followed by the 3D regions in the cloud. The highly vortical nature of the flow and wide range of length scales are apparent in either cycle; including horseshoe vortices in the cavity closure region, spanwise vortices at the cavity interface, and streamwise oriented vortices due to the presence of end wall. Second, in the re-entrant jet cycle, vorticity production is observed through the entire length of the cavity at the cavity interface; while in the bubbly shock cycle, this contribution is generally small throughout the 2D cavity and restricted to the cavity closure (figure 4.19(c)). In either case, vorticity dilatation is very significant and observed at the material interface which undergoes a volumetric change in density due to phase change and also within the vapor cloud undergoing compression (figure 4.19(d)).

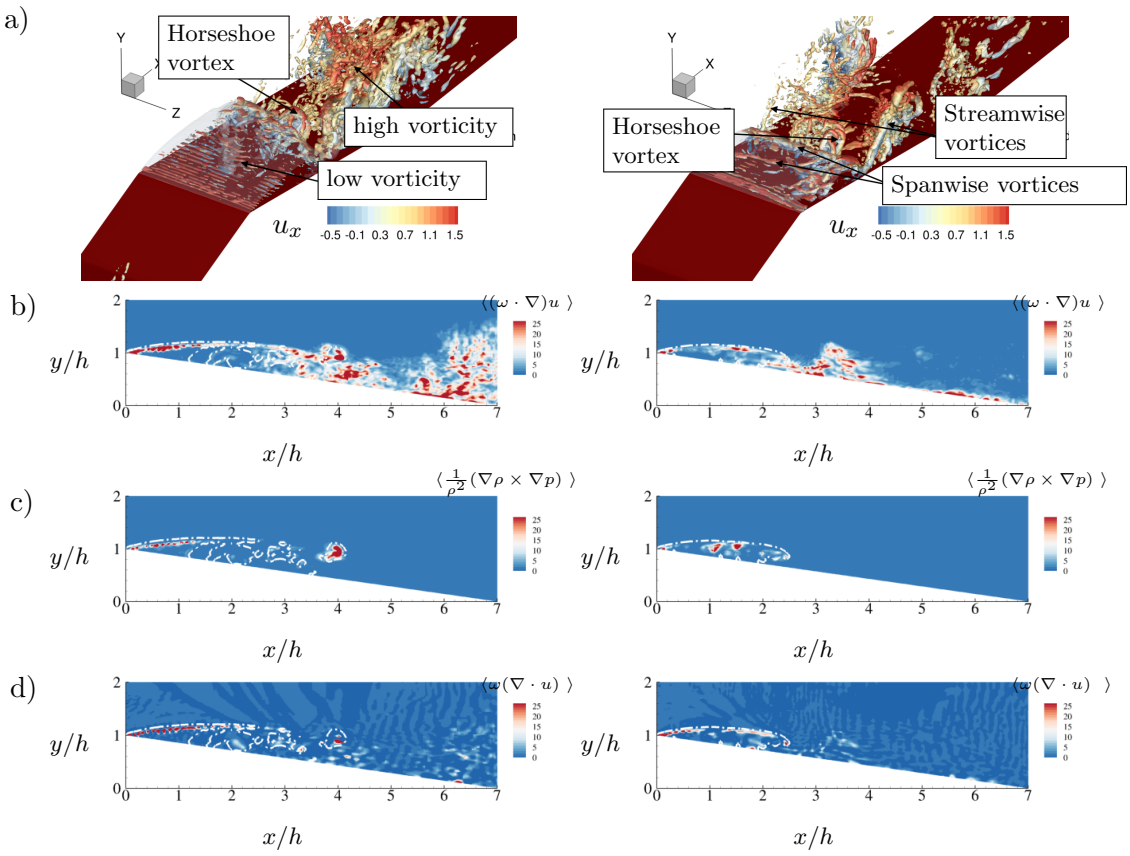

Figure 4.19: Vorticity transport: a) iso-contours of Q-criterion colored by u_x, b) vortex stretching/tilting, c) baroclinc production and d) vorticity dilatation; in the symmetry plane ($z = 1.5$). Maximum cavity growth. Bubbly shock cycle (on left) and re-entrant jet cycle (on right).

Chapter 5

Propeller simulations: need for preconditioning

5.1 Introduction

Recent numerical simulations of the single-phase flow over marine propulsors have shown significant advancement. However, the same is not true for cavitating flows due to the complexity in numerical modeling posed by a range of length and time scales, range of Mach numbers, and multiple types of cavitation phenomena that can co-exist. In SMP-2015, a review of recent advances in both in-house and commercial solvers in predicting cavitation on marine propulsors has been published by Vaz et al. [26] as a part of the Cooperative Research Ships SHARCS project. Numerical methods based on both RANS and coupled RANS–BEM (boundary element method) have been used to predict wetted and cavitating flows over propeller E779A. The study showed good agreement for propeller performance characteristics. Improvement however in predicting cavity extent and pressure fluctuations were deemed necessary. Bensow and Bark [28] studied the flow over the same propeller using a wall-modeled implicit LES approach and demonstrated the need for LES to capture a detailed cavitation flow field for the prediction of cavitation erosion and noise.

Experimental flow over the open propeller P4381 has been studied by Boswell [67],

which will be used for comparison of propeller performance. Numerically the configuration has been studied using the RANS methodology over a wide range of advance ratios by Lindau et al. [68]. Single-phase flow over the same propeller using LES is studied by Kumar and Mahesh [69]. In the present work, we study the experimental configuration using compressible LES with the multiphase flow solver under the wetted conditions. To achieve the propeller rotation, the methodology of Gnanaskandan and Mahesh [43] is extended to solve the governing equations in the rotating frame of reference as discussed in chapter 2. Also, the preconditioning approach (presented in chapter 6) is used for the low free-stream nuclei calculations.

The chapter is organized as follows. Details of the computational grid, domain size, and boundary conditions are described in section 5.2. Assessment of propeller shaft orientation, numerical dissipation, the pressure drop in vortex cores, freestream nuclei, and grid resolution are presented in 5.3 along with the analysis of wetted and thrust torque breakdown conditions of the propeller.

5.2 Problem Setup

The entire computational domain along with a closer view of hub/shaft orientation and corresponding experimental configuration is illustrated in figure 5.1. The domain is a cylinder of diameter $7.0D$ and length $5.5D$, where D is the diameter of the propeller disk. The coordinate system is oriented such that the positive x axis is along the flow direction. Free stream velocities are prescribed at the inflow and far-field lateral boundaries. The pressure is prescribed at the outflow to match the σ in the free-stream. No-slip boundary conditions are prescribed on the walls. The blades and hub rotate with $U = w \times r$, and the shaft is stationary as shown in figure 5.1(b). Angular velocity w is prescribed in order to match the advance ratio, defined as $J = \frac{U}{nD}$, where n is the rotation rate. To avoid reflections of pressure waves from the boundaries back into the domain, we apply an acoustically absorbing sponge layer spanning a distance of D at inflow, outflow, and far-field boundaries. This adds additional term in the governing equations given by, $\Gamma(q - q_{ref})$ [70]. Here 'q' denotes the vector of conservative variables

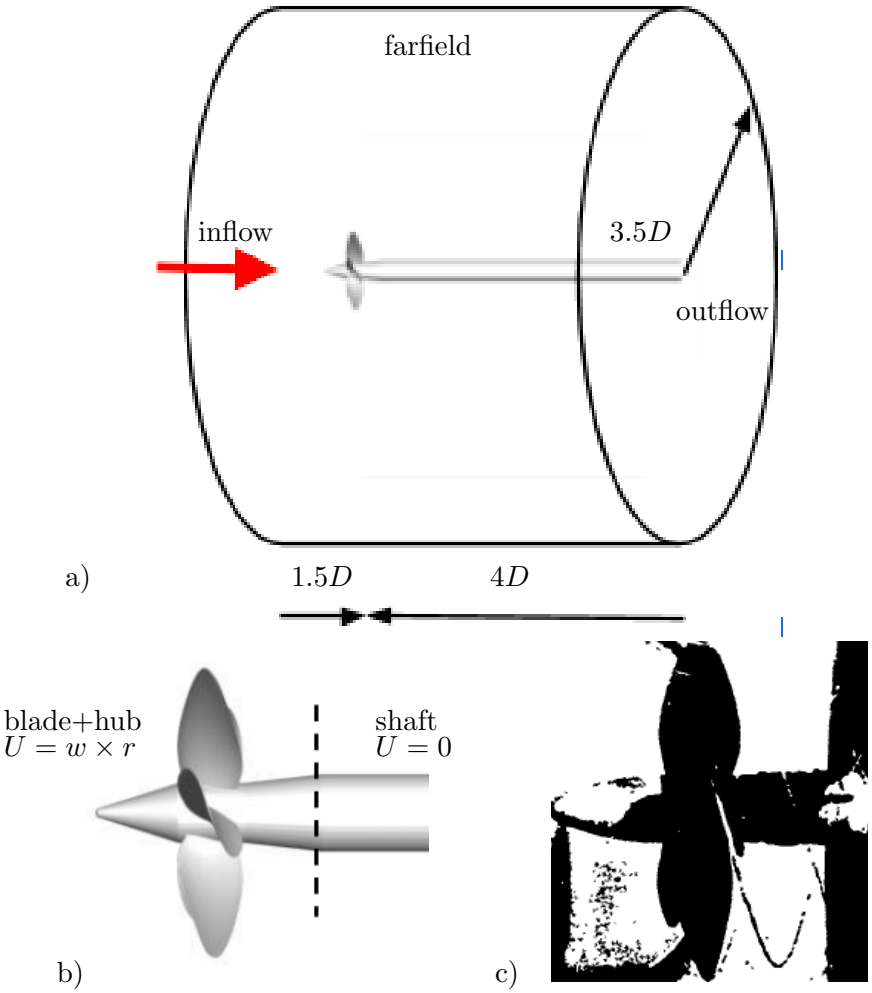

Figure 5.1: a) Complete domain for simulations. b) Closer view of blade, hub and shaft orientation. c) Experimental configuration of Boswell [67] showing $\sigma = 1.4$.

and the subscript 'ref' denotes the reference solution to which the flow is damped, which is free stream values in the cases considered. 'Γ' denotes the amplitude of the forcing.

Also, the grid is coarsened in the far-field to further reduce any reflections. The unstructured grid for the propeller is shown in figure 5.2. Here we consider two different grid sizes $grid1$ and $grid2$, consisting of 11,532,735 and 21,422,580 hexahedral control volumes. The grid is clustered close to the solid surfaces; $grid2$ has a minimum wall-normal spacing of $0.0017D$ on blade, hub, and shaft surfaces. The grids remain finer in the near wake of the propeller and are subsequently coarsened along both the axial

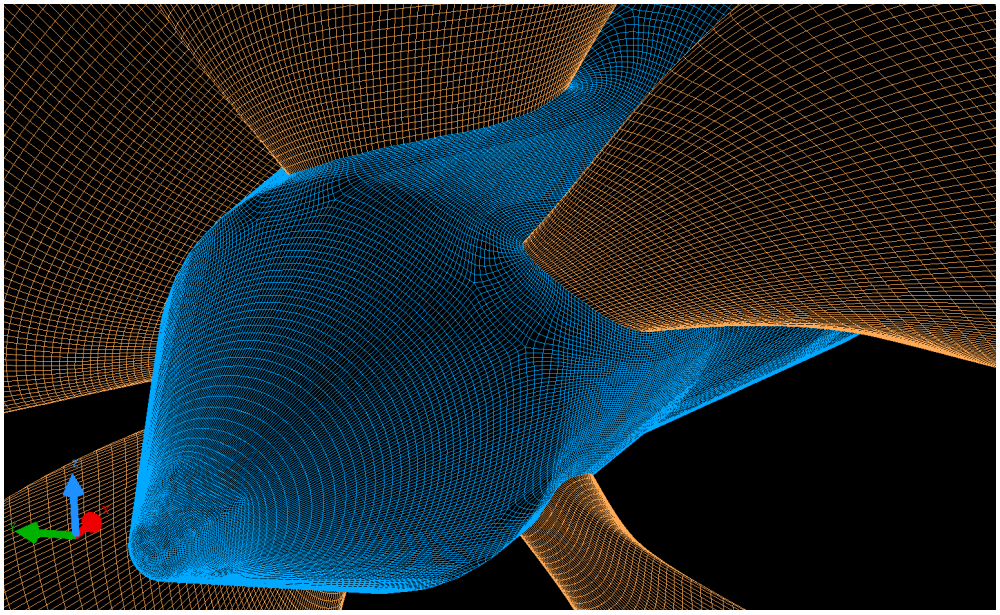

Figure 5.2: Surface mesh near blade and hub.

and radial directions. Blade wake consists of approximately 250 cells along the axial direction past the blade, 110 cells in the radial direction spanning the blade tip, a total of 300 cells in the azimuthal direction.

5.3 Results

Flow is simulated over a marine propeller P4381 at design advance ratio, $J = 0.89$ at a Reynolds number, $Re = 894,000$. The geometric details of the propeller P4381 are reported in Boswell [67]. Reynolds number is defined based on the diameter of propeller disk as $Re = \frac{UD}{\nu}$. The notation used for propeller performance throughout the paper is as follows. Thrust T is the axial component of a force and torque Q is an axial component of the moment of force. Non-dimensional thrust coefficient is defined as

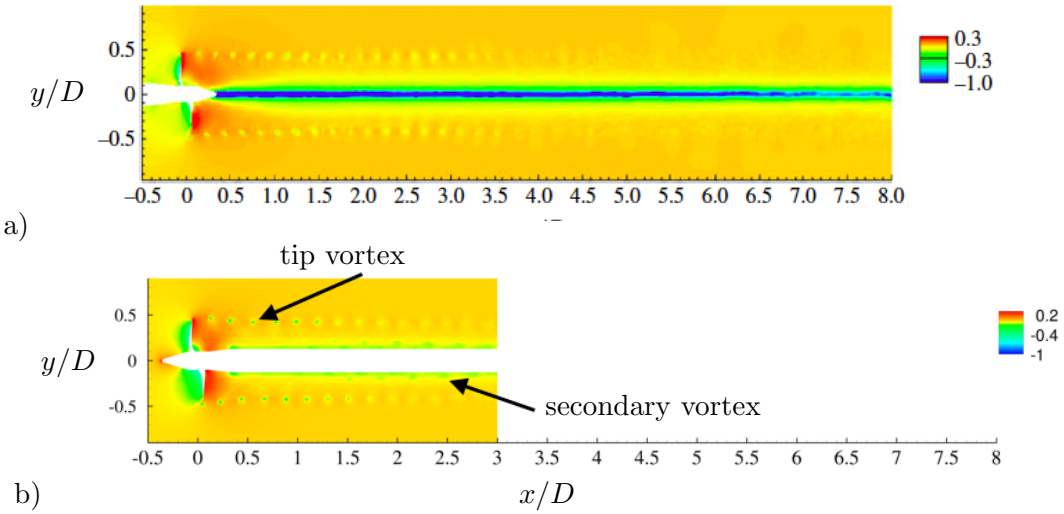

Figure 5.3: Instantaneous pressure field in the xy plane at $z = 0$. a) Kumar and Mahesh [69] and b) current.

Table 5.1: Comparison of propeller performance with change of hub/shaft orientation.

	K_T	K_Q
Kumar and Mahesh [69]	0.21	0.041
hub/shaft flipped	0.22	0.041

$K_T = \frac{T}{\rho n^2 D^4}$ and torque coefficient is defined as $K_Q = \frac{Q}{\rho n^2 D^5}$. Wetted conditions are simulated at high σ (referred to as $\sigma = \infty$ suggesting non-cavitating conditions).

5.3.1 Initialization

In compressible flow solvers, regions of non-zero flow divergence lead to the formation of pressure waves. Due to the sudden start of the propeller, strong compression waves are formed which propagate in the entire domain. In such a case it is undesirable as it not only affects the stability of the solver but also elongates the simulation time due to transients. Hence, to prescribe divergence-free initial conditions for the cavitation solver, the solution is first obtained using in-house incompressible flow solver MPCUGLES (Mahesh et al. [71]) at given Re and J.

Detailed analysis of single-phase flow at the same $Re = 894,000$ and $J = 0.89$ using MPCUGLES is considered by Kumar and Mahesh [69]. In the present work, we match the experimental configuration of Boswell [67] as shown in figure 5.1(c), accordingly the direction of hub/shaft is flipped as compared to the original configuration studied by Kumar and Mahesh [69]. The instantaneous pressure field in the propeller wake for both configurations is compared in figure 5.3. It is noted that when the hub/shaft is flipped, in the absence of hub vortex, vorticity completes itself in the form of secondary vortices near the shaft as shown in figure 5.3(b). Comparison of propeller loads obtained using MPCUGLES for both the configurations is tabulated in 5.1, suggesting that the orientation of hub/shaft has only a nominal effect on overall forces. Torque, in particular, is not affected due to the lower moment arm of the hub/shaft.

5.3.2 Propeller performance

The cavitation code is initialized with the velocity field obtained using MPCUGLES, and pressure is prescribed corresponding to the given cavitation number(σ). Here we present the results for the propeller in the forward mode under wetted conditions on Boswell [67] configuration. The nature of the instantaneous solution is illustrated by iso-contours of axial vorticity as shown in figure 5.4. Coherent vortical structures are evident in the tip vortices along with shedding of vorticity near the blade trailing edge and in the boundary layer on the shaft. The instantaneous flow field in the wake past the propeller blade is visualized by considering the axial velocity profiles in $x - y$ plane at $z = 0$ as shown in figure 5.2. Near field is dominated by coherent tip vortices (also evident from 5.4) and the blade trailing edge wake. As one moves downstream beyond $1.0D$ pockets of blade wake become indistinguishable due to the breaking up of coherent structures in the near field resulting in the flow turbulence and mixing.

A comparison of propeller performance obtained from LES with that of Boswell [67] is presented in table 5.2, showing good agreement in the thrust coefficient and 10% deviation in the computed and experimental torque coefficient.

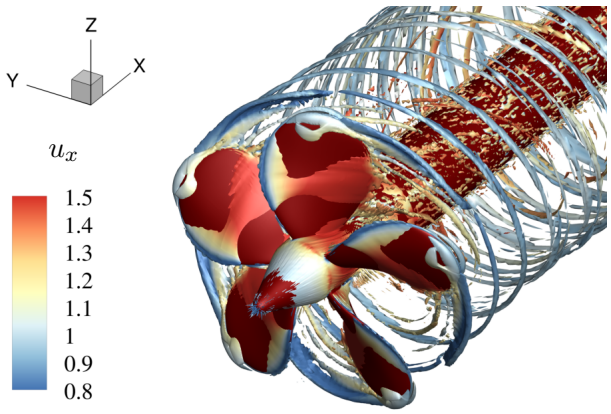

Figure 5.4: Isocontours of axial vorticity colored by u_x.

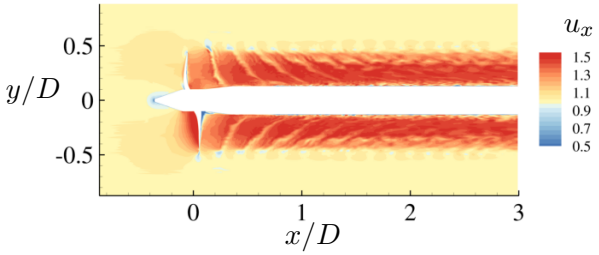

Figure 5.5: Instantaneous solution showing axial velocity.

5.3.3 Shock capturing

First, we assess the sensitivity of propeller performance to the shock capturing scheme. As described in chapter 2, methodology is based on predictor-corrector approach, where predictor step does not explicitly add dissipation and hence in order to capture discontinuites (both shocks and material discontinuity), fluxes are corrected using characteristic based filtering approach where filtered numerical fluxes (i.e. corrected fluxes) are of the

Table 5.2: Comparison of propeller performance under wetted conditions.

	K_T	K_Q
Boswell [67]	0.215	0.045
LES	0.226	0.050

Table 5.3: Sensitivity of propeller performance with shock capturing

	K_T	K_Q
k=5	0.244	0.054
k=1.5	0.257	0.055

following form

$$F^*_{fc} = k\frac{1}{2}R_{fc}\theta_{fc}\phi_{fc}. \tag{5.1}$$

Here, F_{fc} represents corrected flux, R_{fc} is the right eigenvector vector at the face computed using Roe-average of the variables from left and right control volumes. θ_{fc} is the Harten's switch function and ϕ_{fc} has the Harten-Yee TVD form with minmod limiter; see [43] for details.

Here, k is an adjustable parameter. The value of k is problem dependent and its effects on the results are demonstrated by Gnanaskandan and Mahesh [43] and recommended values for a given type of problem are provided by Yee et al. [48]. In brief, extremely small values of k imply negligible dissipation which can lead to oscillations in the solution, whereas larger values lead to dissipation of small scales. In the context of this problem, we assess this by considering $k = 1.5$ and $k = 5$. As shown in table 5.3, the chosen values of k do not have a significant effect on overall propeller performance except for a nominal increase in thrust/torque for $k = 1.5$.

Next, we assess the effect of k on the local flow features particularly of interest such as tip vortices. Figure 5.6(a) displays phase average mean pressure field subtracted from free stream pressure obtained for $k = 1.5$. Pressure extracted along the line passing through the series of tip vortices in the propeller wake as indicated in figure 5.6(a) is plotted in figure 5.6(b). Here, we assess the pressure drop inside vortex cores obtained using an incompressible solution (MPCUGLES), cavitation solver with $k = 1.5$, and $k = 5$. It is observed that as one travels downstream along the propeller wake, the pressure drop inside tip vortices decreases subsequently. It is noted that minor variations in this trend are expected due to the slipstream in the propeller wake, as a result, the extracted line at few locations does not pass exactly through the vortex center.

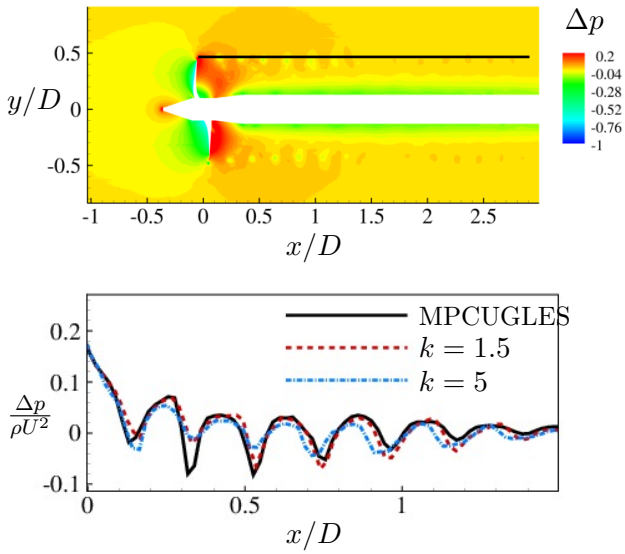

Figure 5.6: a) Phase averaged mean pressure for k=1.5. b) pressure drop along the line extracted at $r = D$ from $x = 0$ to $x = 1.5D$ as indicated in part(a).

Here, the motivation for including an incompressible solution for comparison is bifold; pressure drop from incompressible solution is often used as an indicator to find possible regions of cavitation inception, and in addition to that it also provides the baseline for a non-dissipative solution to assess solution obtained using shock-capturing. It is observed that at lower k (i.e. at $k = 1.5$) closer comparison to MPCUGLES is obtained. This suggests that although the shock-capturing does not have a significant effect on overall propeller performance, to capture local flow features accurately an appropriate assessment is necessary.

5.3.4 Grid resolution

Here, we assess the sensitivity of propeller performance to grid resolution. Table 5.4 shows thrust/torque obtained using $grid1$ and $grid2$ (grid sizes as described in section 5.2), indicating that propeller performance is independent of the grid sizes used.

Figure 5.7 shows instantaneous pressure drop inside vortex cores for two different grids. It is plotted by extracting line passing through tip vortices as shown in figure

Table 5.4: Grid convergence

	K_T	K_Q
$grid1$	0.257	0.055
$grid2$	0.261	0.056

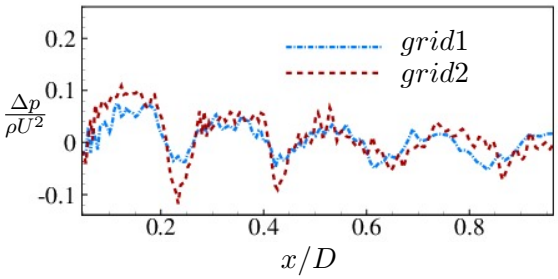

Figure 5.7: Instantaneous pressure drop along the line extracted at $r = D$ from $x = 0$ to $x = 1.5D$.

5.6(a). Note that grids considered here have nearly uniform spacing in the axial, radial, and azimuthal direction in the propeller wake. The axial location of pressure minimum for both the cases is identical up to $0.5D$, however, with the finer grid lower values of pressure minimum are observed. Beyond $0.5D$ the identical values of minimum pressure are observed.

5.3.5 Effect of free stream nuclei

At a pressure lower than the vapor pressure, cavitation is triggered by imperfections in water, that are mostly small non-condensable gas or vapor bubbles (known as cavitation nuclei) and are the starting point for the liquid breakdown [24]. Although these nuclei are usually present in any hydrodynamic system and often unavoidable, their amount and distribution are often not characterized or reported.

In the homogeneous mixture model, these cavitation nuclei are typically prescribed by considering a certain amount of vapor/gas volume fraction through inflow and as initial condition inside the domain. In the present work, we consider three different values of free stream volume fraction (α_∞) 0.1, 0.01, and 0.0001. Standard value of α_∞

Table 5.5: Propeller performance with variation in nuclei concentration

	K_T	K_Q
α_∞=0.1	0.278	0.065
α_∞=0.01	0.257	0.055
α_∞=0.0001	0.226	0.050
Boswell [67]	0.215	0.045

as denoted in the original mass transfer model by Saito et al. [16] is 0.001. However, experimental measurements on background nuclei concentration suggest much lower values.

We assess the sensitivity of the propeller performance with free stream nuclei concentration as tabulated in 5.5. It is interesting to note that the forces acting on the propeller are sensitive to the free stream nuclei. It is evident that with the reduction in α_∞, propeller performance compares closer to the experiments, the smallest value of $\alpha_\infty = 0.0001$ showing the closest comparison. This indicates that under wetted conditions (i.e. under non-cavitating conditions), flow is quite sensitive to the background nuclei concentration. Consequently, for predicting cavitation inception, characterization of cavitation nuclei and its appropriate adaptation in numerical simulations is important.

The sound speed of the compressible homogeneous mixture is sensitive to the small amount of vapor volume fraction in the cell. Changes in α_∞ considered here leads to nearly order of magnitude changes in the sound speed; e.g. $101m/s$ for $\alpha_\infty = 0.01$ to $828m/s$ for $\alpha_\infty = 0.0001$, with lowering of α_∞ sound speed tends toward liquid. Consequently, Mach numbers in the free stream reduce significantly with the lowering of α_∞, resulting in a stiff system due to the large ratio of the acoustic and convective time scales [72]. Non-dimensional time step ($\bar{t} = tU/D$) used for calculations at $\alpha_\infty = 0.1$ of 4×10^{-5}, reduces to 2×10^{-6} at $\alpha_\infty = .0001$. Hence, we make use of the preconditioning methodology to simulate the low free-stream nuclei case in the following section.

Chapter 6

Preconditioning and dual-time stepping

6.1 Introduction

In many cavitation applications, it is essential to capture the propagation of acoustic waves, strong shock waves; therefore, the compressibility of the medium. The shock waves emitted by the vapor cavity collapse are the major cause of noise, vibration, and material damage [24] in marine applications and rotating turbo-machinery. Bubbly shock wave propagation has been identified as the intrinsic mechanism of the sheet to cloud transition [1]. In marine applications, acoustic waves are used as an indicator to detect cavitation inception. Numerical modeling of the compressibility in such problems poses a challenge due to the range of Mach numbers. It is known that the speed of the sound of the pure water can drop by orders of magnitude (e.g. from 1480 m/s to 10 m/s) with the addition of gaseous phase and/or the phase change. Figure 2.1 shows a sharp decrease in the sound speed with the increase in the gaseous phase volume fraction starting from the pure water. Hence, cavitating flows can be highly compressible despite the nearly incompressible nature of the water. In this chapter, we discuss a numerical approach based on the preconditioning and the dual-time stepping (DTS) to address the challenge posed by the range of Mach numbers. The goal of the work is to extend

the current density-based solver that is generally robust at high Mach numbers to the low Mach regimes in the cavitating flows.

One major difference between cavitation solvers based on the homogeneous mixture model is whether they use a pressure-based (e.g. [19]) or a density-based algorithm (e.g. [17]); both of which have to address the range of Mach numbers in the cavitating flows. Density-based algorithms suffer from the accuracy and the numerical stiffness due to the nearly incompressible regions in the water. To mitigate the extremely low Mach regions in the water, several studies based on the fully compressible formulation have used relatively high values of free-stream nuclei [16, 17, 29, 36, 37]. For example, Bhatt and Mahesh [36] studied partial cavitation over a range of regimes spanning the incipient to periodic shedding over a wedge. They obtained a very good comparison of the volume fraction data to the X-ray measurement of [1] for the large regions of vapor in the developed cavitation regimes. However, in the incipient regime, they observed a noticeable difference in vapor void fraction compared to the experiments with the high values of free-stream nuclei. Bhatt and Mahesh [73] showed that the propeller loads are sensitive to the choice of free-stream nuclei and the lower values are necessary for the accurate prediction of the propeller performance. Brandao et al. [39] obtained experimentally consistent behavior of separation location over a range of regimes in the cylinder cavitation with the experimentally consistent values of the free-stream nuclei. The behavior was not captured with high free-stream nuclei content in the prior study of the same configuration [37]. While important for physical modeling, lower values of free-stream nuclei impose a stringent requirement on the time step of the numerical method and affect the solution accuracy. Thus, for the density-based solvers, another approach is to retain low free-stream nuclei and use preconditioning.

Preconditioning applied to the compressible flow equations slows the acoustic wave speed ($u + c$) towards the fluid speed (u); thereby reducing the disparity in the eigenvalues. Preconditioning methods have provided a powerful remedy for the accuracy and convergence of compressible solvers at low Mach [12, 74–81]. Many studies have made use of the preconditioning for single-phase flows. A few studies also report algorithms for multiphase mixtures. Kunz et al. [12] developed a preconditioning formulation in their

two-fluid model using volume fraction as the dependent variable. The authors demonstrated efficient and accurate computations of various steady-state and transient sheet and super-cavity flows. However, in the formulation, they assumed constant densities in each phase and the compressibility effects were not accounted for in the two-phase mixture region. Ahuja et al. [13] developed a preconditioning algorithm accounting for compressibility effects in the component phases and demonstrated results for steady-state flows. Lindau et al. [77] discussed in detail the choice of preconditioning variables and the corresponding eigenvalues of the system for the homogeneous mixture model. Venkateswaran et al. [82] presented the artificial compressibility based formulation for the time-marching system. They used perturbation theory to provide scaled preconditioning forms for the numerical computations. Most of the above studies use pressure-based algorithms originally developed for incompressible flows. The algorithms use Jameson-type artificial dissipation term for the upwinding [83] that is preconditioned as suggested in Turkel [78]. For density-based solvers, Li and Gu [74] proposed an all-speed Roe-type scheme and its asymptotic analysis of the low Mach behavior. They perform preconditioning of the Roe-type shock-capturing schemes by scaling the eigenvalues of the jacobian matrix.

In the present work, we extend the methodology of Gnanaskandan and Mahesh [43] based on a compressible homogeneous mixture model to the low Mach number regimes in cavitating flows. The method has shown promising results for the large scale cavitation in the developed cavitation regimes (e.g. [29, 36]). The goal of the present work is to allow the methodology to simulate wetted conditions, incipient cavitation/cavitation inception regimes that typically require low free-stream nuclei, and consequently the solution involving low Mach regions in the flow. We present a numerical approach based on the preconditioning and DTS to enable such calculations. We precondition the characteristic-based filtering (a Roe-type shock-capturing scheme) as suggested in Li and Gu [74] and use strategies proposed in the prior studies of Lindau et al. [77] and Venkateswaran et al. [82] for constructing the time-derivative preconditioning matrix. The chapter is organized as follows. The details of the preconditioning methodology are discussed in section 6.2. The numerical experiments for the problems of interest are

discussed in section 6.3.

6.2 Preconditioning with dual-time stepping

6.2.1 Vector form of the governing equations

The governing equations (eq.2.1) are recast in the vector form as:

$$\frac{\partial U}{\partial t} + \frac{\partial F_j}{\partial x_j} = S, \quad \text{where}$$

$$U = \begin{pmatrix} \rho \\ \rho u \\ \rho v \\ \rho w \\ \rho Y_v \end{pmatrix}, \quad F_j = F_j^c + F_j^v, \tag{6.1}$$

$$F_j^c = \begin{pmatrix} \rho u_j \\ \rho u u_j + p\delta_{1j} \\ \rho v u_j + p\delta_{2j} \\ \rho w u_j + p\delta_{3j} \\ \rho u_j Y_v \end{pmatrix}, \quad F_j^v = \begin{pmatrix} 0 \\ \sigma_{1j} \\ \sigma_{2j} \\ \sigma_{3j} \\ 0 \end{pmatrix}, \quad \text{and} \quad S = \begin{pmatrix} 0 \\ 0 \\ 0 \\ 0 \\ S_e - S_c \end{pmatrix}.$$

Here, U is the vector of conserved variables, F is the flux vector, F^c is the convective part of the flux vector, F^v is the viscous part of the flux vector, and S is the source vector. δ_{ij} is the Kronecker delta function. For solving unsteady problems using the preconditioning, a pseudo-time derivative term is added to the eq.6.1. The preconditioning is applied to the pseudo-time derivative to preserve the time accuracy of the unteady

problems. The derivative term is written in terms of the time derivative matrix as:

$$\Gamma\frac{\partial Q}{\partial \tau}+\frac{\partial U}{\partial t}+\frac{\partial F_j}{\partial x_j}=S, \quad \text{where} \quad \Gamma=\frac{\partial U}{\partial Q},$$
$$Q=\begin{pmatrix} p \\ u \\ v \\ w \\ Y_v \end{pmatrix}, \quad \text{and} \quad \Gamma=\begin{pmatrix} \rho_p & 0 & 0 & 0 & \rho_{Y_v} \\ u\rho_p & \rho & 0 & 0 & u\rho_{Y_v} \\ v\rho_p & 0 & \rho & 0 & v\rho_{Y_v} \\ w\rho_p & 0 & 0 & \rho & w\rho_{Y_v} \\ Y_v\rho_p & 0 & 0 & 0 & Y_v\rho_{Y_v}+\rho \end{pmatrix}. \tag{6.2}$$

Here, Q is the primitive variable vector. Different choices of the primitive variables are possible (e.g. [12, 77, 82]). Lindau et al. [77] and Venkateswaran et al. [82] has shown that the choice of either α or Y_v as a primitive variable leads to identical eigenvalues of the system. Here, we choose p and Y_v along with the velocity components as the primitive variables. Γ is the jacobian matrix specifying the changes in the conserved variables with respect to the primitive variables. $\rho_p = \frac{\partial \rho}{\partial p}|_T$, which is inverse of the square of isothermal speed of sound ($\frac{1}{c^2}$). Similarly, $\rho_{Y_v} = \frac{\partial \rho}{\partial Y_v}|_T$ is the relative changes in the mixture density with respect to the vapor mass fraction. The expressions of these derivatives are given in A.1. The eigenvalues of the system of equation (eq.6.1) can be obtained from the matrix $A_\Gamma = \Gamma^{-1}A$, where $A = \frac{\partial F}{\partial Q}$ is the convective flux jacobian with respect to the primitive variable vector Q. The matrices A, Γ^{-1} and A_Γ are given in A.2. The eigenvalues of A_Γ are $\lambda_\Gamma = [V_n, V_n, V_n, V_n - c, V_n + c]$. Here, V_n is the velocity normal to the face. Note that in the low Mach regions, V_n is very small compared to c. Hence, the condition number of the matrix A_Γ is very high, which leads to acoustic stiffness. This is a typical condition in water with very low vapor nuclei.

6.2.2 Preconditioning

Time derivative preconditioning [78] is used for the proper conditioning of A_Γ. ρ_p in the Γ matrix is modified as $\rho_p^{'}$ to construct the preconditioned time derivative matrix

Γ_p as:

$$\Gamma_p = \begin{pmatrix} \rho_{p'} & 0 & 0 & 0 & \rho_{Y_v} \\ u\rho_{p'} & \rho & 0 & 0 & u\rho_{Y_v} \\ v\rho_{p'} & 0 & \rho & 0 & v\rho_{Y_v} \\ w\rho_{p'} & 0 & 0 & \rho & w\rho_{Y_v} \\ Y_v\rho_{p'} & 0 & 0 & 0 & Y_v\rho_{Y_v} + \rho \end{pmatrix}. \tag{6.3}$$

Note that the rest of the elements of the Γ_p matrix are the same as Γ. Here, $\rho_p^{'} = \frac{1}{U_\infty^2}$ [77]. Note that for $\rho_p^{'}$ various other preconditioners can be used (e.g. [13, 82]). This can be easily adopted in the current solver. The eigenvalues of the preconditioned system can be obtained from the matrix $A_{p\Gamma} = \Gamma_p^{-1}A$. The matrices Γ_p^{-1} and $A_{p\Gamma}$ are given in A.2. The eigenvalues of $A_{p\Gamma}$ are $\lambda_{p\Gamma} = [V_n, V_n, V_n, \frac{1}{2}(V_n(1+\frac{c^{'2}}{c^2}) - \sqrt{V_n^2(1-\frac{c^{'2}}{c^2})^2 + 4c^{'2}}), \frac{1}{2}(V_n(1+\frac{c^{'2}}{c^2}) + \sqrt{V_n^2(1-\frac{c^{'2}}{c^2})^2 + 4c^{'2}})]$, where c' is the modified speed of sound based on $\rho_p^{'} = \frac{1}{c^{'2}}$. Note that all the eigenvalues are of the order V_n; when $c^{'2} = 1/\rho_p^{'} = U_\infty^2$ is used for the preconditioning. Hence, the matrix $A_{p\Gamma}$ is well conditioned. Note that the pseudo-time derivative vanishes as one marches to the next time step in the physical-time. Hence, time accuracy is preserved when solving unsteady problems.

6.2.3 Time marching with *DTS*

The governing equation (eq.6.2) after finite-volume integration and simplifications is given as,

$$\Gamma_p \frac{\partial Q}{\partial \tau} + \frac{\partial U}{\partial t} = R(U) \quad \text{where} \quad R(U) = -\frac{1}{\mathcal{V}} \int_{\mathcal{S}} F_j n_j d\mathcal{S} + \frac{1}{\mathcal{V}} \int_{\mathcal{V}} S d\mathcal{V}. \tag{6.4}$$

Here, $\mathcal{V}$ is the volume and S is the surface area of the cell. The time marching is performed using a *DTS* procedure (e.g. [75, 76]), where the physical-time derivative is discretized using a second order backward differencing (*BDF-2*) and the pseudo-time derivative is discretized using an explicit Euler. Alternatively, a fourth order Runge-Kutta (*RK-4*) method is considered for discretizing the pseudo-time derivative. However, overall cost of computing 4 stages of *RK-4* outweighed the CFL gain compared to the single step of the explicit Euler. Also, the explicit Euler is chosen for the simplicity

of the preconditioned DTS framework. Indicating the current physical-time with 'n' and the pseudo-time with 'm', the discretized form of the equation is given as:

$$\Gamma_p \frac{Q^{m+1} - Q^m}{\Delta\tau} + \frac{3U^{n+1} - 4U^n + U^{n-1}}{2\Delta t} = R(U^m). \tag{6.5}$$

Here, U^{n+1} is unknown. It can be treated implicitely with respect to the pseudo-time by considering it at $m+1$. Following the linearization $U^{m+1} = U^m + \Delta\tau\Gamma\frac{\Delta Q}{\Delta\tau}$, equation 6.6 can be written as:

$$\begin{aligned} \left(\Gamma_p + \frac{3\Delta\tau}{2\Delta t}\Gamma\right)\frac{\Delta Q}{\Delta\tau} &= R1(U^m), \quad where \\ R1(U^m) &= -\left(\frac{3U^m - 4U^n + U^{n-1}}{2\Delta t}\right) + R(U^m). \end{aligned} \tag{6.6}$$

Here, $\Delta Q = Q^{m+1} - Q^m$. The matrices on the left-hand side can be combined as $\Gamma_{ip} = \Gamma_p + \frac{3\Delta\tau}{2\Delta t}\Gamma$. The pseudo-time marching is performed by inverting the matrix Γ_{ip}. Γ_{ip}^{-1} is given in the A.2. After the pseudo-time iterations are converged, the primitive variables are updated as $Q^{n+1} = Q^{m+1}$. Subsequently, the conserved variables are obtained from the primitive variables.

6.2.4 Shock capturing

Guillard and Viozat [80] showed that the preconditioning of the numerical dissipation term is necessary for the accurate scaling of the pressure fluctuations of the discrete system. They performed the asymptotic analysis of the compressible Euler equation discretized using Roe's dissipation scheme, and proposed preconditioning of the numerical dissipation tensor to recover the correct scaling of the pressure. Turkel [78] discusses various preconditioners for artificial dissipation terms. Turkel [78] shows that different choices for variables and preconditioners can be used in the time derivative matrix and the artificial dissipation term. Also, it is suggested that if one wishes to capture shocks, the fluxes are evaluated in terms of conserved variables (U) and subsequently preconditioned. Hence, for shock capturing the conservative variables are retained.

The convective fluxes can be computed as the sum of the central part and the

dissipation part as:

$$F^c = F^c_c + F^c_d. \tag{6.7}$$

Here, F^c_c is the central part, which is discretized using a symmetric non-dissipative finite volume scheme, where fluxes at a cell face are given by

$$\phi_{f_c} = \frac{\phi_{icv1} + \phi_{icv2}}{2} + \frac{1}{2}(\nabla\phi|_{icv1} \cdot \Delta\mathbf{x}^{icv1} + \nabla\phi|_{icv2} \cdot \Delta\mathbf{x}^{icv2}), \tag{6.8}$$

where $\Delta\mathbf{x}^{icv1} = \mathbf{x}_{f_c} - \mathbf{x}_{icv1}$, and $\nabla\phi|_{icv1}$ denotes gradient defined at $icv1$, which is computed using a least-squares method. '$icv1$' is the current cell, '$icv2$' is the neighbouring cell, and 'fc' is the common face. The viscous fluxes are split into the compressible and the incompressible contributions, and treated separately. See [43] for the details.

F^c_d is the dissipation part, which is treated using the characteristic based filtering [48]. Originally, the method was developed by Yee et al. [48] for ideal gases on structured grid. Park and Mahesh [47] extended this to unstructured grids. Gnanaskandan and Mahesh [43] extended this to the mixture of fluids and the mixture equation of state used in the present work. They implemented the methodology in a predictor-corrector manner, where the filtering is applied in the corrector step as discussed in chapter 2. Alternatively, the filtering can also be directly applied for the dissipative part of the flux in a single step as discussed in Yee et al. [48]. In the present work, we compute both the central part and the dissipation part in a single step as shown in the equation 6.7. It is done for the simplicity in adopting the fluxes in a DTS framework. The formulation for the characteristic filtering is the same as used in Gnanaskandan and Mahesh [43]. However, the eigenvalues are modified to obtain the proper conditioning at the low Mach. F^c_d in the characteristic filtering is of the following form:

$$F^c_{d\,f_c} = \frac{1}{2} R_{f_c} \Phi_{fc}. \tag{6.9}$$

Here, R_{f_c} is the matrix of right eigenvectors of the jacobian $B = \frac{\partial F}{\partial U}$. It is computed at the face using the Roe average of the variables from the left and the right cell-centered values. The matrices R, R^{-1} and B are given in the Appendix of [84]. Φ^*_{fc} is a vector,

l-th component of which, ϕ^{*l}, is given by

$$\phi^{*l}_{fc} = k\theta^{l}_{fc}\phi^{l}_{fc}, \tag{6.10}$$

where k is an adjustable parameter and θ_{fc} is Harten's switch function, given by

$$\theta_{fc} = \sqrt{0.5(\hat{\theta^2_{icv1}} + \hat{\theta^2_{icv2}})}, \quad \hat{\theta_{icv1}} = \frac{|\beta_{fc}| - |\beta_{f1}|}{|\beta_{fc}| + |\beta_{f1}|}, \quad \hat{\theta_{icv2}} = \frac{|\beta_{f2}| - |\beta_{fc}|}{|\beta_{f2}| + |\beta_{fc}|}. \tag{6.11}$$

Here, $\beta_f = R_f^{-1}(U_{icv2} - U_{icv1})$ is the difference between characteristic variables across the face. q For ϕ_l, Harten-Yee total variation diminishing (TVD) form is used as suggested by Yee et al. [48]:

$$\begin{aligned} \phi^{l}_{fc} &= \frac{1}{2}\Psi(a^{l}_{fc})(g^{l}_{icv1} + g^{l}_{icv2}) - \Psi(a^{l}_{fc} + \gamma^{l}_{fc})\beta^{l}_{fc}, \\ \gamma^{l}_{fc} &= \frac{1}{2}\frac{\Psi(a^{l}_{fc})(g^{l}_{icv2} - g^{l}_{icv1})\beta^{l}_{fc}}{(\beta^{l}_{fc})^2 + \epsilon}, \end{aligned} \tag{6.12}$$

where $\epsilon = 10^{-7}$, $\Psi(z) = \sqrt{\delta + z^2}$ (δ being 1/16) is introduced for entropy fixing and a^{l}_{fc} is an eigenvalue of the jacobian matrix B.

B has the set of eigenvalues $\lambda_B = [V_n, V_n, V_n, V_n - c, V_n + c]$. Note that the matrix is ill-conditioned in the low Mach limit. One way to rectify this is to use a typical low-speed preconditioner (e.g. [81]). This works well in the incompressible limit. However, for cavitating flows Mach numbers can range from the extremely low values in the water to the supersonic regions in the mixture. Hence, in the present work, we use an all-mach preconditioning approach proposed by Li and Gu [74]. Interestingly, the implementation of this approach is straight-forward as it only involves changes in the eigenvalues of B, keeping both the jacobian matrix and the eigenvector matrix the same. Li and Gu [74] discusses this in detail. Following that, we modify the eigenvalues as:

$$\begin{aligned} \lambda_B &= [V_n, V_n, V_n, V_n - f(M)c, V_n + f(M)c], \quad \text{where} \\ f(M) &= min(M^2, 1). \end{aligned} \tag{6.13}$$

Here, $f(M)$ is a function of local Mach number that satisfies the following three criteria:

$$\begin{aligned} &0 < f(M) < 1 \quad \text{when} \quad 0 < M < 1 \\ &f(M) \rightarrow\ 0 \quad \text{when} \quad M \rightarrow\ 0 \\ &f(M) = 0 \quad \text{when} \quad M >= 1 \end{aligned}$$

The limiter function g_{icv} is computed using the minmod limiter. Park and Mahesh [47] and Gnanaskandan and Mahesh [43] proposed a modification to the Harten's switch to accurately represent under-resolved turbulence for single phase and multi phase flow mixtures respectively by multiplying θ_{f_c} with $\theta^{\star}_{f_c}$ given by

$$\begin{aligned} \theta^{\star}_{f_c} &= \frac{1}{2}\left(\theta^{\star}_{icv1} + \theta^{\star}_{icv2}\right) + |(\alpha_{\text{icv2}} - \alpha_{\text{icv1}})|, \\ \theta^{\star}_{icv1} &= \frac{(\nabla \cdot \mathbf{u})^2_{icv1}}{(\nabla \cdot \mathbf{u})^2_{icv1} + \Omega^2_{icv1} + \epsilon}. \end{aligned} \tag{6.14}$$

6.3 Results

We assess the methodology using the following numerical experiments. First, we consider the unsteady flow over a cylinder under wetted conditions. The problem is used to assess the preconditioning and *DTS* framework for the unsteady low Mach number problem in the water. Various aspects of the simulation such as the total run-time, shedding frequency, pressure, and the velocity field are considered for comparison and analysis. Next, the background pressure is dropped to examine cavitation inception in the cylinder configuration. Here, the method is assessed to handle the small scale vapor regions at the low free-stream nuclei concentration (consequently at low Mach). Finally, the ability of the method to extend to the complex problems is assessed by doing the LES of high Re flow over a marine propeller under wetted conditions.

6.3.1 Unsteady flow over a cylinder

Cases simulated	(α_{v_∞})	M_∞	Description
Case-O	10^{-2}	0.01	Original solver - no preconditioning [43]
Case-OLM	10^{-6}	0.001	Original solver at low Mach
Case-P	10^{-2}	0.01	Preconditioning with DTS
Case-PLM	10^{-6}	0.001	Preconditioning with DTS at low Mach
Case-PRLM	10^{-6}	0.001	Preconditioning with DTS with RS at low Mach

Table 6.1: Details of the simulations conducted for the flow over a cylinder at Re=200. Here, α_{v_∞} is the free-stream nuclei content, and M_∞ is the free-stream Mach number.

We simulate the flow over a circular cylinder at Reynolds number (Re) $= \frac{\rho_\infty U_\infty D}{\mu_\infty} = 200$, where the subscript '$\infty$' represents the free-stream values and D is the cylinder diameter. The domain size and the mesh used in the present study are the same as those considered in Brandao et al. [39] and Gnanaskandan and Mahesh [37]. Gnanaskandan and Mahesh [37] performed a grid refinement study and showed that the time evolution of the drag coefficient and the profiles of the mean and the fluctuations in the void fraction show a good agreement among the chosen grids. To avoid the reflection of pressure waves from the boundaries, a large domain of $50D$ is used. Also, we apply acoustically absorbing sponge layers at the boundaries [70] to further reduce any reflections. The simulations are initialized with a spatially uniform void fraction of vapor (α_{v_∞}) as a background nuclei. The flow Mach number is changed by choosing different values of free-stream nuclei. Table 6.1 summarizes the simulated cases. All the cases are simulated at a cavitation number $(\sigma) = \frac{p-p_v}{0.5\rho_\infty U_\infty^2} = 5$, such that no cavitation is observed. Only the free-stream nuclei are varied that change the free-stream Mach number, and consequently the acoustic stiffness. The changes in Mach number are within the incompressible limit, thus, the unsteady vortex shedding is expected to be identical.

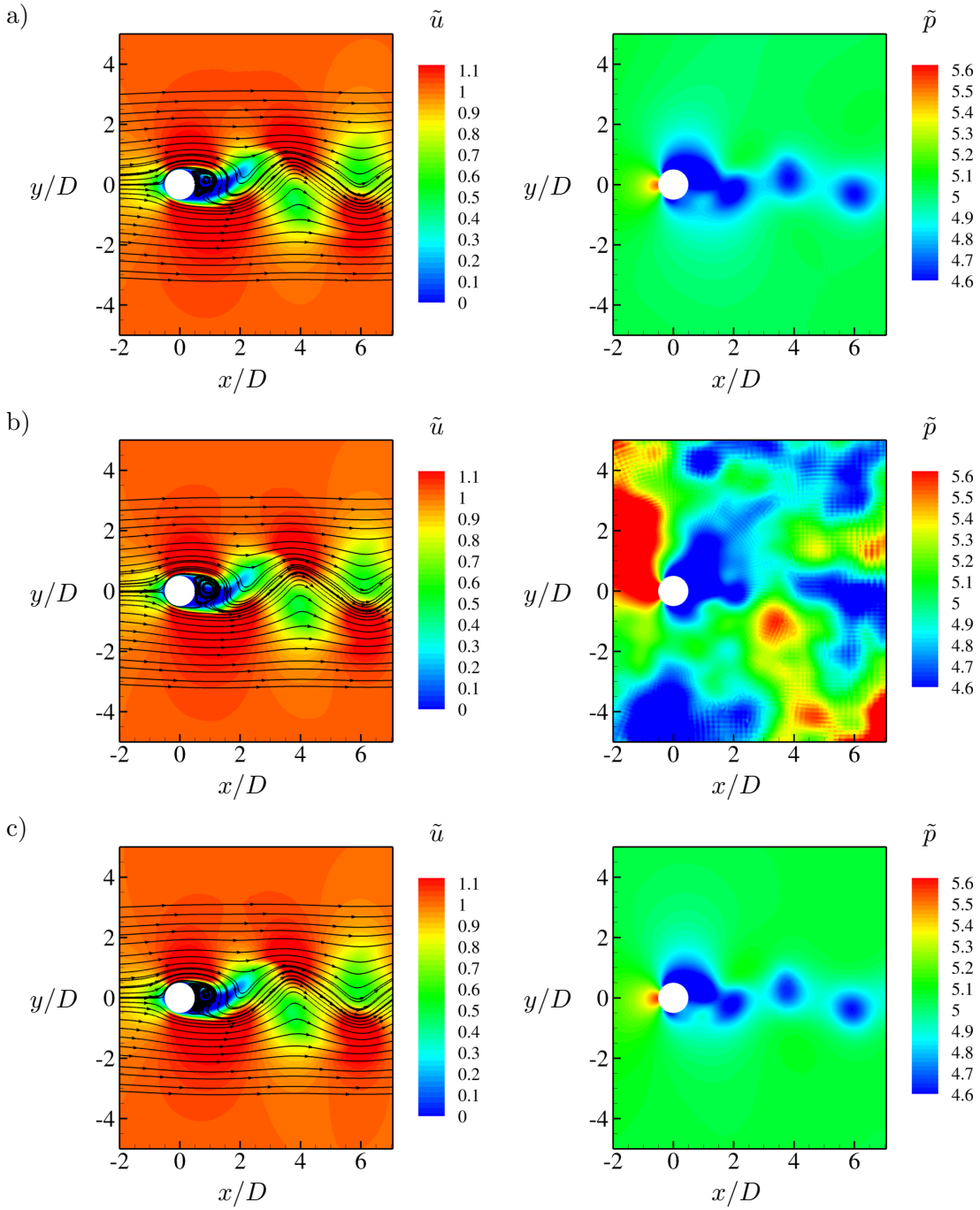

Figure 6.1: Unsteady flow over a cylinder at Re=200. a) Case-O, b) Case-OLM, and c) Case-PLM. Instantaneous snapshots of $\tilde{u}$ (on the left), and $\tilde{p}$ (on the right).

Figure 6.1 shows the instantaneous snapshots of $\tilde{u}$ and $\tilde{p}$ for 3 cases: (i) original solver of Gnanaskandan and Mahesh [43] at high Mach number (Case-O), (ii) original solver at low Mach number (Case-OLM) and (iii) preconditioning with dual time stepping at low Mach number (Case-PLM); respectively in the figures 6.1(a), 6.1(b) and 6.1(c). Here, $\tilde{u} = u/U_\infty$ is the non-dimensional axial component of the velocity, and $\tilde{p} = \frac{p}{\rho_\infty U_\infty^2}$ is the non-dimensional pressure. For the Case-O, the sinusoidal velocity field and the pockets of low-pressure cores of the vortices indicate that the compressible solver is reasonably capturing the vortex shedding at this Mach number. However, at low Mach, for Case-OLM, the pressure field is completely intangible. This is due to the incorrect scaling of the pressure field for the compressible solver in the incompressible limit [78]. Interestingly, the Case-PLM shows that with the use of preconditioning, the accurate pressure field is retained even at low Mach number (Case-PLM).

We consider Case-O as the baseline to compare the Case-PLM. The profiles of the mean pressure and the root-mean-squared (RMS) pressure are chosen for the comparison and shown in the figures 6.2 and 6.3 respectively. A very good agreement is observed in both the mean pressure and the RMS pressure to the Case-O. This demonstrates the ability of the methodology with preconditioning to capture the accurate pressure field at low Mach.

The Strouhal number for the vortex shedding is obtained as $St = \frac{fD}{U_\infty}$. Here, 'f' is the vortex shedding frequency obtained from the Fast Fourier Transform (FFT) of the time-history of the drag coefficient. It is compared to the canonical study of Williamson [85] in the table 6.2. Note the good agreement with the Williamson [85] for both the Case-O and Case-PLM. Interestingly, the Case-PLM shows a better comparison to Williamson [85] than Case-O. The identical values the St for both Case-P and Case-PLM indicates that the St is not affected by the flow Mach number when the preconditioning is used.

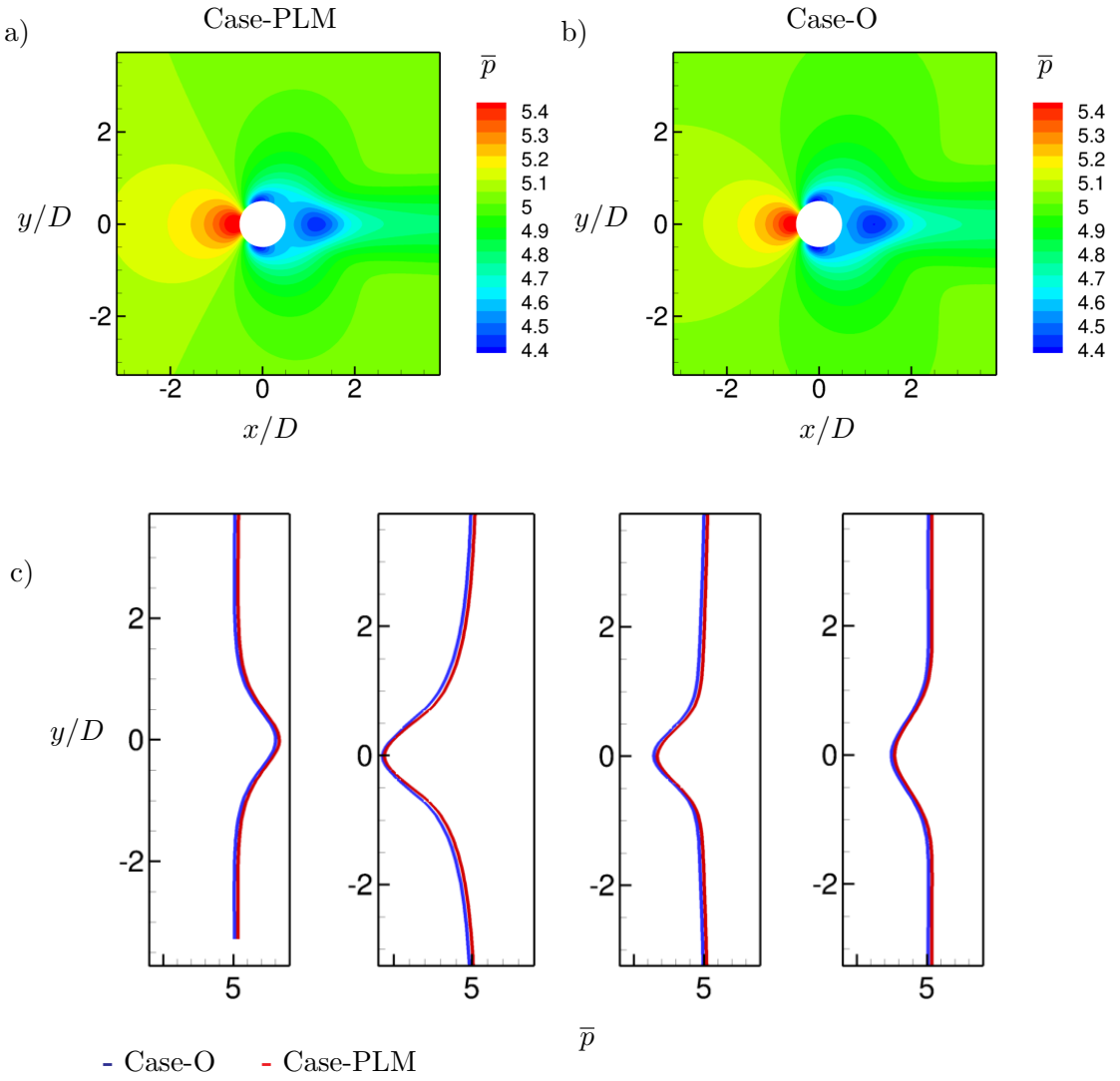

Figure 6.2: Comparison of the mean pressure profiles ($\overline{p}$) for the unsteady flow over a cylinder at Re=200. a) Contours of $\overline{p}$ for Case-PLM, and b) Case-O. c) Profiles extracted along the $y-axis$ at $x/D = -1.0$, 1.0, 2.0 and 3.0.

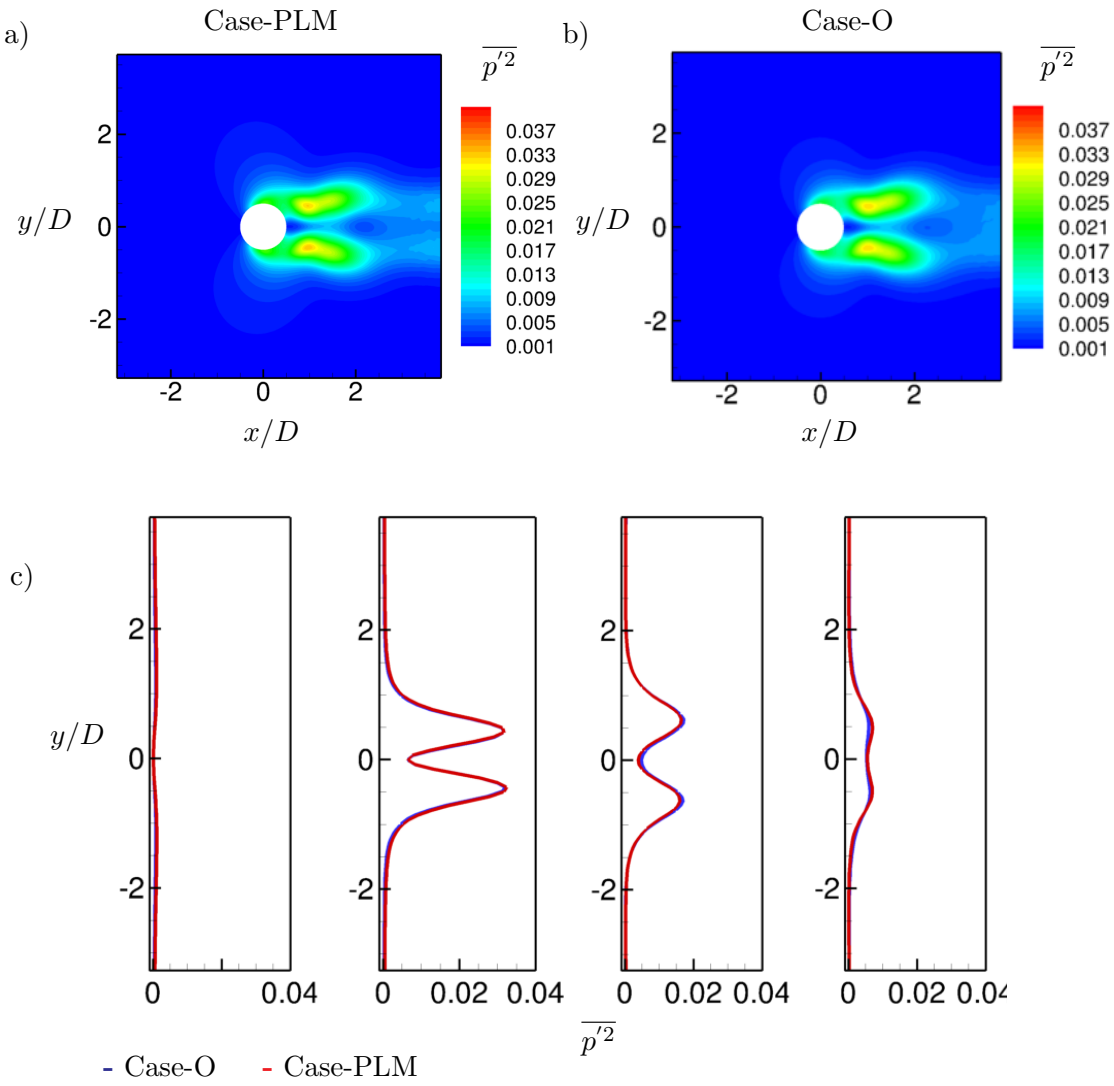

Figure 6.3: Comparison of the *RMS* pressure profiles ($\overline{p'^2}$) for the unsteady flow over a cylinder at Re=200. a) Contours of $\overline{p'^2}$ for Case-PLM, and b) Case-O. c) Profiles extracted along the $y-axis$ at $x/D = -1.0$, 1.0, 2.0 and 3.0.

	Case-O	Case-OLM	Case-P	Case-PLM	[85]
$St = fD/U_\infty$	0.198	$\times$	0.184	0.184	0.182

Table 6.2: Comparison of the St for the flow over a cylinder at Re=200. St is computed from the frequency obtained from the Fast Fourier Transform (FFT) of the time-history of the drag coefficient.

In addition to improving the solution accuracy, preconditioning significantly reduces computer time. The table 6.3 compares the computer time for all the cases simulated. At low Mach number, the time step for the compressible solver drops by a factor of 50 from 5×10^{-5} to 1×10^{-6}. This increases the total run-time from 33.5 min to 1 day for 1 cycle of vortex shedding. Therefore, we can see that the acoustic stiffness due to disparities in eigenvalues at low Mach significantly affects the run-time. The acoustic stiffness is eliminated with the use of preconditioning as observed in table 6.3 for Case-P, Case-PLM, and Case-PRLM. A significantly high physical-time step of 1×10^{-2} can be used with the preconditioning. Also, the physical-time step is independent of the Mach number. The calculations can be further accelerated by using the residual smoothing (RS) (e.g. [75]) for the convergence of the pseudo-time step. The RS increases pseudo-time step by a factor of 3 from 2×10^{-3} to 6×10^{-3} and reduces the total run-time by half.

Cases simulated	Δt	$\Delta \tau$	run-time/cycle	n_{itr}
Case-O	5×10^{-5}	–	33.5 min	–
Case-OLM	1×10^{-6}	–	1 day	–
Case-P	1×10^{-2}	2×10^{-3}	6.18 min	30
Case-PLM	1×10^{-2}	2×10^{-3}	5.6 min	30
Case-PRLM	1×10^{-2}	6×10^{-3}	3.7 min	11

Table 6.3: Computational time for the cases simulated for the flow over a cylinder at Re=200. Here, Δt is the physical-time step, $\Delta \tau$ is the pseudo-time step, and n_{itr} is the number of pseudo-time iterations per physical-time step.

6.3.2 Cavitation inception over a cylinder

In this section, we consider the flow at $\sigma = 1.8$. The only difference from the calculations presented in section 6.3.1 is that the free-stream pressure is dropped to allow cavitation; thereby, changing σ from 5 to 1.8. For the σ lower than 1.8, Brandao et al. [39] discuss the developed cavitation regimes in detail. They show that at $\sigma = 1$, cavitation is observed in the vortex core as the local pressure inside the core drops below vapor pressure, this is termed as the cyclic regime. If σ is further reduced to 0.7, the pressure in the near wake of the cylinder also drops below vapor pressure. This leads to transitional shedding by condensation shock propagation. Given this prior work, the current development allows us to extend to higher σ close to cavitation inception, with significant time savings. The details of the flow conditions and the computer time requirements are given in table 6.4. Note that changing the cavitation number does not affect the time step and the overall run-time when preconditioning is used (compare the case in table 6.4 to the cases in table 6.3). A significant saving in the run-time over the original solver (compare Case-OLM with Case-I) is obtained at low Mach.

Case simulated	(α_{v_∞})	M_∞	σ	Description
Case-I	10^{-6}	0.001	1.8	Preconditioning, *DTS*, *RS* at low Mach
	Δt	$\Delta\tau$		run-time/cycle
	1×10^{-2}	2×10^{-3}		4.17 *min*

Table 6.4: Details of the simulations conducted for the cavitation inception over a cylinder including the computer time requirements. Here, α_{v_∞} is the free-stream nuclei content, M_∞ is the free-stream Mach number, Δt is the physical-time step, and $\Delta\tau$ is the pseudo-time step.

The solution is visualized by the instantaneous snapshots of Y_v and $\tilde{p}$. Three snapshots are chosen to cover a single vortex shedding cycle from the bottom of the cylinder. $\tilde{p}$ is plotted on a log scale from 0.01 to 1. The corresponding non-dimensional value of the vapor pressure is 0.011. Hence, the blue regions observed at the bottom of the

cylinder surface in figure 6.4(a) indicate the local pressure lower than the vapor pressure. Unlike the cyclic cavitation regime discussed by Brandao et al. [39] at $\sigma = 1$; here at $\sigma = 1.8$, the regions within the vortex core show the local pressure higher than the vapor pressure. This suggests that the vapor is incepted on the cylinder surface and advected downstream along the shear-layer into the vortex core. In the subsequent snapshots, after the vortex is shed from the bottom, the low pressure now appears on the top of the cylinder (figure 6.4) continuing the periodic shedding. The St remains unchanged from the non-cavitation conditions as shown in table 6.2. Overall, the Y_v remains of the $O(10^{-7})$, which is 3 orders of magnitude lower than what was observed in the developed cavitation regimes [39].

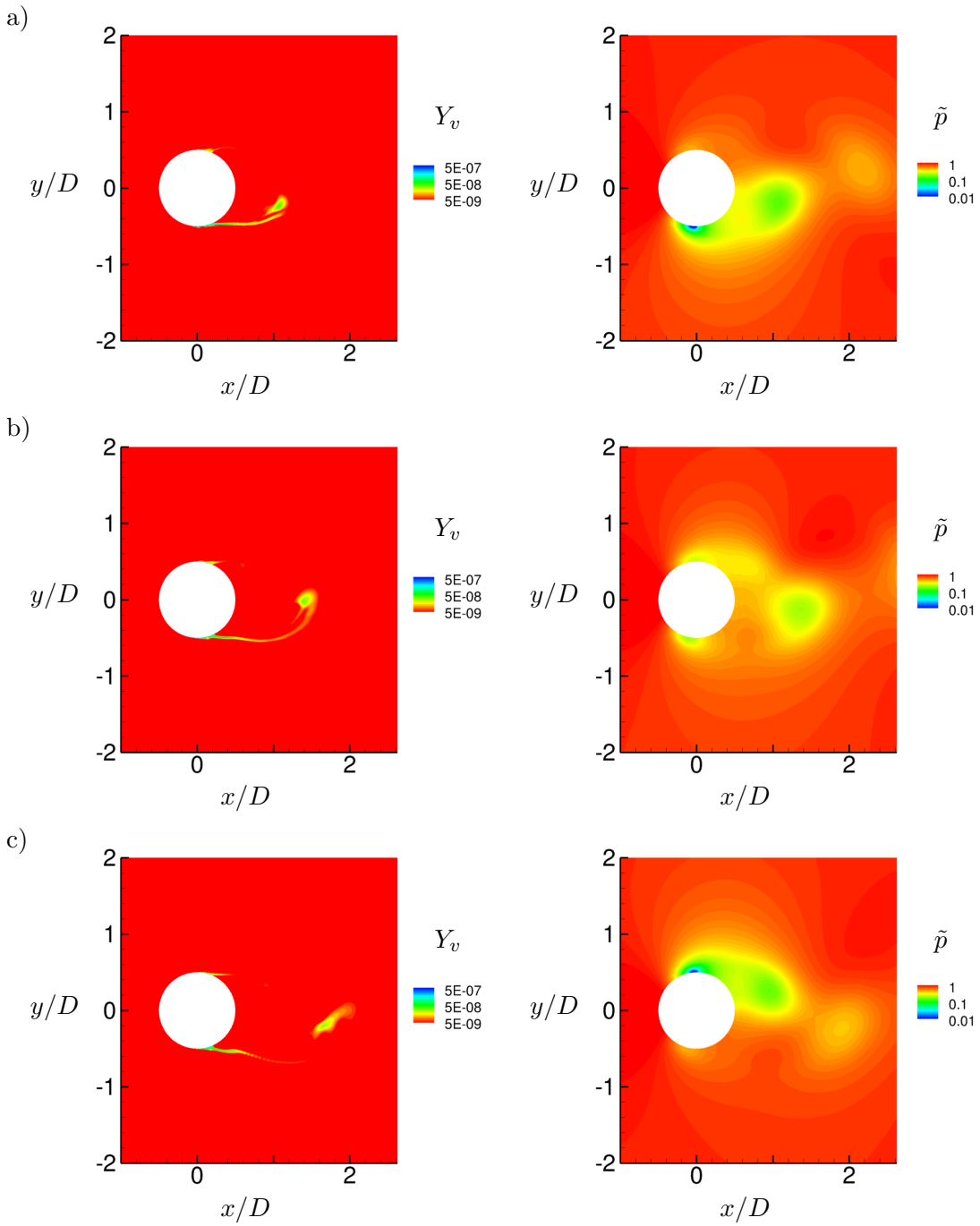

Figure 6.4: Cavitation inception on the cylinder at Re=200 and $\sigma = 1.8$. a) Beginning of the vortex shedding, b) $t = 0.42$ *cycle* and c) $t = 0.84$ *cycle*. Instantaneous snapshots of Y_v (on the left), and $\tilde{p}$ (on the right).

6.3.3 LES of high Re flow over a marine propeller

As discussed in chapter 5, propeller loads are sensitive to the amount of free-stream nuclei. The lowest value of $\alpha_\infty = 1 \times 10^{-4}$ showed the closest comparison. However, a further reduction in the nuclei concentration could not be achieved with the original solver as it significantly reduced the time step and increased the total run-time. Here, with the preconditioning and *DTS*, we show that the calculations can be performed at such low free-stream nuclei in a reasonable amount of time. In the simulations, we discuss run-time, the effect of free-stream nuclei on the propeller loads, and comparison to both the experiments and the incompressible solver results. Table 6.5 summarizes the flow conditions, nomenclature, and the description of the cases considered for the comparison and analysis in this section.

Cases simulated	(α_{v_∞})	M_∞	Description
Case-O	10^{-2}	0.03	Original solver - no preconditioning [43]
Case-OLM	10^{-4}	0.005	Original solver at low Mach
Case-PRLM	10^{-6}	0.002	Preconditioning with *DTS* with *RS* at low Mach

Table 6.5: Details of the simulations conducted for the LES of high Re flow over a propeller under wetted conditions. Here, α_{v_∞} is the free-stream nuclei content, and M_∞ is the free-stream Mach number.

First, we compare the propeller loads obtained from using the preconditioning to that of the original solver and the experimental data of [67] in the table 6.6. As discussed in the previous section a better comparison to the experiments can be obtained at lower values of free-stream nuclei. This is evident from comparing K_T and K_Q for Case-O and Case-OLM to [67] experiments. Case-OLM shows a better comparison to the experiments. The preconditioning allowed the calculations at an even lower nuclei concentration (Case-PRLM) (consequently, at a very low Mach). The preconditioning case shows a significant improvement in the K_Q from the prior study. Overall, both the K_T and K_Q of the Case-PRLM show a very good comparison to the experiments.

	K_T	K_Q
Case-O	0.257	0.055
Case-OLM	0.226	0.050
Case-PRLM	0.227	0.0458
Boswell [67]	0.215	0.045

Table 6.6: Comparison of propeller performance under the wetted conditions.

As discussed in section 6.3.1, for low Mach number flows it is important to assess the pressure field obtained from the compressible solver. Hence, we compare the mean and the *RMS* pressure field of the original solver (Case-OLM) and the preconditioned solver (Case-PRLM) with the incompressible MPCUGLES [71]. The incompressible solver is considered as the baseline since the M_∞ is less than 0.01. The contours of the mean pressure field are visualized in figure 6.5. For the Case-OLM the horizontal stripes upstream of the propeller, the lack of visibility of the tip vortices, and the diffused regions of low pressure close to the shaft are all indicators of the deteriorated pressure field. This behavior is similar to what was observed for the cylinder case in section 6.3.1. As noted earlier, it is due to the incorrect scaling of the pressure field for the compressible solver in the incompressible limit [78]. With the use of preconditioning (Case-PRLM), the improvement on all the fronts is observed. This is evident visually from the comparison of the Case-PRLM to the incompressible MPCUGLES. The secondary vortices close to the shaft of the propeller are better captured in the Case-PRLM. A quantitative comparison of the mean pressure is obtained by taking profiles along the $y - axis$ at various axial locations as indicated by the white dashed lines in figure 6.5(a).

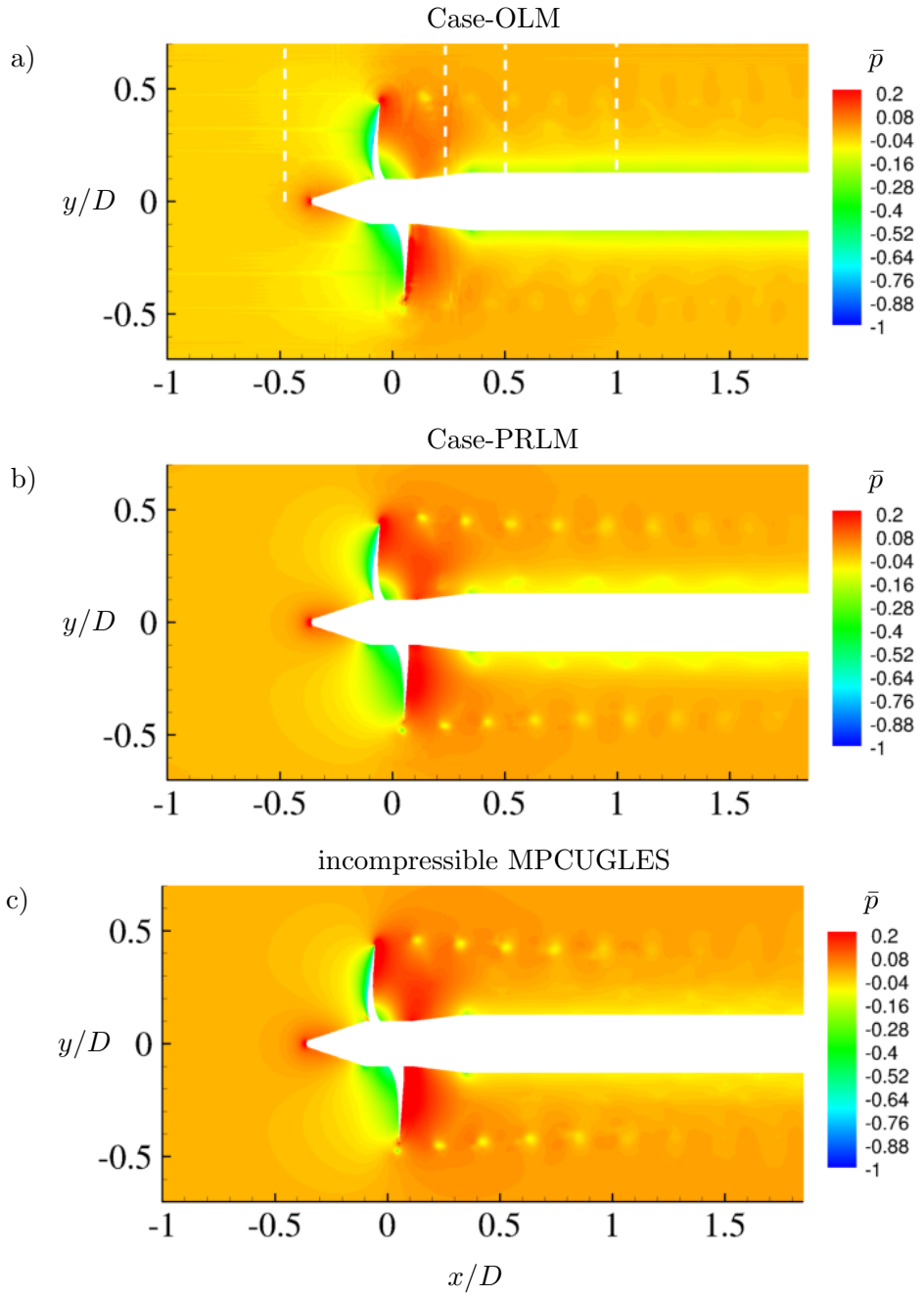

Figure 6.5: Contours of the phase averaged pressure field along the $x-y$ plane for $Re = 894000$ flow over the P4381 propeller under the wetted conditions. a) Case-OLM, b) Case-PLM and c) incompressible MPCUGLES [71]. The flow is from left to right.

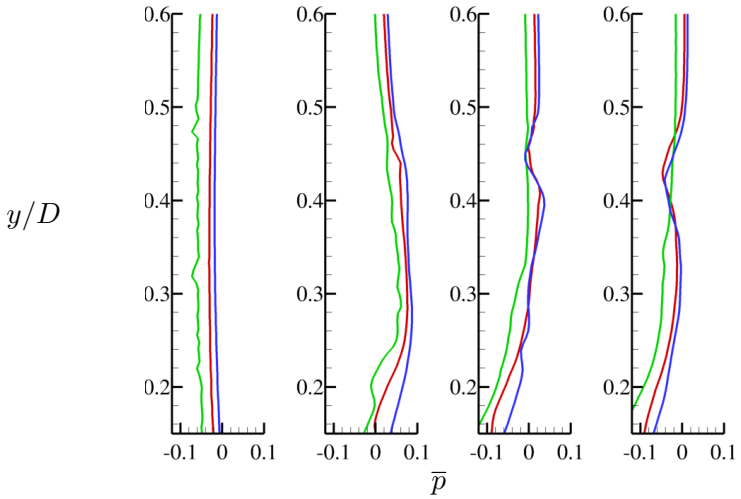

Figure 6.6: Profiles of the phase averaged pressure field for the $Re = 894000$ flow over the propeller P4381 under the wetted conditions. The profiles are extracted along the $y - axis$ at $x = -0.5D$, $0.25D$, $0.5D$ and $1.0D$.

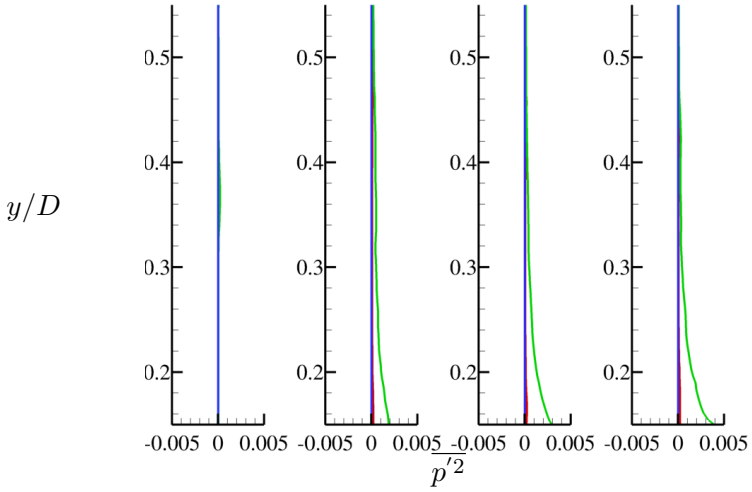

Figure 6.7: Profiles of the RMS pressure fluctuations for the $Re = 894000$ flow over the propeller P4381 under the wetted conditions. The profiles are extracted along the $y - axis$ at $x = -0.5D$, $0.25D$, $0.5D$ and $1.0D$.

The profiles are compared in figure 6.6. For Case-OLM, even the mean pressure upstream of the propeller at $x = -0.5D$ is different from the baseline incompressible MPCUGLES. Also, the profile shows oscillations along the $y - axis$. Both Case-PRLM and incompressible MPCUGLES are generally in good agreement at all the locations. The lower pressures near the shaft at $x = 0.25D$ and $x = 0.5D$ for the Case-PRLM are due to the secondary vortices near the shaft as visualized in the figure 6.5(b). The RMS pressure is compared in the figure 6.7. The pressure fluctuations are typically very small for the low Mach number flow. However, the Case-OLM shows very high-pressure fluctuations close to the shaft; particularly at the locations downstream of the propeller blade (i.e. $x = 0.25D$, $x = 0.5D$ and $x = D$). Here also, the Case-PRLM is generally in good agreement with the incompressible solution.

Finally, we compare the computational time savings when using preconditioning as compared to the original solver in the table 6.7. The preconditioning allows a significantly higher physical-time step of 5×10^{-3} as compared to the physical-time step of 2×10^{-6} of the original solver. Although, the overall gain in the run-time is not directly proportional to the time step gain as the additional time is needed to converge the pseudo-time derivative at each physical-time step. Nevertheless, preconditioning saves the run-time significantly from ~ 2 $weeks$ to ~ 40 $hours$ per cycle.

Cases simulated	Δt	$\Delta \tau$	run-time/cycle
Case-OLM	2×10^{-6}	–	~ 2 $weeks$
Case-PRLM	5×10^{-3}	1×10^{-3}	~ 40 $hours$

Table 6.7: Computational time for the cases simulated for the flow over propeller p4381 under the wetted conditions at $Re = 894000$. Here, Δt is the physical-time step, and $\Delta \tau$ is the pseudo-time step.

Chapter 7

Summary

The objective of this dissertation is to develop LES capabilities to study cavitation in complex hydrodynamic geometries. A fully-compressible homogeneous mixture model with finite rate mass transfer is used for the simulations. The homogeneous mixture model is evaluated using a bubble collapse problem. It is observed that as long as the vapor region is sufficiently resolved, the homogeneous models are accurate in predicting the dynamics of small vapor regions, making them a suitable approach to study sheet to cloud cavitation transition. The results from the homogeneous mixture model and the Rayleigh-Plesset equation are compared for a range of bubble sizes, smaller length scales showing the dominant effect of surface tension forces. The effect of considering $2D$ collapse as is commonly assumed in RANS is illustrated by comparing cylindrical and spherical bubble collapse. It is shown that the cylindrical bubble collapse produces much smaller collapse pressure than a spherical bubble collapse. The evaporation/condensation source terms are composed in terms of the non-dimensional parameters that determine the relative strength of flow advection with respect to the phase change. The expression for the finite rate mixture speed of sound is derived using the rates from Saito et al. [16] cavitation model.

The methodology is used to investigate partial cavitation over incipient, transitory and periodic regimes matching the experimental sharp wedge configuration of Ganesh et al. [1]. Instability mechanisms of the sheet to cloud transition, both the re-entrant

jet and the bubbly shock wave, are captured in the LES. In the developed cavitation regimes, large regions of vapor in the sheet/cloud and the resulting volume fraction field are accurately captured in the current simulations. Besides, the instantaneous evolution of the void fraction field, bubbly shock propagation speed, and shedding frequency show very good comparison to the experiments. Conditions favoring the formation of either the re-entrant jet or the bubbly shock wave are analyzed using LES. In the transitory regime, larger streamline curvature leads to a higher adverse pressure gradient. This is observed both normal to the cavity and along the axial direction at the cavity closure. A higher adverse pressure gradient supports flow reversal and formation of the re-entrant jet. The streamline curvature reduces with the growing cavity moving from the transitory to the periodic regime. Reduction in the streamline curvature leads to smaller pressure recovery from within the cavity to outside. Hence, overall low pressures in the cavity closure lead to the reduced speed of sound and increased medium compressibility. This favors the formation of shock waves in the periodic regime. In the periodic regime, bubbly shock waves are initiated by the collapse-induced pressure waves of the previously shed cloud. The process is illustrated using instantaneous plots and $s-t$ diagrams. The collapse-induced pressure wave travels through a highly compressible low volume fraction bubbly mixture. It subsequently impinges on the trailing edge of the cavity initiating the cavity retraction by a bubbly shock wave. Properties across collapse-induced pressure wave and the bubbly shock wave are analyzed using Rankine-Hugoniot jump conditions. Supersonic Mach numbers, significant condensation, and smaller pressure rise are observed across the bubbly shock wave in accordance with the prior studies. Jumps in the vapor mass and density across the collapse-induced pressure waves are small. Interestingly, the regions within the cavity are subsonic despite the low speed of sound due to extremely small velocities inside the cavity. Reverse flow and supersonic Mach numbers are observed in the cavity closure region.

The flow over a five-bladed marine propeller (P4381) at the design advance ratio is investigated under the wetted and the thrust/torque breakdown conditions. The original methodology is extended to solve the governing equations in the rotating frame of reference. An important aspect of initializing the compressible flow solver is considered.

A divergence-free initial condition necessary to avoid transient pressure waves generated due to the sudden start of the propeller is provided using in-house incompressible flow solver MPCUGLES (Mahesh et al. [71]). Wetted flow conditions are simulated at Re=894,000 and J=0.89. The effect of shock-capturing is assessed by adjusting the corrector fluxes to the non-dissipative predictor step. No significant effect of numerical dissipation is observed on the propeller performance for the considered corrector fluxes. Propeller performance obtained using LES is shown to be independent of grids considered. It was interesting to note that under wetted conditions, flow showed sensitivity to the background nuclei content. A parametric study performed over a range of free-stream nuclei showed the closest comparison to the experiments for the lowest value of free stream nuclei considered.

Numerical approach based on preconditioning and dual-time stepping is developed to address the numerical stiffness in the cavitating flows at low Mach. The key aspects of the numerical approach are: (i) the preconditioning applied to the cavitating flow equations in a fully-compressible (density-based) solver, (ii) modifications based on the all-speed Roe-type scheme to the characteristic-based filtering, and (iii) the implementation in parallel and on the unstructured grids that allow the simulation of complex problems such as a propeller. The numerical formulation of the time-derivative preconditioning matrix, the DTS framework, and modification to the shock-capturing are discussed in detail. The numerical approach is assessed for wetted conditions and cavitation inception over the unsteady flow over a cylinder at $Re = 200$, and wetted conditions over a propeller at $Re = 89400$ using LES. Overall, a significant saving in the total run-time as compared to the original solver is obtained. The methodology enabled the use of low free stream nuclei calculations that resulted in accurate calculations of propeller loads. The accurate pressure field at a low Mach number is obtained that is in agreement with the incompressible solver.

Bibliography

[1] H. Ganesh, S. A. Makiharju, and S. L. Ceccio. Bubbly shock propagation as a mechanism for sheet-to-cloud transition of partial cavities. *Journal of Fluid Mechanics*, 802:37–78, 2016.

[2] C. J. Chesnakas and D. S. Jessup. Tip-vortex induced cavitation on a ducted propulsor. In *ASME/JSME 4th Joint Fluids Summer Engineering Conference*, 2003.

[3] H. J. Heinke. Potsdam propeller test case (PPTC)- cavitation test case 2.3. *Second International Sysmposium on Marine Propulsors*, 2011.

[4] G. H. G. Mitchell, R. Sampson, and M. Atlar. A modern approach to the representation and use of the kca systematic propeller series. *Third International Symposium on Marine Propulsors*, 2013.

[5] C. E. Brennen. Cavitation and bubble dynamics.

[6] N. A. Chang, J. Choi, R. Yakushuji, and S. L. Ceccio. Cavitation inception during the interaction of a pair of counter–rotating vortices. *Physics of Fluids*, 24:1–15, 2012.

[7] T. J. O'Hern. An experimental investigation of turbulent shear flow cavitation. *Journal of Fluid Mechanics*, 215:365–391, 1990.

[8] M. Callenaere, J-P. Franc, J. Michel, and M. Riondet. The cavitation instability

induced by the development of a re-entrant jet. *Journal of Fluid Mechanics*, 444: 223–256, 2001.

[9] URL http://www.legi.grenoble-inp.fr/people/Jean-Pierre.Franc/gallery.html.

[10] URL http://cav.safl.umn.edu/research-areas/ventilated-supercavitation.

[11] B. R. Shin, Y. Iwata, and T. Ikohagi. Numerical simulation of unsteady cavitating flows using a homogenous equilibrium model. *Computational Mechanics*, 30(5-6): 388–395, 2003.

[12] R. F. Kunz, D. A. Boger, D. R. Stinebring, T. S. Chyczewski, J. W. Lindau, H. J. Gibeling, S. Venkateswaran, and T. R. Govindan. A preconditioned Navier–Stokes method for two–phase flows with application to cavitation prediction. *Computers & Fluids*, 29(8):849–875, 2000.

[13] V. Ahuja, A. Hosangadi, and S. Arunajatesan. Simulations of cavitating flows using hybrid unstructured meshes. *Journal of Fluids Engineering*, 123(2):331–340, 2001.

[14] G. H. Schnerr, I. H. Sezal, and S. J. Schmidt. Numerical investigation of three–dimensional cloud cavitation with special emphasis on collapse induced shock dynamics. *Physics of Fluids*, 20(4):1–9, 2008.

[15] T. G. Liu, B. C. Khoo, and W. F. Xie. Isentropic one–fluid modeling of unsteady cavitating flow. *Journal of Computational Physics*, 201(1):80–108, 2004.

[16] Y. Saito, R. Takami, I. Nakamori, and T. Ikohagi. Numerical analysis of unsteady behavior of cloud cavitation around a NACA0015 foil. *Computational Mechanics*, 40(1):85–96, 2007.

[17] J. H. Seo and S. Lele. Numerical investigation of cloud cavitation and cavitation noise on a hydrofoil section. In *7th International Symposium on Cavitation*, number 0062, pages 1–15, 2009.

[18] J. H. Seo, Y. J. Moon, and B. R. Shin. Prediction of cavitating flow noise by direct numerical simulation. *Journal of Computational Physics*, 227(13):6511–6531, 2008.

[19] A. K. Singhal, M. M. Athavale, H. Li, and Y. Jiang. Mathematical basis and validation of the full cavitation model. *Journal of Fluids Engineering*, 124(3):617–624, 2002.

[20] I. Senocak and W. Shyy. A pressure–based method for turbulent cavitating flow computations. *Journal of Computational Physics*, 176(2):363–383, 2002.

[21] R. Saurel and O. Lemetayer. A multiphase model for compressible flows with interfaces, shocks, detonation waves and cavitation. *Journal of Fluid Mechanics*, 431(6):239–271, 2001.

[22] E. Goncalves and R-F. Patella. Numerical simulation of cavitating flows with homogeneous models. *Computers & Fluids*, 38(9):1682–1696, 2009.

[23] E. Goncalves and R. F. Patella. Numerical study of cavitating flows with thermodynamic effect. *Computers & Fluids*, 39(1):99–113, 2010.

[24] J-P. Franc and J-M. Michel. *Fundamentals of cavitation*, volume 76. Springer Science & Business Media, 2006.

[25] S. Kim. A numerical study of unsteady cavitation on a hydrofoil. In *Proceedings of the 7th International Symposium on Cavitation*, number 56, pages 1–13, 2009.

[26] G. Vaz, D. Hally, T. Huuva, N. Bulten, P. Muller, P. Becchi, J. L. R. Herrer, S. Whitworth, R. Mace, and A. Korsstrom. Cavitating flow calculations for the E779A propeller in open water and behind conditions: Code comparison and solution validation. *Fifth International Symposium of Marine Propulsors*, 2015.

[27] O. Coutier-Delgosha, R. Fortes-Patella, and J-L. Reboud. Evaluation of the turbulence model influence on the numerical simulations of unsteady cavitation. *Journal of Fluids Engineering*, 125(1):38–45, 2003.

[28] R. E. Bensow and G. Bark. Implicit LES predictions of the cavitating flow on a propeller. *Journal of Fluids Engineering*, 132(4):1–10, 2010.

[29] A. Gnanaskandan and K. Mahesh. Large eddy simulation of the transition from sheet to cloud cavitation over a wedge. *International Journal of Multiphase Flow*, 83:86–102, 2016.

[30] Y. Wang, X. Wu, C. Huang, and X. Wu. Unsteady characteristics of cloud cavitating flow near the free surface around an axisymmetric projectile. *International Journal of Multiphase Flow*, 85:48–56, 2016.

[31] M. R. Pendar and E. Roohi. Cavitation characteristics around a sphere: An LES investigation. *International Journal of Multiphase Flow*, 98:1–23, 2018.

[32] Y. Long, X. Long, B. Ji, and T. Xing. Verification and validation of large eddy simulation of attached cavitating flow around a clark-y hydrofoil. *International Journal of Multiphase Flow*, 2019.

[33] C. Eskilsson and R.E. Bensow. A compressible model for cavitating flow: comparison between Euler, RANS and LES simulations. In *29th Symposium on Naval Hydrodynamics, Gothenburg, Sweden*, 2012.

[34] A. Gnanaskandan and K. Mahesh. Comparative study of RANS and LES in simulating cavitating flows. In *31st Symposium on Naval Hydrodynamics. California, USA*, 2016.

[35] A. Asnaghi and R. E. Bensow U. Svennberg. Comparative analysis of tip vortex flow using RANS and LES. In *7th International Conference on Computational Methods in Marine Engineering*, 2017.

[36] M. Bhatt and K. Mahesh. Numerical investigation of partial cavitation regimes over a wedge using large eddy simulations. *International Journal of Multiphase Flow*, 122:103155, 2020.

[37] A. Gnanaskandan and K. Mahesh. Numerical investigation of near-wake characteristics of cavitating flow over a circular cylinder. *Journal of Fluid Mechanics*, 790: 453–491, 2016.

[38] C.-T. Hsiao and G. L. Chahine. Scaling of tip vortex cavitation inception noise with a bubble dynamics model accounting for nuclei size distribution. *Journal of Fluids Engineering*, 127(1), 2005.

[39] F. L. Brandao, M. Bhatt, and K. Mahesh. Numerical study of cavitating regimes in flow over a circular cylinder. *Journal of Fluid Mechanics*, 885:A19, 2020.

[40] D. R. H. Beattie and P. B. Whalley. Simple two-phase fractional pressure drop calculation method. *International Journal of Multiphase Flow*, 8:83–87, 1982.

[41] J. L. Chen, B. Xue, K. Mahesh, and J. I. Siepmann. Molecular simulations probing the thermophysical properties of homogeneously stretched and bubbly water systems. *Journal of Chemical & Engineering Data*, 2019.

[42] C. H. Chang and M. S. Liou. A robust and accurate approach to computing compressible multiphase flow: Stratified flow model and ausm +-up scheme. *Journal of Computational Physics*, 40:85–96, 2007.

[43] A. Gnanaskandan and K. Mahesh. A numerical method to simulate turbulent cavitating flows. *International Journal of Multiphase Flow*, 70:22–34, 2015.

[44] H. B. Karplus. Velocity of sound in a liquid containing gas bubbles. *The Journal of the Acoustical Society of America*, 29:12–61, 1957.

[45] B. Budich, S. Schmidt, and N.A. Adams. Numerical simulation and analysis of condensation shocks in cavitating flows. *Journal of Fluid Mechanics*, 838:759–813, 2018.

[46] P. Moin, K. Squires, W. Cabot, and S. Lele. A dynamic subgrid-scale model for compressible turbulence and scalar transport. *Physics of Fluids*, 3(11):2746–2757, 1991.

[47] N. Park and K. Mahesh. Numerical and modeling issues in LES of compressible turbulence on unstructured grids. In *Proceedings of the 45th AIAA Aerospace Sciences Meeting and Exhibit, AIAA Paper*, number 0722, pages 1–18, 2007.

[48] H. C. Yee, N. D. Sandham, and M. J. Djomehri. Low–dissipative high–order shock–capturing methods using characteristic–based filters. *Journal of Computational Physics*, 150(1):199–238, 1999.

[49] T. D. Economan. Optimal shape design using an unsteady continuous adjoint approach. *PhD Dissertation*, 2014.

[50] A. Prosperetti and M. S. Plesset. Bubble dynamics and cavitation. *Annual Review of Fluid Mechanics*, 9(1):145–185, 1997.

[51] M. Bhatt, A. Gnanaskandan, and K. Mahesh. Evaluation of finite rate homogenous mixture model in cavitation bubble collapse. *9th International Symposium on Cavitation*, 2015.

[52] R. T. Knapp, J. W. Daily, and F. G. Hammit. *Cavitation.* McGraw-Hill Book Company, London, 1970.

[53] Y. Kawanami, H. Kato, H. Yamaguchi, M. Tanimura, and Y. Tagaya. Mechanism and control of cloud cavitation. *Journal of Fluids Engineering*, 119(4):788–794, 1997.

[54] R. E. A. Arndt, C. C. S. Song, M. Kjeldsen, J. He, and A. Keller. Instability of partial cavitation: a numerical/experimental approach. In *Proceedings of the 23rd Symposium on Naval Hydrodynamics*, pages 519–615. National Academies Press, 2000.

[55] S. Gopalan and J. Katz. Flow structure and modeling issues in the closure region of attached cavitation. *Physics of Fluids*, 12(4):895–911, 2000.

[56] K. R. Laberteaux and S. L. Ceccio. Partial cavity flows. Part 1. Cavities forming on models without spanwise variation. *Journal of Fluid Mechanics*, 431:1–41, 2001.

[57] E. Foeth, T.V. Terwisga, and C.V. Doorne. On the collapse structure of an attached cavity on a three-dimensional hydrofoil. *Journal of Fluids Engineering*, 130:071303, 2008.

[58] S. Frikha, O. Coutier-Delgosha, and J-A. Astolfi. Influence of the cavitation model on the simulation of cloud cavitation on 2D foil section. *International Journal of Rotating Machinery*, 2008:1–12, 2009.

[59] X. Peng, B. Ji, Y. Cao, L. Xu, G. Zhang, X. Luo, and X. Long. Combined experimental observation and numerical simulation of the cloud cavitation with u-type flow structures on hydrofoils. *International Journal of Multiphase Flow*, 79:10–22, 2016.

[60] J. K. Jakobsen. On the mechanism of head breakdown in cavitating inducers. *Journal of Basic Engineering*, pages 291–305, 1964.

[61] G. E. Reisman, Y. C. Wang, and C. E. Brennen. Observation of shock waves in cloud cavitation. *Journal of Fluid Mechanics*, 355:255–283, 1998.

[62] S. Schenke and T.J.C van Terwisga. Simulating compressibility in cavitating flows with an incompressible mass transfer flow solver. *Fifth International symposium on Marine Propulsors*, 2017.

[63] S. Jahangir, W. Hogendoorn, and C. Poelma. Dynamics of partial cavitation in an axisymmetric converging-diverging nozzle. *International Journal of Multiphase Flow*, 106:34–45, 2018.

[64] X. Wu, E. Maheux, and G. L. Chahine. An experimental study of sheet to cloud cavitation. *Experimental Thermal and Fluid Science*, 83:129–140, 2017.

[65] M. Bhatt and K. Mahesh. Investigation of sheet to cloud transition due to the propagation of condensation fronts over a sharp wedge using large eddy simulations. *10th International symposium on cavitation*, 2018.

[66] S. A. Makiharju, H. Ganesh, and S. L. Ceccio. The dynamics of partial cavity formation, shedding and the influence of dissolved and injected non-condensable gas. *Journal of Fluid Mechanics*, 829:420–458, 2017.

[67] R. J. Boswell. Design, cavitation performance, and open-water performance of a series of research skewed propellers. *Report : Naval ship research and development center Washington, D.C.*, 1971.

[68] J. W. Lindau, D. A. Boger, R. B. Medvitz, and R. F. Kunz. Propeller cavitation breakdown analysis. *Journal of Fluids Engineering*, 127, 2005.

[69] P. Kumar and K. Mahesh. Large eddy simulation of propeller wake instabilities. *Journal of Fluid Mechanics*, 814:361–396, 2017.

[70] T. Colonius. Modeling artificial boundary conditions for compressible flow. *Annual Review of Fluid Mechanics*, 36:315–345, 2004.

[71] K. Mahesh, G. Constantinescu, and P. Moin. A numerical method for large eddy simulation in complex geometries. *Journal of Computational Physics*, 197(1):215–240, 2004.

[72] E. Turkel. Preconditioned methods for solving the incompressible and low speed compressible equations. *Journal of Computational Physics*, 72:277–298, 1987.

[73] M. Bhatt and K. Mahesh. Investigation of propeller cavitation using compressible large eddy simulations. *Sixth International symposium on Marine Propulsors*, 2019.

[74] X. S. Li and C.W. Gu. An all-speed Roe-type scheme and its asymptotic analysis of low Mach number behavior. *Journal of Computational Physics*, pages 5144–5159, 2008.

[75] V. Vatsa and E. Turkel. Choice of variables and preconditioning for time dependent problems. 16^{th} *AIAA Computational Fluid Dynamics Conference*, page 3692, 2003.

[76] J. Hsu and A. Jameson. An implicit-explicit hybrid scheme for calculating complex unsteady flows. 40^{th} *AIAA Aerospace Science Meeting & Exhibit*, page 714, 2002.

[77] J. Lindau, R. Kunz, S. Venkateswaran, and C. Merkle. Development of a fully-compressible multi-phase Reynolds-averaged Navier-Stokes model. 15^{th} *AIAA Computational Fluid Dynamics Conference*, page 2648, 2001.

[78] E. Turkel. Preconditioning techniques in computational fluid dynamics. *Annual Review of Fluid Mechanics*, 31:385–416, 1999.

[79] C. L. Merkle. Computational modelling of the dynamics of sheet cavitation. In *3rd International Symposium on Cavitation, Grenoble, France*, 1998.

[80] H. Guillard and C. Viozat. On the behavior of upwind schemes in the low Mach number limit. *Computers & Fluids*, pages 63–86, 1999.

[81] J. M. Weiss and W. A Smith. Preconditioning applied to variable and constant density flows. *Journal of Computational Physics*, pages 2050–2057, 1995.

[82] S. Venkateswaran, J. W. Lindau, R. F. Kunz, and C. L. Merkle. Computation of multiphase mixture flows with compressibility effects. *Journal of Computational Physics*, 180(1):54–77, 2002.

[83] A. Jameson. Analysis and design of numerical schemes for gas dynamics, 1: artificial diffusion, upwind biasing, limiters and their effect on accuracy and multigrid convergence. *International Journal of Computational Fluid Dynamics*, 4(3-4):171–218, 1995.

[84] A. Gnanaskandan. Development of a methodology for LES of turbulent cavitating flows. 2015.

[85] C. H. K. Williamson. Vortex dynamics in the cylinder wake. *Annual Review of Fluid Mechanics*, 28:477–539, 1996.

Appendix A

Preconditioning matrices

A.1 Derivatives

The expressions of the derivatives appearing in the time derivative matrix (eq. 6.2) are derived by substituting the equation of state (eq. 2.9) in terms of density, and then taking its derivative at constant T. They are givne as:

$$\begin{aligned}
\rho_{Y_v} &= \frac{\partial \rho}{\partial Y_v}|_T \\
&= \rho^2 \left(\frac{1}{\rho_l} - \frac{1}{\rho_v} \right), \quad \text{and} \\
\rho_p &= \frac{\partial \rho}{\partial p}|_T = \frac{1}{c^2} \\
&= \frac{2p + P_c - \rho Y_v RgT - (1 - Y_v)\rho K_l T}{(p + P_c)Y_v RgT + p(1 - Y_v)K_l T}.
\end{aligned} \tag{A.1}$$

A.2 Jacobians and eigenvalues

The convective flux jacobian matrix with respect to the primitive variable vector (Q) is given as:

$$A = \frac{\partial F}{\partial Q} = \begin{pmatrix} V_n\rho_p & \rho n_x & \rho n_y & \rho n_z & \rho_{Y_v} V_n \\ uV_n\rho_p + n_x & \rho u n_x + \rho V_n & \rho u n_y & \rho u n_z & u\rho_{Y_v} V_n \\ vV_n\rho_p + n_y & \rho v n_x & \rho v n_y + \rho V_n & \rho v n_z & v\rho_{Y_v} V_n \\ wV_n\rho_p + n_z & \rho w n_x & \rho w n_y & \rho w n_z + \rho V_n & w\rho_{Y_v} V_n \\ Y_v V_n\rho_p & \rho V_n n_x & \rho V_n n_y & \rho V_n n_z & Y_v\rho_{Y_v} V_n + \rho V_n \end{pmatrix}. \tag{A.2}$$

The matrix A is evaluated at the cell face. n_x, n_y and n_z are the unit vectors along x, y and z axis respectively. The inverse of the time derivative matrix (eq.6.2) is given as:

$$\Gamma^{-1} = \begin{pmatrix} \frac{\rho+\rho_{Y_v} Y_v}{\rho\rho_p} & 0 & 0 & 0 & -\frac{\rho_{Y_v}}{\rho\rho_p} \\ -\frac{u}{\rho} & \frac{1}{\rho} & 0 & 0 & 0 \\ -\frac{v}{\rho} & 0 & \frac{1}{\rho} & 0 & 0 \\ -\frac{w}{\rho} & 0 & 0 & \frac{1}{\rho} & 0 \\ -\frac{Y_v}{\rho} & 0 & 0 & 0 & \frac{1}{\rho} \end{pmatrix}. \tag{A.3}$$

Finally, the eigenvalues of the system of equation (eq.6.1) can be obtained by computing the jacobian:

$$A_\Gamma = \Gamma^{-1}A = \begin{pmatrix} V_n & \frac{\rho n_x}{\rho_p} & \frac{\rho n_y}{\rho_p} & \frac{\rho n_z}{\rho_p} & 0 \\ \frac{n_x}{\rho} & V_n & 0 & 0 & 0 \\ \frac{n_y}{\rho} & 0 & V_n & 0 & 0 \\ \frac{n_z}{\rho} & 0 & 0 & V_n & 0 \\ 0 & 0 & 0 & 0 & V_n \end{pmatrix}. \tag{A.4}$$

The eigenvalues of the matrix A_Γ are $\lambda_\Gamma = [V_n, V_n, V_n, V_n - c, V_n + c]$, where c is the speed of sound given by eq.A.1. When the preconditioning is used, ρ_p in the Γ^{-1} matrix is modified to $\rho_p^{'}$ to construct Γ_p^{-1} matrix. The rest of the elements of the Γ_p matrix are the same as Γ. Here, $\rho_p^{'} = \frac{1}{U_\infty^2}$. The eigenvalues of the preconditioned system can

by obtained by computing the modified flux jacobian matrix given as:

$$A_{p\Gamma} = \Gamma_p^{-1} A = \begin{pmatrix} \frac{\rho_p}{\rho_p^{'}} V_n & \frac{\rho n_x}{\rho_p} & \frac{\rho n_y}{\rho_p} & \frac{\rho n_z}{\rho_p} & 0 \\ \frac{n_x}{\rho} & V_n & 0 & 0 & 0 \\ \frac{n_y}{\rho} & 0 & V_n & 0 & 0 \\ \frac{n_z}{\rho} & 0 & 0 & V_n & 0 \\ 0 & 0 & 0 & 0 & V_n \end{pmatrix}. \tag{A.5}$$

The eigenvalues of the matrix A_{p_Γ} are $\lambda_{p\Gamma} = [V_n, V_n, V_n,$
$\frac{1}{2}(V_n(1+\frac{c^{'2}}{c^2}) - \sqrt{V_n^2(1-\frac{c^{'2}}{c^2})^2 + 4c^{'2}}), \frac{1}{2}(V_n(1+\frac{c^{'2}}{c^2}) + \sqrt{V_n^2(1-\frac{c^{'2}}{c^2})^2 + 4c^{'2}})]$, where c' is the modified speed of sound based on $\rho_p^{'} = \frac{1}{c^{'2}}$. Note that all the eigenvalues are of the order V_n; when $c^{'2} = 1/\rho_p^{'} = U_\infty^2$ is used for the preconditioning. When the physical-time derivative terms are treated in an implicit manner, they are combined with the preconditioned pseudo-time derivative terms. The resulting time derivative matrix inverse is given as:

$$\Gamma_{pi}^{-1} = \left(1 + \frac{3\Delta\tau}{2\Delta t}\right)^{-1} \begin{pmatrix} \frac{\rho + \rho_{Y_v} Y_v}{\rho \rho_p^{''}} & 0 & 0 & 0 & -\frac{\rho_{Y_v}}{\rho \rho_p^{''}} \\ -\frac{u}{\rho} & \frac{1}{\rho} & 0 & 0 & 0 \\ -\frac{v}{\rho} & 0 & \frac{1}{\rho} & 0 & 0 \\ -\frac{w}{\rho} & 0 & 0 & \frac{1}{\rho} & 0 \\ -\frac{Y_v}{\rho} & 0 & 0 & 0 & \frac{1}{\rho} \end{pmatrix}. \tag{A.6}$$

Here, $\rho_p^{''} = \frac{\rho_p^{'} + \frac{3\Delta\tau}{2\Delta t}\rho_p}{1 + \frac{3\Delta\tau}{2\Delta t}}$. Note that the eigenvalues of the corresponding flux jacobian matrix ($A_{pi\Gamma} = \Gamma_{pi}^{-1} A$) are the same as $A_{p\Gamma}$.